A KINEMATICALLY COMPLETE, INTERDICSIPLINARY, AND CO-INSTITUTIONAL MEASUREMENT OF THE ^{19}F(α,n) CROSS SECTION FOR NUCLEAR SAFEGUARDS SCIENCE

IN13-V-F(a,n)-PD2La

W. A. Peters[a,f], M. S. Smith[a], S. Pittman[a], S. J. Thompson[b], R. R. C. Clement[b,h], J. A. Cizewski[c], S. D. Pain[a], M. Febbraro[a,e], K.A. Chipps[a], S. Burcher[c], B. Manning[c], C. Reingold[c], R. Avetisyan[d], A. Battaglia[d], Y. Chen[d], A. Long[d], S. Lyons[d], S.T. Marley[d], C. Seymour[d], K. T. Siegl[d], M. K. Smith[d], S. Strauss[d], R. Talwar[d], D. W. Bardayan[d], A. Gyurjinyan[d], K. Smith[f], C. Thornsberry[f], P. Thompson[f], M. Madurga[f], E. Stech[d], W.-P. Tan[d], M. Wiescher[d], S. Ilyushkin[g], Z. Tully[i], M. M. Grinder[b]

[a] Oak Ridge National Laboratory, [b] Idaho National Laboratory, [c] Rutgers University, [d] University of Notre Dame, [e] University of Michigan, [f] University of Tennessee, [g] Colorado School of Mines, [h] U.S. Air Force, [i] Tennessee Technological University

Abstract

Alpha particles emitted from the decay of uranium in a UF_6 matrix can interact with fluorine and generate neutrons via the $^{19}F(\alpha,n)^{22}Na$ reaction. These neutrons can be used to determine the uranium content in a UF_6 storage cylinder. The accuracy of this self-interrogating, non-destructive assay (NDA) technique is, however, limited by the uncertainty of the $^{19}F(\alpha,n)^{22}Na$ cross section. We have performed complementary measurements of the $^{19}F(\alpha,n)^{22}Na$ reaction with both ^{4}He and ^{19}F beams to improve the precision of the $^{19}F(\alpha,n)^{22}Na$ cross section over the alpha energy range that encompasses common actinide alpha decay needed for NDA studies. We have determined an absolute cross section for the $^{19}F(\alpha,n)^{22}Na$ reaction to an average precision of 7.6% over the alpha energy range of 3.9 – 6.7 MeV. We utilized this cross section in a simulation of a 110 g spherical UF_6 assembly and obtained a change in neutron emission rate values of approximately 10-12%, and a significant (factor of 3.6) decrease in the neutron emission rate uncertainty (from 50-51% to 13-14%), compared to simulations using the old cross section. Our new absolute cross section enables improved interpretations of NDAs of containers of arbitrary size and configuration.

TABLE OF CONTENTS

LIST OF FIGURES

LIST OF TABLES

1. INTRODUCTION

1.a. Importance of Non-Destructive Assays and the $^{19}F(\alpha,n)^{22}Na$ reaction cross section

Non-destructive assays are widely utilized in the nuclear, safeguards, and defense industries [Hsu78, Mil12]. They enable the determination of amounts of fissile material without the need for direct contact or sampling. NDAs are needed to prevent the accidental loss of fissile material as well as the amount of holdup in an enrichment plant, and are thus invaluable to plant operators responsible for material accountancy and criticality safety. NDAs can also be used to prevent the misuse of fissile material through many scenarios, including: using a reactor to create undeclared highly-enriched (greater than 20%) uranium (HEU); diverting low-enriched (less than 5%) uranium (LEU), natural uranium (NU), or depleted uranium (DU) for sale; and producing excess amounts of LEU. The IAEA has, for example, recently proposed the development of unattended cylinder verification stations that automate the NDA process [Smi14]. It is anticipated that such automated verification and tracking systems would be deployed at enrichment facilities, fuel fabrication plants, and storage locations.

The IAEA has set goals for detecting 25 kg of ^{235}U in one year in HEU form, and 75 kg of ^{235}U in one year for all other forms. To reach such detection goals, sensitive assay techniques are required. Some NDA techniques (Fig. 1-1) require an external radiation source to induce secondary radiation in the material (*e.g.*, [Ped07]), which is subsequently detected externally to complete the assay, while other "self-interrogating" techniques utilize radiation generated within, and detected outside of, the sample (*e.g.,* [Mil12], [Che10]). One of these passive neutron-emission monitoring NDA techniques [LaF13, Kim08, Mil14] is based on alphas emitted from the natural decay of U in a UF_6 matrix commonly used in the uranium enrichment process (Fig. 1-2); here the alpha emission is overwhelmingly from ^{234}U rather than from ^{235}U or ^{238}U. These alphas subsequently interact with fluorine in the matrix and generate neutrons via the $^{19}F(\alpha,n)^{22}Na$ reaction. Given the $^{19}F(\alpha,n)^{22}Na$ reaction cross section and the alpha spectrum from uranium decay, the amount of ^{234}U can be determined via a measurement of the neutron flux and energy spectra outside the matrix. When combined with the $^{234}U/^{235}U$ ratio inferred from the enrichment process, the amount of fissile ^{235}U could then be determined in a non-destructive manner. This passive NDA approach can potentially improve safeguards and materials accounting at enrichment plants, but only if the neutron emission yields or rates per gram of uranium are accurately known.

1.b. Previous $^{19}F(\alpha,n)^{22}Na$ measurements

The energies of alphas from uranium decay range are less than 6 MeV, making this the range over which the $^{19}F(\alpha,n)^{22}Na$ reaction cross section must be known for NDA studies. For alphas of this energy, no other reaction channels (*e.g.*, (α,pn), $(\alpha,\alpha'n)$, $(\alpha,2n)$) are open. The $^{19}F(\alpha,n)^{22}Na$ reaction proceeds through unbound ^{23}Na resonances, some of which are known from a variety of other reaction studies of this nucleus [Fir07].

There have been a number of measurements of $^{19}F(\alpha,n)^{22}Na$, but there is no precision cross section determination over the entire energy range of interest for NDA studies. We also note that since most of the previous studies moderated the neutrons emitted from the target, they could not determine the neutron energy distribution resulting from the (α,n) reaction. Bair and Gomez del Campo [Bai79], for example, used alpha ranging from 4 – 8 MeV to bombard thick (stopping) PbF_2 and ZnF_2 targets within a 1.5 meter diameter sphere of reactor-grade graphite with eight ^{10}B-enriched BF_3 counters embedded near the surface. Such thick target measurements do not directly measure the differential or total cross section as a function of energy. In this work, the number of neutrons per 10^6 incident alphas from an infinitely thick target is determined. Norman *et al.* [Nor84] also used the thick target approach, covering the alpha energy range 3.6 to 9.9 MeV.

They used a stopping PbF_2 target surrounded by a 1.5m diameter graphite moderator and an array of 10 ^{3}He proportional counters. By subtracting the yield of all neutrons measured at beam adjacent beam energies differing by 0.25 MeV, Norman *et al.* calculate a set of *average* cross sections over broad 250-keV energy bins to a precision of approximately 10 - 12%. We note that their average cross section determination depends linearly on the stopping power [And77] of alpha particles in the PbF_2 target. In a recent publication, Norman *et al.* [Nor15] give additional details on their 1984 measurement: they report the neutron yields per 10^6 incident alpha particles with an uncertainty of 5%, and they state the discrepancy with the result of Bair and Gomez del Campo [Bai79] ranges from 54% to 35% for alpha energies increasing from 4 to 8 MeV, respectively. The discrepancy may be due in part to differing neutron escape probabilities of the moderated neutron detection systems.

Two studies used thin targets to determine the cross section as a function of energy, but neither covered the alpha energy range needed for NDA studies. Balakrishnan *et al.* [Bal78] used a thin target with very fine (5 keV) energy steps to determine cross sections to 15% over the range of 2.6 – 5.1 MeV. Significant resonant structure was shown in their work that is averaged out in the thick target measurements. Norman *et al.* [Nor84] state that their results agree reasonably with those of Balakrishnan *et al.* [Bal78] when the latter are appropriately energy-averaged. Wrean and Kavanagh [Wre00] covered the alpha energy range of 2.3 - 3.1 MeV using a thin-target and determined the $^{19}F(\alpha,n)^{22}Na$ cross section to a precision of 8%. Their measurement, over alpha energies just below those needed for NDA studies, also showed significant resonant structure in the reaction.

In a different approach, Jacobs and Liskien [Jac83] bombarded stopping CaF_2 targets with a pulsed alpha beam with energies of 4.0, 4.5, 5.0, and 5.5 MeV. They measured neutrons with a single 5 cm diameter liquid scintillator detector placed at 3.5 meters distance from the target (a solid angle of 0.16 msr), and they measured neutron energy spectra with a neutron time-of-flight (TOF) technique that used the beam pulse to start the TOF and the neutron detection as the stop signal. Because of the detector response, their spectra needed to be extrapolated (with an uncertainty of 50%) at energies below 300 keV. Their time resolution of 2 ns corresponded to approximately 300 keV neutron energy resolution at the highest neutron energies. They measured the angular distributions of their thick-target neutron energy spectra in the reaction plane by positioning their detector at five different angles at each bombarding energy. Their data was binned and fitted with Legendre polynomials to extrapolate the angular distribution, and then integrated over angles to determine a total neutron yield. They found a thick-target, angle- and energy-integrated neutron yield per incident alpha that was 20% higher than that found in Bair and Gomez del Campo [Bai79].

There have been several assessments of the $^{19}F(\alpha,n)^{22}Na$ cross section. An early evaluation was performed by Vukulov *et al.* [Vuk83] over the energy range 2.5 to 7.75 MeV. They assign uncertainties of up to 10% to the cross section. The evaluation of Murata *et al.* [Mur06] in the JENDL/AN-2005 library [JEN14] is based on calculations with the EG-GNASH code [Yam90], optimized at energies significantly above those needed for NDA studies. They reproduce the cross section derived in Norman *et al.* [Nor84] and the thick-target yield of Bair and Gomez del Campo [Bai79] but do not account for the discrepancy between these two measurements. Assuming isotropic angular distributions, they also calculate the neutron energy spectra as a function of alpha bombarding energy. We note that an uncertainty is not reported in this study [Mur06], nor is the resonant structure seen in Wrean and Kavanagh [Wre00] reproduced. The TENDL-2015 library [TEN15] includes an evaluation of the $^{19}F(\alpha,n)^{22}Na$ cross section as calculated with the TALYS reaction code [TAL16]. Recent tests with TENDL libraries [Fen14]

demonstrated that thick target yields calculated with their $^{19}F(\alpha,n)^{22}Na$ cross section differed by 20-60% from measurements for ^{19}F in the energy range of ^{234}U alpha emissions. An earlier TALYS calculation of the reaction was used in the TENDL 2012 library and put into an ENDF format [TEN12]. Finally, van den Berg and Simakov [van15] give an assessment of $^{19}F(\alpha,n)^{22}Na$ but do not quote an uncertainty. They discuss the JENDL and TENDL evaluations and the datasets of [Nor84] and [Wre00], but do not discuss discrepancies with other data sets (*e.g.*, [Bai79]).

1.c. Need for an improved characterization of $^{19}F(\alpha,n)^{22}Na$

There is a significant need for an improved determination of the $^{19}F(\alpha,n)^{22}Na$ cross section. First, the thick-target measurements have discrepancies significantly larger (*e.g.*, 35 – 54%) than quoted uncertainties (*e.g.*, 7 – 10%) of each data set. A reasonable assessment [Laf13] of the current uncertainty in the $^{19}F(\alpha,n)^{22}Na$ cross section is 15% - 25%. Miller *et al.* [Mil14] agree that the database is discrepant. According to Croft *et al.* [Cro03], the need for additional experiments "has long been recognized."

Second, the results of NDAs based on neutron self-interrogation from uranium alpha decay depend linearly on the $^{19}F(\alpha,n)^{22}Na$ cross section, and the current spread in datasets limit the accuracy of the assays [Cro03, LaF13, Kim08, Mil14]. For example, Kimball and Gauld [Kim08] report that the use of certain datasets can lead to assays that underestimate the ^{235}U contents by as much as 40%. Miller *et al.* [Mil14] show a spread of a factor of 1.4 between yields calculated with different cross sections, and call for a reduction in the uncertainty by an order of magnitude to improve NDAs. In fact, the roughly 40% discrepancy between thick target yield datasets corresponds to a 28 kg uncertainty in the amount of ^{235}U in a 2300 kg capacity Model 30B container used to store LEU. This assay uncertainty is larger than the proposed IAEA detection limits mentioned above.

Third, a more complete characterization of the $^{19}F(\alpha,n)^{22}Na$ reaction that included the neutron energy spectrum and neutron angular distributions as a function of bombarding energy, taken with a thin target, would be a significant step forward. It would enable much more sophisticated modeling of the signals expected from new or proposed NDA system, and a better interpretation of measured neutron yields of any type of storage cylinder. Such a dataset would provide a versatile solution that can be used in a wide variety of NDA studies. Specifically, they could be used for advanced modeling of those in the Uranium Cylinder Assay System [Mil10a] that have been used for measurements at LANL. An improved cross section could also be used for more accurate simulations needed for a variety of NDA systems including the Passive Neutron Enrichment Meter (LANL) [Mil10b] and the Hybrid Enrichment Verification Array (PNNL) [Mac11], as well as to interpret existing bench scale measurement data.

Finally, an improved $^{19}F(\alpha,n)^{22}Na$ cross section has applications for fuel cycle NDA studies beyond UF_6 [Cro97]. For example, systems utilizing any of the fluorinated actinides (UF_4, PuF_3, PuF_6, and UO_2F_2) will benefit from improved modeling, as will studies of aqueous reprocessing systems wherein neutrons are generated when alphas interact with fluorine in hydrofluoric acid, as well as studies of pyroprocesses with molten fluoride salts which generate neutrons when exposed to alphas from actinide decay.

2. EXPERIMENTAL SETUP

2.a. Overall approach

We first measured the $^{19}F(\alpha,n)^{22}Na$ reaction by bombarding a thin fluorine target with an alpha beam at 135 different energies covering the range necessary for NDA studies. We used an energy

step size of 25 keV for our excitation function. At each bombarding energy, we measured the neutron time-of-flight (TOF) spectrum with a large array of 42 detectors. We then performed a complementary measurement, at a different laboratory but with the same neutron detector array, bombarding a helium gas target with a fluorine beam with smaller (approximately 5 keV) energy steps over four critical energy regions (*e.g.*, resonances and other rapid changes in cross section) as identified in our alpha-beam measurement. The subsections below describe these two experiments in detail. Our data analysis is described in Section 3, and Section 4 addresses the utilization of our results in an NDA simulation.

2.b. Alpha-beam experiment setup

This experiment was performed at the Nuclear Science Laboratory at the University of Notre Dame [Apr14]. Alpha beams generated by a duoplasmatron-type ion source were brought up to energies of 3.9 – 6.7 MeV using their FN Tandem electrostatic accelerator. Beam energies were determined by a calibrated NMR to within 5 keV, smaller than the energy thickness of the target (see below). For a subset of the runs, the energy uncertainty was increased due to the analyzing magnet not being properly cycled along the hysteresis curve; these runs were not averaged with those that were cycled regularly. We chose a moderate energy step size of 25 keV for our excitation function measurement, an order of magnitude smaller than that of the energy-averaged cross section determined by Norman *et al.* [Nor84] in their thick-target experiment. The pulsed time structure (3 ns wide pulses, in multiples of 100 ns between pulses) of the alpha beam provided the timing "start" for our neutron energy measurement via neutron TOF; the timing "stop" signal was provided by the neutron detectors described below. The beam current was integrated by measuring the electrical current of the entire target chamber and beam dump assembly. This ensured any charge exchange effects occurring in the target were included so the original current of the beam is recorded. The beam dump consisted of a tungsten plate located within a shielded wall over 2 meters downstream so as to not cause significant gamma or neutron background in the neutron array.

Our thin targets (Fig. 2-1), fabricated by the Luxel Corporation [LUX], were composed of 49 nm (29 $\mu g/cm^2$) of lanthanum fluoride LaF_3 evaporated onto 84 nm (50 $\mu g/cm^2$) of Au. The energy thickness of these targets was approximately 12 keV. The choice of a lanthanum molecule and a gold backing for the target was made because the high Coulumb barrier for reactions of alpha particles on Au and La at these energies significantly reduced backgrounds compared to AlF_3 or other lighter targets. Rutherford back scattering (RBS) was used to verify the thickness (to 2%) of the targets as well as their stoichiometry and purity.

We utilized the Versatile Array of Neutron Detectors at Low Energy (VANDLE) system [Pet16] to detect neutrons from the $^{19}F(\alpha,n)^{22}Na$ reaction. This installation of VANDLE consisted of 42 bars of plastic scintillators BC-408 (EJ-200 plastic) of size 60 cm long x 3 cm wide x 3 cm deep (Fig. 2-2). Each bar has a Hamamatsu photomultiplier tube (PMT) attached to each end via optical cement, and the bars are wrapped in nitrocellulose paper and aluminized Mylar to keep the bars light-tight and to transport as much of the scintillation light to the PMTs as possible. These bars detect the position and energy of neutrons over an energy range of 0.1 - 20 MeV. Neutron position along the bar (related to emission angle) is determined from the time difference of signals reaching the PMT at each end of each bar, and neutron energy is determined by their time-of-flight (TOF) between the target (the alpha beam pulse time) and the detector (the detector event signal). The position of the center of each of the bars was measured to within 0.5 cm. The PMTs are coupled to a digital data acquisition system based on XIA PIXIE-16 250 MHz waveform digitizers. This system routes PMT signals through a low-pass filter into a digitizer and then to an FPGA shaping circuit. The detectors have a hardware threshold near 8 keVee (8 keV

electron equivalent light yield), and are capable of detecting neutrons with as little as 100 keV of kinetic energy. The time resolution of the detector signals is less than 750 ps. Placing the bar 50 cm from the target results in the depth of the bars (3 cm) contributing 7% to the neutron energy resolution.

For neutron energy measurements via TOF, the energy resolution improves with a longer flight path and better detector timing resolution, the angular resolution improves with a longer flight path, and the detection efficiency improves with lower neutron energy threshold, better light collection, and shorter flight path to increase solid angle. VANDLE bars can be arranged in any manner to optimize the time (energy) resolution, angular resolution, and yield for the experiment at hand. The arrangement of neutron detectors for this experiment is shown in Fig. 2-3. They covered the angular ranges of 21 – 170 degrees (beam right side) and 75 – 150 degrees (beam left side), for a solid angle of 227 msr. Each VANDLE bar itself subtended 5.4 msr. The numbering scheme for the bars is shown in Fig. 2-4. The neutron detection efficiency of the VANDLE system depends on a sum of these subtended solid angles (geometric efficiency) multiplied by the intrinsic detection efficiency of each bar. This latter quantity, determined using a Cf source measurement and a ^{27}Al(d,n) measurement [Pet16] (Fig. 2-5), ranges from 35% to 15% for neutron energies of 1 to 6 MeV, respectively, using a 60 keVee threshold applied to the data.

Alpha-beam data was collected over 14 days of 24/7 operations with an average of 30 nC of 2+ alpha particles, for an integrated beam of 0.036 Coulombs. The neutron TOF (energy) spectra were collected in each of the 42 bars at 135 energies between 3.9 and 6.7 MeV; a representative TOF spectrum is shown in Fig. 2-6. Fig. 2-7 shows neutron TOF spectra across the entire array at a single bombarding energy. As evident in this figure, neutrons from reactions to the ^{22}Na ground state and to a number of ^{22}Na excited states were obtained in these TOF spectra at all angles (*i.e.*, all VANDLE bars). The neutron yields per bar were approximately 10 - 80 per microCoulomb of alphas. The VANDLE bars were able to provide good separation between the gamma-ray flash and the neutrons (Fig. 2-7 and Fig. 2-8) by their different TOF. The neutron energy resolution depends on the energy of the neutrons but was approximately 20% for 1.5 MeV neutrons and was dominated by the 3 ns pulse width of the bunched alpha beam. The details of our analysis to extract an absolute cross section from the neutron yields are given below in Section 3.

2.c. Fluorine-beam experiment setup

This complementary experiment, performed at Oak Ridge National Laboratory, was designed to measure relative yields of the ^{19}F(α,n)^{22}Na reaction with very fine energy steps over energy regions identified as crucial in the alpha-beam experiment. We made an "inverse kinematics" (IK) (heavy beam incident on a light target) measurement of ^{19}F(α,n)^{22}Na by bombarding a helium gas target with a ^{19}F beam from a 25 MV Tandem electrostatic accelerator [Jon86], and detecting the neutrons in coincidence with the ^{22}Na reaction products. By using an IK approach, the ^{22}Na – the "recoils" of the reaction – are forward focussed in the laboratory frame and can be detected with high efficiency using a recoil spectrometer system of modest acceptance. The neutrons, on the other hand, are still emitted in 4π and require a large-acceptance array to measure. We chose to use the well-characterized VANDLE system to reduce systematic errors when combining results of the fluorine- and alpha-beam experiments; and we used the Daresbury Recoil Separator (DRS), described below, to detect the recoiling ^{22}Na ions. A layout of the accelerator facility is shown in Fig. 2-9, and the experimental arrangement is shown in Fig. 2-10.

The ORNL Tandem accelerator has excellent beam quality, with energies determined to 1 part in 10^4, beam spot sizes of 2 mm diameter, and an emittance of 1 π mm mrad. The small energy changes required for measurements over crucial regions can be made in as little as 30 minutes.

There is no time structure for this DC (continuous) accelerator beam, so a detection of ^{22}Na recoils was needed to "start" the neutron TOF measurement; the "stop" signal came from the VANDLE detector signal. Since the recoils were detected with high efficiency, the coincidence requirement did not significantly decrease the yields of neutrons that followed a direct path from target to detector. However, the coincidence requirement did result in a substantial decrease in the yields of neutrons scattered off the floor and walls that arose from reactions induced by fluorine nuclei arriving at the target at different times.

The ^{19}F beams had intensities up to 10^{10} particles per second (pps) and energies of 12 - 38 MeV beams, requiring approximately 1.5 MV terminal potential, to give the same center of mass energy as the 3.9 – 6.7 MeV bombarding energy used in the alpha-beam experiment. We changed the beam energy in approximately 5 keV-wide steps over 4 energy ranges as identified in the alpha-beam measurement. The central energies of these 4 ranges were 5.300, 5.910, 6.075, and 6.530 MeV. We typically collected data for a few hours at each beam energy, and repeated a number of beam energies to determine reproducibility. Our energy step size of 5 keV is a factor of 35 less than that of the energy-averaged cross section determined by Norman *et al.* [Nor84] in their thick-target experiment. The use of the gas target system, described below, required precise tuning of the beam through a series of small (few mm) apertures arranged over a distance of 2 meters.

We utilized components of the Jet Experiments for Nuclear Structure and Astrophysics (JENSA) system [Chi14] to provide a windowless recirculating gas target system for our fluorine-beam measurements (Fig. 2-11). The ^{4}He gas pressure was very stable at 4000 ± 5 mTorr, corresponding to an energy thickness of 5 keV, a factor of 2.5 lower than the energy thickness of the LaF_3 targets used in the alpha-beam experiments. The pressure was recorded before, during, and after each run. The helium gas has a purity of better than 1 part in 10^6 and therefore had no contaminants contributing to background in the measurement. The thickness is 2.6 μg/cm^2 of pure helium for an active length of the target region of 3 cm. This size is matched to the cross-sectional size (width) of the VANDLE detection bars.

Beam current and target thickness normalizations were made by measuring the scattering of ^{4}He nuclei out of the target by the ^{19}F beam particles. This technique is often straightforward, with the yield predicted by Rutherford (elastic) scattering formula [Mel66] to depend on the angle of detection and the energy of the beam. However, because there are resonances in ^{19}F(α,α) at these energies, the yield does not follow the Rutherford formula; rather, it must be measured to enable an accurate normalization of the beam current. We ran a separate measurement of this scattering over energy from 20 – 38 MeV, which covers the energy ranges for our coincidence measurement that were listed above. We used the same detector, beam, and target arrangement for ^{19}F(α,α) that we used for our ^{19}F(α,n)^{22}Na data runs.

The ^{19}F(α,α) relative rate was measured by installing an electrically isolated beam current monitor – a suppressed Faraday cup – behind the target. The integrated current was recorded while simultaneously measuring the alpha particles scattered out of the gas target with a small collimated Si charged-particle detector arranged 28 cm from the target gas at an angle of 45 degrees (Fig. 2-12). A typical yield of a scattering run is shown in Fig. 2-13. The same energies use for the ^{19}F(α,n)^{22}Na data runs were repeated to determine the corresponding ^{19}F(α,α) yields. In some cases where the ^{19}F(α,α) yields were smoothly varying, a linear interpolation was used to determine additional values to normalize ^{19}F(α,n)^{22}Na yields. The same Si detector at 45 degrees was utilized for the ^{19}F(α,n)^{22}Na runs, which enabled the measured He-scattered counts to be used to normalize the beam current.

We detected neutrons both forward and backward of 90 degrees with the VANDLE system. The same bars were used for this experiment as were used for the alpha-beam measurements, but with a different arrangement (Fig. 2-14 and Fig. 2-15). A typical neutron TOF spectrum for the fluorine-beam experiment is shown in Fig. 2-16. The Daresbury Recoil Separator [Chi09] (Fig. 2-17) was used to capture the ^{22}Na ions resulting from the ^{19}F(α,n)^{22}Na reaction. The DRS is a 13m-long, 90-ton device that is aligned along the beam axis (*i.e.*, at zero degrees) and consists of two velocity filters (with crossed electric and magnetic fields), a dipole magnet, and 3 sets of focusing quadrupole-triplet magnets. The DRS is optimized for measurements of IK reactions where the recoils are focused into a narrow downstream-oriented (forward) cone. The DRS electromagnet elements were set to focus the ^{22}Na "recoil" ions into a focal plane detector system, while simultaneously rejecting (by steering into interior walls of the vacuum chambers of the components) the primary ^{19}F beam that enters the DRS along the beam axis. The system has an energy acceptance of ±5% and a dispersion at the final mass/charge focal plane of 0.1% M/q per mm. The DRS angular acceptance is ± 45 mrad (±2.6 degrees), which is not sufficiently large to capture all of the ^{22}Na recoils from the ^{19}F(α,n)^{22}Na reaction (with opening angles up to 4 degrees) at the low beam energies needed for this measurement. The impact of this limited acceptance on the experiment is that we can only determine relative cross sections; this is discussed in detail below in §3.b.

At the DRS focal plane, we direct the recoils through a transmission microchannel plate detector system [Sha05] to generate a fast timing signal needed as the "start" of the neutron TOF. The particles then enter a high-rate gas ionization counter [Cha14] (Fig. 2-18). This large-acceptance detector features tilted-grid wire electrodes to accept particle at rates up to $2 \cdot 10^5$ pps. In this detector, the ions are identified, counted, and have their energy measured. The particle identification is crucial, because for every single ^{22}Na recoil that reaches the focal plane detector, there are typically 100 beam particles that have passed through the entire DRS to reach the detector after multiple scattering events off of surfaces inside the DRS elements. The gas ionization counter serves to differentiate the recoils from the scattered beam events on the basis of the *Z*-dependence (proton number) of the energy loss of ions as they traverse the CF_4 gas. The DRS coupled with the gas ionization counter can provide clean identification of ions that differ in atomic number *Z* by 1 in the mass range for this experiment (Fig 2-19). The particle identification plots in this figure were used to determine the ^{22}Na yields as described below in §3.b.

Fluorine-beam data was collected over approximately 20 days of 24/7 operations. The neutron energy spectra were collected in each of the 42 bars at a total of 27 energies, distributed among the 4 energy regions listed above. Data were typically collected for 2 to 3 hours at each beam energy. Neutrons from reactions to the ^{22}Na ground state and to a number of ^{22}Na excited states were unresolved and summed at all angles (*i.e.*, for all VANDLE bars). The gamma-flash was cleanly identified in the neutron TOF spectra (Fig. 2-16). We collected a ^{22}Na spectrum at each energy (Fig. 2-19), as well as (α,α) scattering data to normalize the beam current and target thickness. Details of our analysis to extract relative yields of neutrons and ^{22}Na over the 4 energy ranges are given below in §3.b.

3. DATA ANALYSIS AND DISCUSSION

3.a. Alpha-beam experiment cross section determination

The data from the alpha-beam experiment consists of over 4000 neutron TOF datasets collected in 42 VANDLE bars (angles) during multiple runs at 135 different beam energies. We converted the data from the VANDLE data acquisition system [Pet16] into tables formatted for ROOT

[Roo16] for later comparisons to simulations. Below we give an overview of our analysis procedure followed by details on each of the analysis steps.

3.a.1. Overview

Our data analysis strategy for the alpha-beam experiment is as follows. At each bombarding energy, we recorded a neutron TOF spectrum for each of the 42 VANDLE bars (§3.a.2); we also recorded the integrated beam current for the run (§3.a.3). Target thickness was determined via separate Rutherford backscattering (RBS) measurements (§3.a.4). The TOF spectra are fit to extract the area of each TOF peaks corresponding to the yield of neutrons proceeding to the ^{22}Na ground state or to one of a number of ^{22}Na excited states (§3.a.2). The yields for all neutron TOF peaks are summed for each bar, and this is repeated for each of the 42 bars and collected into a distribution of *measured neutron yield vs. angle* across the array. We then perform an MCNP6 [MCN14] simulation (§3.a.6) to determine, for each bar, the yield of neutrons leading to each possible ^{22}Na level as normalized to one reaction event. This simulation includes geometry, kinematics, intrinsic detector efficiency (§3.a.5), and scattering from pipe, floor, and other setup materials. These simulation results are collected into a set of *predicted neutron yield per level per reaction vs. angle* distributions, for each of the ^{22}Na levels. Each of these distributions is then multiplied by a weighting factor of the number of reactions proceeding to that particular ^{22}Na level; this factor equals the partial cross section for this ^{22}Na level multiplied by the integrated beam current for the run and the areal density of the target. The weighted sum of the predicted distributions is then compared to the *measured neutron yield vs. angle* distribution (§3.a.7), and the weighting factors are adjusted in a least-squares fit to minimize the difference between the predicted and measured distributions (§3.a.7). The total cross section is determined by the sum of the partial cross sections to all energetically possible ^{22}Na levels. Multiple runs made at the same energy are merged appropriately (§3.a.8). The uncertainties are discussed for each step and combined appropriately (§3.a.9).

Our analysis accounts for: the detector efficiency of each bar; the missing neutrons due to limited VANDLE solid angle; the scattering of neutrons off of the walls, floor, and other objects; the variation of neutron yield, energy, and detection efficiency over the solid angle of each detector bar; the change in neutron energy in the lab frame as a function of angle; and a point-by-point attribution of cross section and uncertainty. The limitations of our analysis are given below in §3.a.10. This process, described in detail in the following sub-subsections, is repeated for all bombarding energies to build up the ^{19}F(α,n) excitation function given in §3.a.11.

3.a.2. Neutron yields

To determine the ^{19}F(α,n)^{22}Na reaction cross section at a given energy, we began by summing up the neutron counts above background in each TOF histogram. For cases where multiple runs at the same energy were made, the runs were treated independently (see §3.a.8 below). A typical TOF spectrum (Fig. 3-1) exhibits peaks corresponding to neutrons from reactions to the ^{22}Na ground state and to a number of ^{22}Na excited states. We tracked both the areas and centroids of these individual peaks above a linear background as well as the sum of the yields above background. The relative yields to the ^{22}Na excited states were used to subsequently restrict the fitting procedure used to extract the partial cross sections. This histogram summing, however, is problematic for spectra where an individual neutron peak overlaps the tail of the gamma flash or overlaps another neutron peak. We therefore refined our approach and fit each TOF spectrum to a custom peak shape (Fig. 3-2) consisting of a Gaussian (normal distribution) plus an exponential tail extending to higher TOF (*i.e.*, lower energies). The peak shape was derived from a fit to the well-isolated peaks in a TOF spectrum of the ^{13}C(α,n)^{16}O reaction that we measured during this experiment. The peak areas resulting from the fits to the ^{19}F(α,n)^{22}Na TOF spectra were then used

for the neutron yields rather than the sum of counts above background in each histogram. Because of the large number (>7000) of spectra to fit, we wrote an automated program and visually inspected the fit results. We also made a linear fit to the TOF background using counts outside of the neutron peak areas or the gamma flash, with a resulting uncertainty of ±11 counts/channel that was consistent for all runs. The uncertainty of the background subtraction in our yield determination was then found by multiplying the full width of each peak by ±11 counts/channel. The statistics of the yields in the TOF spectra were typically 10^3 – 10^4 counts total per bar above background, and 10^2 – 10^4 per individual peak. We added the statistical and background uncertainties in quadrature to get the total uncertainty on the neutron TOF yields. For the stronger peaks (with ~ thousands of counts), the background contribution was a negligible contribution to the yield uncertainty, but for some weak peaks the background contribution was the dominant term. The yields for all neutron TOF peaks are summed for each bar, and this is repeated for each of the 42 bars and collected into a distribution of *measured neutron yield vs. bar* across the array (Fig. 3-3). We convert this to a plot of *measured neutron yield vs. angle* (Fig. 3-3) using the angle from the beam axis to the center of each bar. When appropriately adding together the uncertainties of each peak, the resulting uncertainties ranged from 2 to 20% for the *measured neutron yield vs. angle* at a given energy. Statistical uncertainties for neutron yields in all cases were better than 3% and in most cases were better than 1%. The reproducibility of neutron yields was checked by repeating measurements at 8 energies, and ranged from 0.02 – 3%; within the expected statistical and fitting uncertainties for those runs.

3.a.3. Beam current integration

For each run at each bombarding energy, we determined the number of beam particles on target by routing the collected charge on the beam stop to a beam current integrator (BCI). The BCI was routed through the acquisition system so it would have the same live time (ranging from 65% – 80%) as the neutron detector channels. The uncertainty on the BCI is less than 0.1% for most runs. There were, however, some runs that had a recording failure in the DAQ for the BCI channel, and for these cases the beam current is taken from the event counter into an ungated channel and the live-time determination. The uncertainty for these runs was still less than 1%. Unfortunately, the BCI signal connection was interrupted for a few runs, and for these cases the beam current was determined from the current as measured by the accelerator operators before and after the run and recorded in the logbook. For these cases, the integrated beam had an uncertainty ranging from 4% to 7%.

3.a.4. Target thickness

We made a number of RBS measurements to determine the thickness of the Au-backed LaF_3 foil targets in the experiment (Fig. 3-4). The area under the RBS peaks for Au, La, and F were determined and used to verify that the stoichiometry of the lanthanum fluoride was 1:3 (*i.e.*, LaF_3) and to determine a target thickness of 49 nm LaF3 on 85 nm Au. This LaF_3 layer corresponds to an areal density of 2.68 x 10^{17} F atoms/cm^2. The uncertainty of this determination was 2% from fitting the fluorine peak in the RBS spectrum. We note that this thickness corresponds to an energy thickness of 12.5 keV, only half of the 25 keV thickness expected from the manufacturer.

3.a.5. Intrinsic detection efficiency

The intrinsic neutron detection efficiency of a VANDLE bar (Fig. 2-5) [Pet16] was determined as a function of neutron energy via a separate measurement of the ^{27}Al(d,n) reaction at the Edwards Accelerator Facility at Ohio University, combined with a measurement with a calibrated ^{252}Cf source. The intrinsic efficiency, which depends on a (chosen) threshold, varies from a maximum of approximately 70% for neutrons of ~ 0.5 MeV to 20% for neutrons of ~6 MeV with no software threshold. With a higher threshold of 60 keVee (60 keV electron equivalent light yield),

this efficiency decreases to 35% to 15% at 1 MeV to 6 MeV, respectively. A GEANT4 [Ago03] simulation of the response of a VANDLE bar to a Cf neutron source gives good agreement with the corresponding measurement (Fig. 3-5). More details of the efficiency calibration can be found in [Pet16], including a determination of a 4% uncertainty in the efficiency. This efficiency was a crucial input for the simulations described below.

3.a.6. Simulations

Simulations are needed to interpret the distribution of *measured neutron yield vs. angle* described above in §3.a.2. This is because each VANDLE bar subtends a substantial opening angle over which the energies and yields of neutrons from the $^{19}F(\alpha,n)^{22}Na$ reaction change – both from reaction kinematics and from the emission of neutrons proceeding to different ^{22}Na levels. Furthermore, our *measured neutron yield vs. angle* distribution does not account for neutrons that were emitted at energies below our detection threshold of approximately 500 keV, or for neutrons emitted at angles not subtended by the VANDLE bars. We therefore relied on simulations to determine how large a reaction cross section is needed to produce a *total* neutron emission into 4π at each beam energy that will (after the incorporation of geometries, efficiencies, and other effects) match our *measured neutron yield vs. angle* distribution. This cross section is the result that we seek.

We utilized MCNP6 simulations to determine, for each bar, the yield of $^{19}F(\alpha,n)^{22}Na$ neutrons leading to each possible ^{22}Na level as normalized to one reaction event. The simulations include the known level structure of ^{22}Na [Bas15], center of mass reaction kinematics, an appropriate boost to the laboratory frame, and detector locations and geometry (Fig. 3-6). From this, the centroids of the neutron peaks expected in the TOF spectra of each bar were determined. The simulation also includes the intrinsic detector efficiency and threshold [Pet16], and incorporates events from emitted neutrons that scatter of beam pipes, the floor, and other large objects in the experimental hall. These simulation results are a set of *predicted neutron yield per level per reaction vs. angle* distributions across the array, one distribution for *each* ^{22}Na level (Fig. 3-7). As described in §3.a.7 below, the weighted sum of each of these distributions gives a *predicted neutron yield vs. angle* distribution that can be compared to our experimental results. The weighting factors are the number of reactions into each ^{22}Na level, which are proportional to the partial cross sections for each level.

To assign an uncertainty to our MCNP6 simulations, we ran GEANT4 [Ago03] simulations of a small number of runs (Fig. 3-8) to compare to the MCNP6 results. The approach of the GEANT4 simulations is very different: the full light transport through the bars is calculated using different physics libraries and *only* the detector 60 keVee threshold, geometry, and composition as input. The previously measured VANDLE efficiency is *not* an input in the simulation; rather, the system efficiency is calculated within the simulation. When the GEANT4 simulations for 5 runs were substituted for the MCNP6 simulations in the determination of the cross section (via the fitting procedure discussed below in §3.a.7), the cross sections from the two approaches agreed with an average deviation of 2% and a maximal deviation of 4%. We have therefore assigned a conservative systematic uncertainty of 4% to our MCNP6 simulations.

3.a.7. Fitting

At each energy, our MCNP6 simulation results are collected into a set of *predicted neutron yield per level per reaction vs. angle* distributions across the array, one distribution for reactions into each ^{22}Na level (Fig. 3-7). Each of these distributions is then multiplied by a weighting factor (*i.e.*, a fit coefficient) that is an *assumed* number of reactions into that ^{22}Na level. These fit coefficients are equal to an *assumed* partial cross section for this ^{22}Na level multiplied by the

integrated beam current for the run and by the areal density of the target. In the text below, we will use the terms fit coefficient, weighting factor, and partial cross sections interchangeably. The sum of the weighted distributions gives a *predicted neutron yield vs. angle* distribution for this set of assumed partial cross sections that can be compared to our experimental results. We adjusted the fit coefficients to minimize the difference between the *predicted yield vs. angle* and *measured yield vs. angle* distributions. We used ROOT to perform the fit via a least-squared minimization routine. The uncertainties of fit coefficients are correlated, which results in the uncertainty in the *sum* of the partial cross sections – the total cross section – being typically *less* than the uncertainty of each of the individual partial cross sections. We used ROOT to calculate the uncertainty correlation matrix for our fit (Fig. 3-9), which features off-diagonal elements characteristic of such correlated systems. An example of a typical fit is shown in Fig. 3-7; typically there were over 40 data points in the fit and less than 5 fit parameters. The fit coefficients were constrained by the relative yield to each ^{22}Na excited state as determined by the neutron TOF spectra. A typical uncertainty for the total cross section from this fit procedure was 3%; in some cases this was as large as 10%.

3.a.8. Merging datasets

For cases where we collected more than one data run at the same beam energy, we performed the analysis described above independently for each run, and combined the results with a weighted average to obtain the partial and total cross sections for this beam energy. The weighting factor was the integrated beam current of each run. The mean and standard deviation for the combined cross section dataset incorporates the separation between the mean values of each set in the appropriate manner [Bur15], such that the result is statistically the same as if all of the events in the multiple sets were analyzed together.

3.a.9. Uncertainties

The alpha bombarding energy uncertainties were half of the energy thickness of the target with a slight dependence on the beam energy, typically ±7 keV. In our analysis of the centroids of peaks in the neutron TOF spectra for a small number of runs, however, it was apparent that the beam energy was not the energy indicated by the NMR of the accelerator analyzing magnet. This was caused by a hysteresis effect in the magnet: accelerator analyzing magnets are typically always changed in a consistent direction that follows the magnet hysteresis curve. When the magnet is changed without appropriate cycling, the NMR calibration is invalid. We were able to estimate a correction to the beam energy for these runs based on TOF peak centroids, and we determined the appropriate size of the horizontal (energy) error bar to these points through consultation with the experts on the particular analyzing magnet used at Notre Dame. These points were *not* merged with others as described in §3.a.8 above because of the energy shift and their larger energy uncertainty, but were instead kept separate in the final results given below.

The uncertainties of our total cross sections were independently determined at each energy. As described above in §3.a.2, the combination of counting statistics, background subtraction, and summing of yields in different neutron TOF peaks resulted in a 2 to 20% uncertainty for the points in the *measured neutron yield vs. angle* distributions at a given energy. When we fit the *predicted neutron yield vs. angle* distribution (§3.a.7) to the corresponding *measured yield vs. angle* distribution (with its uncertainty), the fit coefficient (proportional to the total cross section) had a typical uncertainty of 3%, with some runs as high as 10%. This uncertainty was in many cases lower than the statistical yields of any given individual bar because we fit the distributions over the *entire array* of bars. To this 3% fit coefficient uncertainty, we must add in quadrature two independent systematic uncertainties in the simulation: 4% from the neutron detection efficiency (§3.a.5), and 4% reproducibility from the comparison of MCNP6 and GEANT

calculations (§3.a.6). We then converted the fit coefficient into the total cross section by dividing by the integrated beam current (§3.a.3) and target areal densities (§3.a.4). We therefore added in quadrature the uncertainties of the beam current (typically 0.1%, but in some cases up to 7%) and target thickness (2%). The typical uncertainty was therefore the sum in quadrature of 3% fitting, 4% intrinsic detector efficiency, 4% neutron detection efficiency, 0.1% beam current, and 2% target thickness, giving a total of 7% (Table 1). Some points have additions for larger fit uncertainty (up to 10%), larger beam current uncertainty (up to 5%), a correction for angular distribution effects (up to 10%, described in §3.a.10), or a correction for a sub-threshold energy level (up to 6%, described in §3.a.10). Overall, uncertainties ranged from 6% (minimum) to 7.55% (average) to 16% (maximum). A distribution of the uncertainties is shown in Fig. 3-10.

3.a.10. Specialized fits and limitations

The fits to a number of our *measured yield vs. angle* distributions required special treatment. This was largely due to our strategy of fitting the simulation to the distribution of *total* yield vs. angle: fitting to the sum of yields ignores the neutron yields to individual ^{22}Na levels. Because the *predicted yield per level per reaction vs. angle* distributions have very similar shapes (as shown in Fig. 3-11), there are ambiguities to the fits to the total yield per bar in some cases. Specifically, fits resulting in very different partial cross sections can combine to give (nearly) the same total cross section. A typical case is shown in Fig. 3-12, where the total cross section values arising from the different fits agree within uncertainties. To reduce ambiguities, we constrained the fit coefficients to roughly match the reactions to different ^{22}Na levels as indicated by the yields under the corresponding TOF spectrum peaks. For a number of reasons, however, this treatment was not possible for runs at all energies. For example, only a few of the levels gave appreciable yields in many cases; in others, our timing resolution prevented us from resolving the peaks in the TOF spectra; and in others, the variations in relative yields to different levels varied significantly across the array. We were able to deal with some of these cases by constraining partial cross sections to values similar to fit results at adjacent (*i.e.*, different by 25 keV) energy steps. We note that neutron distributions from the highest excited state do not suffer this ambiguity because the shape of those yield distributions are very forward focused due to the kinematics. Specifically, neutrons ejected at forward angles are above the detection threshold. Since the lower-energy neutrons from lower-lying ^{22}Na excited states or from the ground state ^{22}Na are above threshold at all angles, the shape from the highest excited state is easy to fit with less ambiguity. See §3.a.12 for a discussion of a complementary data analysis strategy that could avoid these ambiguities.

Another set of runs required specialized fits because of our assumption of isotropic yield distributions in the center-of-mass system. As shown in Fig. 3-13, our data clearly show anisotropies in neutron yields across the array at certain energies. These were typically a dipole distribution where the yield is enhanced at forward and backward angles. Our current analysis strategy, however, precludes the consideration of angular distribution effects. This is because the addition of the required multiple angular distribution fit coefficients for each level would enhance ambiguities in the fit coefficients beyond those already present when using a single fit coefficient (the partial cross section) per level. Since our neutron detector array covered a wide range of reaction angles (from 21 to 170 degrees), almost the entire angular distribution is evident. By running the fitting code as described in §3.a.7, the intensities of the center-of-mass distributions were effectively fit to an average yield of the array, with slightly larger error due to the poor shape of the overall fit (Fig. 3-14). No extra error was added for these points, but a note was kept to identify them in our final data set (§3.c).

Some runs required a different treatment due to enhanced yields at forward angles (Fig. 3-15). For these cases, we first fit the smoothly varying portion of the distribution, and subtracted this

from the measured yield distribution to determine the fraction of yield in the forward peak; this was typically 25% or less. We then scaled the result of the fit by the fraction of forward peak not accounted for by the first fit and added this to the fit to the smooth distribution. An extra uncertainty of half of the forward-only cross section was added in these cases, which was usually less than 12% of the total yield.

Another set of runs required specialized fits when the beam energy was slightly above the threshold for populating an excited level in ^{22}Na. In such cases, the reaction kinematics dictates that neutrons at forward angles are the only ones that have energies above our detection threshold. For these cases, a comparison of runs with increasing energy showed yields increasing in the forward bars (Fig. 3-16), and the corresponding simulations confirmed that this forward angle yield is a contribution of the highest excitation energy ^{22}Na level that can be populated at this beam energy. Because the *predicted yield per level vs. angle* distributions are relatively featureless for levels that are well above threshold, the standard fitting procedure would attribute any forward-angle feature to the near-threshold level. This, however, is problematic because these low energy neutrons are very sensitive to the rapidly decreasing intrinsic neutron detection efficiency near the detection threshold (Fig. 2-5). The result is that the standard fits give a significant over-enhancement of the predicted partial cross section to the near-threshold level. This was corrected by examining an average of the TOF yield to this level for a series of runs decreasing from 1 MeV down to the threshold for the level of interest. For almost all cases, it was found that the relevant TOF yields were reasonably consistent down to our detection threshold. We therefore constrained the fit coefficient to give the same partial cross section over this energy range, and added this amount (usually less than 20% of the total) to a separate fit of the featureless portion of the *measured yield vs. angle* distribution. For these runs, we included an uncertainty in the partial cross section corresponding to the spread of values from TOF peaks observed at higher energies, which was generally less than 10% of the partial cross section and less than 5% of the total cross section. This process is repeated for sub-threshold neutrons for even lower beam energies where no forward-angle neutrons are above the detection threshold but the beam energy is high enough to populate the excited level in ^{22}Na. Just as described above, the partial cross section to this excited state is kept constant. The data was subsequently analyzed without a calibrated threshold, thereby lowering the effective detection threshold to confirm that the neutron peaks appear for this high excitation level. It was discovered that about 250 to 300 keV above the beam-energy threshold for populating these levels, the intensity drops to zero. Therefore, the added partial cross section is only added for beam energies that actually indicate some intensity for populating that excitation level. Only half of the partial cross section was added when the uncalibrated spectra indicated the population to that level was measurably reduced and the next lowest energy point had no contribution.

3.a.11. Final cross section from alpha-beam experiment

The analysis procedure described above was repeated for all bombarding energies to build up the ^{19}F(α,n)^{22}Na excitation function. Fig. 3-17 shows the resulting cross section vs. energy, with uncertainties only arising from the fit (*i.e.*, no systematic uncertainties). Fig. 3-18 shows the cross section with all uncertainties included. The values are given in Table 2.

3.a.12. Complementary strategy for data analysis

A strategy for data analysis that is complementary to our fits of *measured yield vs. angle* distributions can be based on assigning a TOF value and a reaction angle to each event in the neutron detector, where the reaction angle is based on the position of the neutron event along the VANDLE bar. This position can be determined from the time difference between the top and bottom signals in the VANDLE bar PMTs. From the reaction angle and the TOF, the neutron

energy can be determined by reaction kinematics. The neutron energy and reaction Q-value then determine whether the neutron is from a reaction to the ^{22}Na ground state or to a particular excited state. For each level, the yields can be summed (binned) as a function of reaction angle, using the symmetry about the beam axis. These yields can then corrected for intrinsic detector efficiency. The angular distributions for each level can then be converted into the center-of-mass frame and fit with Legendre polynomials. Finally, these coefficients enable the yield at all angles (*i.e.*, the total yield into 4π,) to be calculated by integrating over a sphere to account for angular distribution effects. For each level, the partial cross section can then be determined by normalizing to the integrated beam current; the total cross section can be obtained by summing all the partial cross sections. This process can be repeated for all energies, constraining partial cross sections if necessary between angles. The advantages of this strategy include a complete utilization of neutron TOF information in determining partial cross sections, and the ability to determine the cross section without reliance on the MCNP6 simulation. This approach, however, does not include effects of scattering from the experimental setup or cross talk between the detectors in the array. We anticipate pursuing this complementary analysis strategy in the near future.

3.b. Fluorine-beam experiment relative cross section determination

3.b.1. Overview

The data from the fluorine-beam experiment consists of nearly 800 neutron TOF datasets (28 VANDLE bars (angles) x 28 beam energies) with some repeated, as well as 30 ^{22}Na datasets. We also collected 30 ^{19}F(α,α) scattering datasets simultaneously with the ^{22}Na and neutron datasets from ^{19}F(α,n), as well as over 50 ^{19}F(α,α) datasets from a separate measurement of only the scattering excitation function. Our data analysis approach has three components. First, we used our ^{19}F(α,α) excitation function datasets to determine the scattering yield per Coulomb of integrated beam current at a standard target thickness spanning the range of energies where we measured ^{19}F(α,n) (§3.b.3). Then we identified and counted ^{22}Na ions in the spectra from the gas ionization counter at the DRS focal plane, along with the simultaneous alpha yield from ^{19}F(α,α), to determine the number of ^{22}Na per scattered alpha at each energy where we measured ^{19}F(α,n) (§3.b.4). By dividing by the corresponding scattered alphas per Coulomb at that energy from the scattering excitation function, we determine the ^{22}Na yield per Coulomb. We also determined the TOF spectrum of all neutron events in the VANDLE array that are in time coincidence with the identified ^{22}Na ions in each ^{19}F(α,n) run (§3.b.5). We summed up the neutron counts in each TOF peak to get the total neutron yield per scattered alpha at each energy. We then divided this result by the corresponding scattered alphas per Coulomb to determine the ^{22}Na-gated neutron yield per Coulomb. Finally, we combined these relative yields and then converted to a cross section via comparison to the results from the alpha-beam experiment.

3.b.2. Recoil acceptance

As mentioned in §2.c, the angular acceptance of the DRS is not large enough to capture all of the ^{22}Na recoils from the ^{19}F(α,n)^{22}Na reaction. The DRS system is optimized for the detection of recoils from capture reactions (*e.g.*, (p,γ) reactions) that typically have opening angles of 0.5 degrees or less, well within the ±2.6 degree angular acceptance. For such reactions, the DRS acceptance is 100% and is insensitive to the tuning of the beam. Because the opening angle of the ^{19}F(α,n)^{22}Na reaction is 4 degrees (Fig. 3-19), the DRS acceptance is not sufficiently large to capture all of the ^{22}Na recoils. Furthermore, the percentage of recoils transmitted to the focal plane has a dependence on the beam tune as well as a (slow) dependence on the reaction kinematics (*i.e.*, the beam energy). We addressed this issue by optimizing the DRS acceptance at the lowest energy of each of the 4 fluorine-beam energy regions (5.300, 5.910, 6.075, and 6.530 MeV). This optimization was done by varying both beam tune and DRS ion-optical parameters

and choosing the parameters giving the maximal yield. With these settings, we then measured the ^{22}Na yields and ^{22}Na-neutron coincident yields over a series of energies in small steps. We monitored the particle ID spectrum (Fig. 2-19) from the gas ionization counter for qualitative changes during these runs as a diagnostic of the acceptance. For measurements at energies within ~70 keV of the lowest energy in this region (where the yield was optimized), there were no significant qualitative changes in the particle ID spectrum appeared, and the DRS acceptance was deemed to be constant over this range. This enabled us extract a set of *relative* (rather than absolute) ^{22}Na yields and ^{22}Na-neutron coincident yields for this series of measurements. As the beam energy was increased beyond ~70 keV above the optimized energy, however, significant qualitative changes in the particle ID spectrum appeared due to a change in the DRS acceptance. Points at those higher energies could not be combined with those at lower energies to determine a relative yield and were not included in our analysis.

3.b.3. Beam current and target thickness normalization

During our ^{19}F(α,n) measurements, we cannot measure the integrated beam current directly, and therefore cannot directly determine the reaction yield per Coulomb of integrated beam. This is because the beam and the ^{22}Na recoils enter the DRS and are focused in different directions; we cannot run the beam into a Faraday cup as we did in the alpha-beam experiment. As mentioned in §2.c, to provide a normalization for our runs, we make a simultaneous measurement of ^{19}F(α,n) and ^{19}F(α,α) scattering at each energy, and use the scattered alphas as an indicator of the integrated beam current. A typical ^{19}F(α,α) scattering spectrum is shown in Fig. 2-13. These yields were determined for each run, and typical statistical uncertainties were 0.2%, with all being less than 1%. The connection between scattered alpha yield and integrated beam current (scattering yield per Coulomb) is given by our separate measurement of ^{19}F(α,α) scattering over the entire energy range of our experiment. This enables us to account for the non-Rutherford nature of the reaction in this energy range. The excitation function for this measurement, shown in Fig. 3-20, exhibits the expected interference patterns between resonant and elastic scattering [Bla52]. We note that since the scattering yield is also directly proportional to the ^{4}He gas pressure, this approach of normalizing the ^{19}F(α,n) yields per scatter by the scatters per Coulomb also normalizes to the ^{4}He gas target thickness. Our statistical uncertainties were less than 1% for this scattering measurement. The beam was run into a Faraday cup and the current routed to a Beam Current Integrator module and then into our data stream where it was digitized; uncertainties were based on the digitization accuracy and were less than 0.5%. Scattering measurements at 12 energies were repeated (often two times, and in some cases three times) to determine a systematic uncertainty based on the spread of values around their mean; this was 6%, yielding a combined statistical and systematic uncertainty (added in quadrature) of 6% for this normalization. Since we used smaller energy steps in our ^{19}F(α,n) measurement than we did for our ^{19}F(α,α) excitation function measurement, we performed linear interpolations as necessary to determine the ^{19}F(α,α) yield per Coulomb at each of the energies of our ^{19}F(α,n) measurements. For those cases, we properly included the uncertainty of the interpolation added in quadrature with the average of the uncertainties of the data points used for the interpolation.

3.b.4. ^{22}Na relative yields

The ^{22}Na yields were determined by counting events above background within the appropriate two-dimensional gate or "window" in the energy loss vs. total energy plot (Fig. 3-21) used for particle identification in the gas ionization counter at the DRS focal plane. Typical statistical uncertainties were approximately 0.5%, and most runs were less than 1%. There are additional uncertainties arising from the event selection in the two-dimensional plot. We determined these by adjusting the ^{22}Na window to have maximal and minimal sizes (Fig. 3-21), where the maximal size included all ^{22}Na particles as well as some of the scattered ^{19}F beam particles, and the

minimal size omitted some ^{22}Na particles in order to remove all possible scattered ^{19}F. As this variation represents a three-sigma uncertainty, the resulting ^{22}Na yield variations were divided by a factor of three to determine the one-sigma uncertainties. These uncertainties were typically 7% and ranged from 1% to 9% for all the runs. We then divided these yields by the scattering yield measured in the same run (§3.b.3) to determine the ^{22}Na yield per scatter. Finally, we then divided this by the appropriate scatter per Coulomb value (§3.b.3) from our measurement of the ^{19}F(α,α) excitation function to get the ^{22}Na yield per Coulomb. This is a relative cross section determination. Uncertainties for yields, yields per scatter, and scatters per Coulomb were combined in quadrature and were dominated by the 7% identification uncertainty and 6% systematic (reproducibility) uncertainty; they average at 9% and some are as high as 11%. Note that no simulations or fits were required to determine these ^{22}Na yields. Figs. 3-22 to 3-25 show the ^{22}Na yield per Coulomb as function of energy as measured at DRS focal plane in the gas ionization counter, at energies near 5.300, 5.910, 6.075, and 6.530 MeV, respectively. These represent the relative cross section values based on our measurement of ^{22}Na recoils. The typical uncertainties are listed in Table 3, and the values are given in Table 4.

3.b.5. Neutron relative yields

At each energy in the fluorine-beam experiment, we examined the 28 neutron TOF spectra from the VANDLE bars that had events in time coincidence with an event in the ^{22}Na particle identification window from the gas ionization counter spectrum. The time coincidence resulted in these ^{22}Na-gated neutron TOF spectra (Fig. 3-26) having a significantly lower background (typically less than 1% of the total) than the background in the TOF spectra in the alpha-beam experiment. The background was fit and subtracted from the TOF spectra, and the total number of counts above background (for reactions proceeding to all ^{22}Na levels combined) was determined by summing under the histogram peaks. There was no need for TOF spectra fits to determine these total neutron yields. We varied the ^{22}Na particle identification window as described above in §3.b.4 and found no significant difference (less than 2%) in the total neutron yields. Statistical uncertainties ranged from 1 – 5% for the total neutron yields per bar. Since we are determining relative yields as a function of bombarding energy, no simulation on neutron yield per bar was required. The ^{22}Na–gated neutron yields were divided by the simultaneously measured alpha scattering yield to get neutrons per scatter, and then this was divided by the appropriate scatter/Coulomb to determine the ^{22}Na–gated neutron yield per Coulomb. Uncertainties were combined in quadrature for the neutron yields, the scattering yields, and the scatter/Coulomb value, and were typically 3% and ranged from 1 to 5%. Figs. 3-27 to 3-30 show the ^{22}Na-gated neutron yields per Coulomb as function of energy, at energies near 5.300, 5.910, 6.075, and 6.530 MeV, respectively. These represent the relative cross section values based on our measurement of ^{22}Na-gated neutrons. The typical uncertainties are listed in Table 5, and the values are given in Table 6.

3.b.6. Combined relative yields and uncertainties

Comparisons of our relative cross sections based on ^{22}Na yields and on ^{22}Na-gated neutron yields as a function of energy are given in Figs. 3-31 to 3-34 at energies near 5.300, 5.910, 6.075, and 6.530 MeV, respectively. In these plots, we have normalized the ^{22}Na-gated neutron yields/Coulomb by a scale factor chosen to minimize the sum of the variances between these two relative cross section data sets. A different scale factor is used in each of the four energy regions. Values are given in Table 7. We then combined these two data sets by a weighted average, where the weighting was based on the Na or neutron yields. The results are shown in Figs. 3-35 to 3-38 for energies near 5.300, 5.910, 6.075, and 6.530 MeV, respectively. For these points, the uncertainties are not added in quadrature, since many of the same uncertainties appear in both the ^{22}Na and neutron yield points. We therefore increased the uncertainties appropriately by

combining all the *unique* component uncertainties in Tables 3 and 5. Typical values are statistical yield uncertainties (0.5% ^{22}Na, 3% neutrons), beam current and target thickness normalization (0.2%), ^{22}Na identification (7% as needed), reproducibility (6%), averaging (< 1% as needed), and interpolation (< 2% as needed). Some points have larger statistical uncertainties for neutrons (up to 5%), larger ^{22}Na identification uncertainties (up to 9%). The final uncertainties range from 6.5% (minimum), to 9% (average), to 11% (maximum). The data points for these plots are given in Table 8.

3.c. Combined cross section determination

We normalized the relative cross section values from fluorine-beam experiment (§3.b.6, Figs. 3-35 to 3-38, Table 8) to the absolute cross sections determined from the alpha-beam experiment (§3.a.11, Fig. 3-18, Table 2) in order to determine absolute cross sections from the fluorine-beam experiment. Each of the four energy ranges in the fluorine-beam experiment has a different normalization factor, based on a minimization of the sum of the variances between the scaled fluorine-beam data with the nearest neighbors of the alpha-beam data. We increased the uncertainties on the fluorine-beam experiment data points appropriately by including a normalization uncertainty with the data point uncertainty. The absolute cross sections as a function of energy resulting from scaling the fluorine-beam experiment relative cross sections to the absolute cross sections from the alpha-beam experiment are shown in Figs. 3-39 to 3-42 at energies near 5.300 MeV, 5.910, 6.075, and 6.530 MeV, respectively. The values are given in Table 9.

The result of the analysis described above can be expressed as one absolute cross section data set that combines the results of the alpha-beam and fluorine-beam experiments. This is shown in Fig. 3-43 with all uncertainties, and in Fig. 3-44 without systematic uncertainties. For clarity, Fig. 3-43 is expanded into two portions in Fig. 3-45 and Fig. 3-46. The distribution of percent uncertainties in this final data set is shown in Fig. 3-47; the average uncertainty is 7.6%. The cross section values with uncertainties are given in Table 10. Table 11 gives details for each data point in our final cross section plot Fig. 3-43. These details include the origin of the point (alpha-beam experiment, fluorine-beam experiment), special fitting requirements (forward-peaked, angular distribution, sub-threshold Na levels), merged data points, uncertainty notes, uncertainty terms, and other notes.

4. COMPARISON TO OTHER WORKS

We present a comparison of our cross section (Table 10, Fig. 3-43) with those of a number of previous studies. Fig. 4-1 shows our cross section compared to the thick target result of Norman *et al.* [Nor84]. In Fig. 4-2, we take a 250-keV energy average of our result and compare to Norman *et al.* [Nor84]. A linear regression of our energy average is 63.3 mb/MeV, compared to 102 mb/keV in [Nor84]. Fig. 4-3 shows our result overlaid with the thin-target measurement of Balakrishnan *et al.* [Bal78]. In Fig. 4-4, we show our result with the TALYS-calculated cross section the TENDL 2015 library [TEN15]. Our measurement is compared to the evaluation in JENDL [Mur06] in Fig. 4-5. Finally, in Fig. 4-6, our work is compared to the evaluation of Vukulov *et al.* [Vuk83].

5. IMPLICATIONS FOR NON-DESTRUCTIVE ASSAY STUDIES

5.a. Cross Section Processing

Our study has produced a total cross section for the ^{19}F(α,n)^{22}Na reaction for alpha energies ranging from 3.9 – 6.7 MeV. This cross section must, however, be processed to enable its use for the development and optimization of NDA detection systems. The results of our study will be combined with previous works in a formal evaluation endorsed by the Cross Section Evaluation

Working Group (CSEWG) [CSE16] for eventual release into a new revision of the Evaluated Nuclear Data File (ENDF) [END16]. We have processed our data into an "evaluation-ready" ENDF format, augmenting it with existing JENDL produced data [JEN05] as a first step, and made it immediately available [INL16] to researchers with the caveat that this is unevaluated data.

Nondestructive assay system performance analysis is most commonly determined via simulations with the Monte Carlo N-Particle (MCNP) transport code [MCN14] developed at Los Alamos National Laboratory. These types of analyses use MCNP to span measurement and system parameter space with simulations and are typically complemented with benchmark measurements to ensure model accuracy. Past versions of MCNP have used mathematical models in the transport of protons and heavier ions. These models were developed for high-energy physics applications and are known to be inaccurate at energies below 100 MeV. As of version 6.1, MCNP now permits the use of tabulated nuclear data for heavy ion transport in the same manner it does for neutron and photonuclear interactions, allowing for the use of measured cross sections like that for the $^{19}F(\alpha,n)^{22}Na$ reaction obtained in this study.

The MCNP code relies on data that has been translated into a pointwise continuous-energy format that is fit to an energy grid that allows for linear interpolation between data points. This format, referred to as an ACE file (A Compact ENDF), requires the dataset to include total, scattering, and particle production cross sections for implementation in MCNP. These files can be readily produced from existing ENDF formatted data using the ACER module of the NJOY nuclear data processing system [NJOY]. An ACE file has been created from the TENDL-augmented ENDF data set for use by researchers [INL16], again with the caveat that this file contains cross sections that have yet to be evaluated by the nuclear data community.

5.b. Simulations

We performed simulations to demonstrate the impact of our new cross section on NDA applications. The neutron emission rate from UF_6 (in units of neutrons per second per gram) was chosen as a first metric. In 1984, Sampson measured the neutron emission rates of UF_6 for several ^{235}U enrichments that ranged from approximately 0.2% to 97.7% [Sam84]. Enrichments of 3.0% and 57.38% were chosen as starting points for this demonstration because (a) the neutron emission rate has been shown to increase dramatically with increasing enrichment at lower enrichments values, and (b) 57.38% falls into a range of enrichments in which the neutron emission rate is fairly linear [PAN91]. A small 100g sphere (1.6739-cm radius) of solid UF_6 was modeled to minimize multiplication effects and isolate the neutron production rate from the $^{19}F(\alpha,n)^{22}Na$ reaction. Neutron emissions from spontaneous fission reactions were also ignored in this simulation. The neutron emission rate was calculated using our TENDL-augmented cross section at the two described enrichments and compared to calculations using default MCNP6 physics models and the original TENDL cross section. The simulation geometry is shown in Fig. 5-1, detailing the spherical surface in the airspace surrounding the UF_6 sphere used to tally the neutron emissions exiting the material.

We first found that simulations using the default MCNP6 physics model produced no $^{19}F(\alpha,n)^{22}Na$ neutrons in the airspace, even after billions of trial particles. It is unclear at this point whether the default model is drastically underestimating the reaction cross section, or if it simply does not account for this reaction in fluorine. Next, a simulation was made using the TENDL 2015 $^{19}F(\alpha,n)^{22}Na$ cross section as input [TEN15], followed by simulations where this input was increased and decreased by 25% in accordance with a recent assessment of the $^{19}F(\alpha,n)^{22}Na$ cross section uncertainty [LaF13]. These three calculations, at a maximum, central, and minimum value

(±1 sigma), enabled us to determine the impact on the neutron emission rate of the previous ± 25% uncertainty in the $^{19}F(\alpha,n)^{22}Na$ cross section to be 50% for the LEU sphere (3% enrichment) and 51% for the HEU sphere (57.38% enrichment); the results are given in Table 12 and plotted in Fig. 5-2. This uncertainty is in rough agreement with to the results of Miller *et al.* [Mil14] who found a spread of a factor of 1.4 between neutron yields in an NDA simulation calculated with different input $^{19}F(\alpha,n)^{22}Na$ cross sections.

Next, we repeated this process using the $^{19}F(\alpha,n)^{22}Na$ cross section from our present study (Table 10, Fig. 3-43), and values that were increased and decreased by 7% in accordance with the average uncertainty of our measurement. Comparing simulations with our cross section and the TENDL cross section (Table 12), we find that the neutron emission rate is reduced by 10% for the LEU sphere and 12% for the HEU sphere (Fig. 5-2). Finally, comparing simulations with an input cross section at our maximum (+1 sigma) and minimum (-1 sigma) values, the uncertainty in the neutron emission rate is 13% for the LEU sphere and 14% for the HEU sphere. This is a reduction in neutron emission uncertainty caused by the $^{19}F(\alpha,n)^{22}Na$ cross section by a factor of 3.6.

MCNP6 model geometries have also been generated for a suite of standard UF_6 storage cylinders. A study to assess the impact of our new $^{19}F(\alpha,n)^{22}Na$ cross section on NDA measurements will be the subject of an article submitted to Applied Radiation and Isotopes in Fall 2016.

6. SUMMARY

Neutrons from the $^{19}F(\alpha,n)^{22}Na$ reaction are used as the basis of a self-interrogating non-destructive assay (NDA) technique. The accuracy of these assays is now improved by our measurements of the $^{19}F(\alpha,n)^{22}Na$ reaction with both ^{4}He and ^{19}F beams. We have determined an absolute cross section for the $^{19}F(\alpha,n)^{22}Na$ reaction to an average precision of 7.6% over the alpha energy range of 3.9 – 6.7 MeV that encompasses common actinide alpha decay needed for NDA studies. We utilized this cross section in a simulation of a 110 g spherical UF_6 assembly and obtained a change in neutron emission rate values of approximately 10-12%, and a significant (factor of 3.6) decrease in the neutron emission rate uncertainty (from 50-51% to 13-14%), compared to simulations using the old cross section. Our new absolute cross section enables improved interpretations of NDAs of containers of arbitrary size and configuration.

REFERENCES

[Ago03] S. Agostinelli *et al.*, Nucl. Inst. Meth. **A506** (2003) 250.
[And77] Andersen, H.H., Ziegler, J.F., 1977. The Stopping Powers and Ranges of Ions in Matter, Vol. 4. Pergamon, New York.
[Apr14] A. Aprahamian, P. Collon, M. Wiescher, Nuclear Physics News **24** (2014) 5.
[Bai79] J.K. Bair, J. Gomez del Campo, Nucl. Sci. Eng. **71** (1979) 18.
[Bal78] M. Balakrishnan, S. Kailas, M.K. Mehta, Pramana **10** (1978) 329.
[Bas15] M.S. Basunia, Nuclear Data Sheets **127** (2015) 69.
[Bla52] J.M. Blatt, L.C. Biedenharn, Rev. Mod. Phys. **24** (1952) 258.
[Bur15] http://www.burtonsys.com/climate/composite_standard_deviations.html
[Cha14] K.Y. Chae *et al.*, Nucl. Inst. Meth. **A715C** (2014) 6.
[Che10] J. Cheathan, J.C. Wagner, Proc. INMM 51st Ann. Meeting, Baltimore, MD, July 11–15 (2010).
[Chi09] K.A. Chipps *et al.*, Phys. Rev. C **80** (2009) 065810.
[Chi14] K.A. Chipps *et al.*, Nucl. Inst. Meth. **A763** (2014) 553.
[Cro97] S. Croft, EUR 17665 EU, Proceedings of the 19th Annual Symposium on Safeguards and Nuclear Material Management, Montpellier, France, 1997 May 13-15, p. 397.
[Cro03] S. Croft, L.C-A. Bourva, C.G. Wilkins, Proc. 25th Ann. ESARDA Meeting, Stockholm, Sweden, 13-15 May 2003.
[CSE16] Cross Section Evaluation Working Group (CSEWG) http://www.nndc.bnl.gov/csewg/
[Fen14] Michael Fensin, LANL (private communication) (2014).
[Fir07] R.B. Firestone, Nuclear Data Sheets **108** (2007) 1.
[Hsu78] S.T. Hsue, T.W. Crane, W.L. Talbert Jr., J.C. Lee, LANL Report LA-6923 (1978).
[IAE94] IAEA-TECDOC-771 (1994).
[INL16] Contact Scott Thompson, INL, scott.thompson@inl.gov
[Jac83] G.J.H. Jacobs, H. Liskien, Ann. Nucl. Energy **10** (1983) 541.
[JEN14] Japanese Evaluated Nuclear Data Library (JENDL) http://wwwndc.jaea.go.jp/jendl/j40/j40.html
[Jon86] C.M. Jones *et al.*, Nucl. Instrum. Meth. A **244** (1986) 7.
[Kim08] K.D. Kimball, I.C. Gauld, Trans. Amer. Nuclear Soc. **98** (2008) 214.
[LaF13] A.M. LaFleur, S. Croft, R.L. Mayer, M.T. Swinhoe, D.R. Mayo, B.A. Sapp, Proc. 3rd Int. Conf. Advancements in Nuclear Instrumentation Measurement Methods and their Applications (ANIMMA), IEEE (2013) 1.
[LUX] Luxel Corporation http://luxel.com
[Mac11] E. K. Mace *et al.*, Proc. INMM Annual Mtg., Palm Desert, California, July 17–21, 2011, Institute of Nuclear Materials Management.
[MCN14] MCNP, Los Alamos National Laboratory report LA-CP-14-00745, Rev. 0, June 2014.
[Mel66] A. Melissinos, "Experiments in modern physics: Rutherford scattering," Academic Press (1966) Chap. 6, pp. 226–252.
[Mil10a] K.A. Miller *et al.*, J. Nuclear Materials Management **39** (2010) 21.
[Mil10b] K. A. Miller *et al*., Proc. IAEA Symp. International Safeguards, Vienna, Austria, November 1–5, 2010, International Atomic Energy Agency.
[Mil12] K.A. Miller, LA-UR-12-21067 (2012)
[Mil14] K.A. Miller, M.T. Swinhoe, S. Croft, Nucl. Sci. Eng. **176** (2014) 98.
[Mur06] T. Murata, H. Matsunobu, K. Shibata, JAEA 2006-052 (2006).
[NJOY] NJOY http://t2.lanl.gov/nis/njoy/theindex.html
[Nor84] E.B. Norman *et al.*, Phys. Rev. C **30** (1984) 1339.
[Nor15] E.B. Norman *et al.*, Appl. Radiation Isotopes **103** (2015) 177.
[PAN91] D. Reilly, N. Ensslin, H. Smith, "Passive Nondestructive Assay of Nuclear Materials," NRC FIN A7241 (1991) 407.

[Ped07] B. Pedersen , W. Hage , A. Favalli , G. Varasano, Proc. Int. Safeguards Symp. Addressing Verification Challenges, IAEA, October 2006, IAEA-CN-148/52 (2007)
[Pet16] W.A. Peters *et al.*, Nucl. Inst. Meth. **A** (2016) submitted.
[Root] 30 https://root.cern.ch/
[Sam84] T.E. Sampson, Nucl Sci. and Eng. **54** (1984) 470.
[Sha05] D. Shapira *et al.*, Nucl. Instr. Meth. **A551** (2005) 330.
[Smi14] L.E. Smith *et al.*, PNNL-SA-105136, https://www.iaea.org/safeguards/symposium/2014/home/eproceedings/sg2014-slides/000287.pdf
[TAL16] TALYS reaction code http://www.talys.eu/fileadmin/talys/user/docs/talys1.8.pdf
[TEN12] TALYS Evaluated Nuclear Data Library (TENDL) 2012 ftp://ftp.nrg.eu/pub/www/talys/tendl2012/alpha_file/F/019/lib/endf/F019-a.tendl
[TEN15] TALYS Evaluated Nuclear Data Library (TENDL) 2015 https://tendl.web.psi.ch/tendl_2015/tendl2015.html
[van15] Q. van den Berg, S. Simakov, INDC(SEC)-0111 (2015).
[Vuk83] V.A. Vukulov *et al.*, Voprosy Atomnoy Nauki i Tekhniki, Seriya Obshch. **4/25** (1983) 31.
[Wil02] W.B. Wilson *et al.*, LA-UR-02-1839.
[Wre00] P.R. Wrean, R.W. Kavanagh, Phys. Rev. C **62** (2000) 055805.
[Yam90] N. Yamamuro, JAERI-M 90-006 (1990).

FIGURES

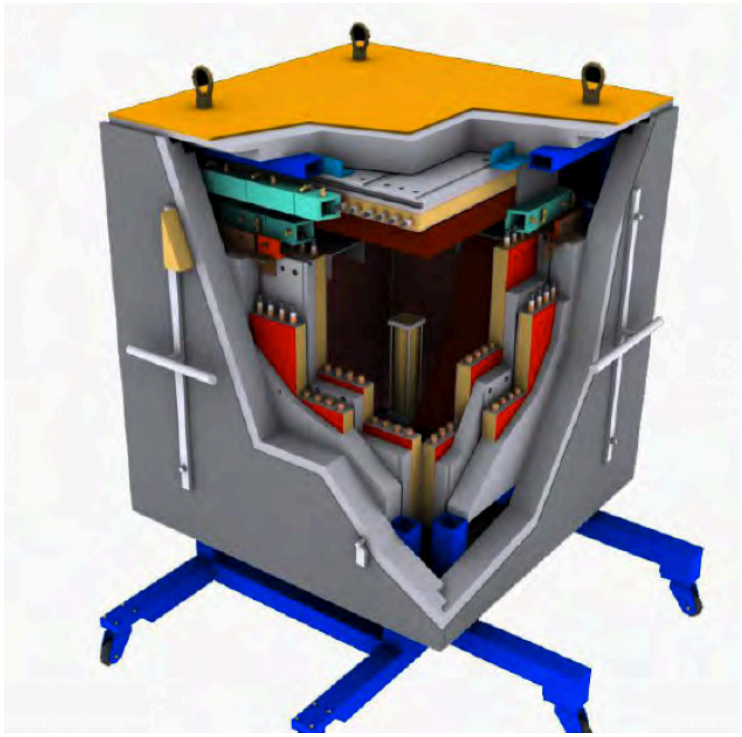

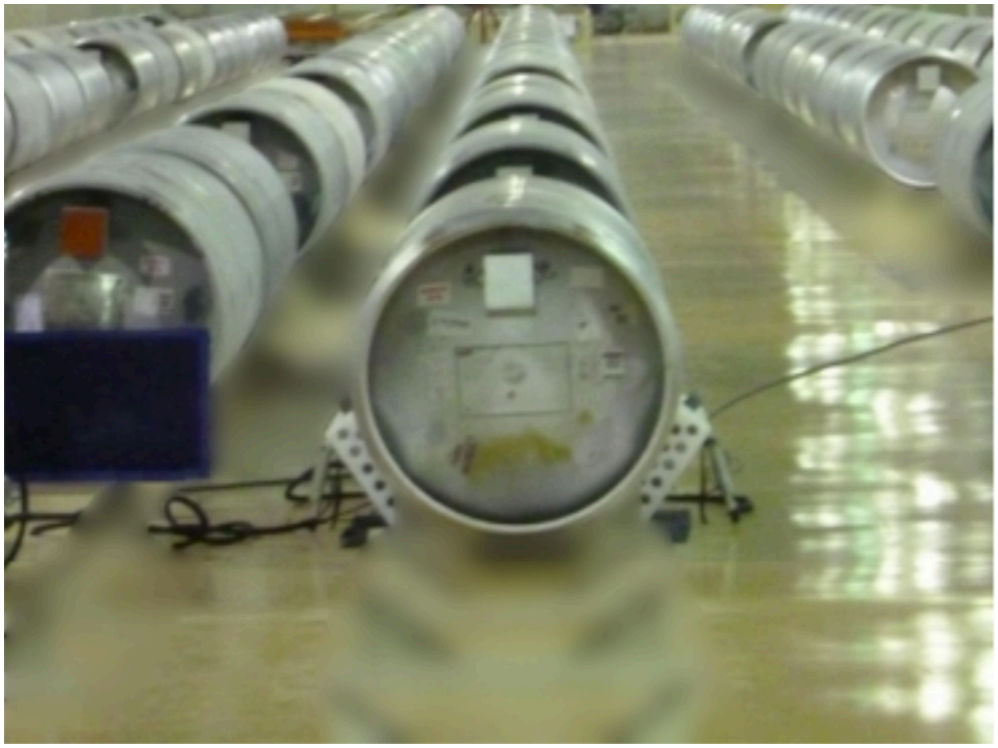

Fig. 1-1. PUNITA non-destructive assay (NDA) system with an external (pulsed neutron generator) radiation source (top) [Ped07]; a passive, self-interrogating NDA setup on a Model 30B UF_6 container at Rokkasho enrichment plant (bottom) [Mil12].

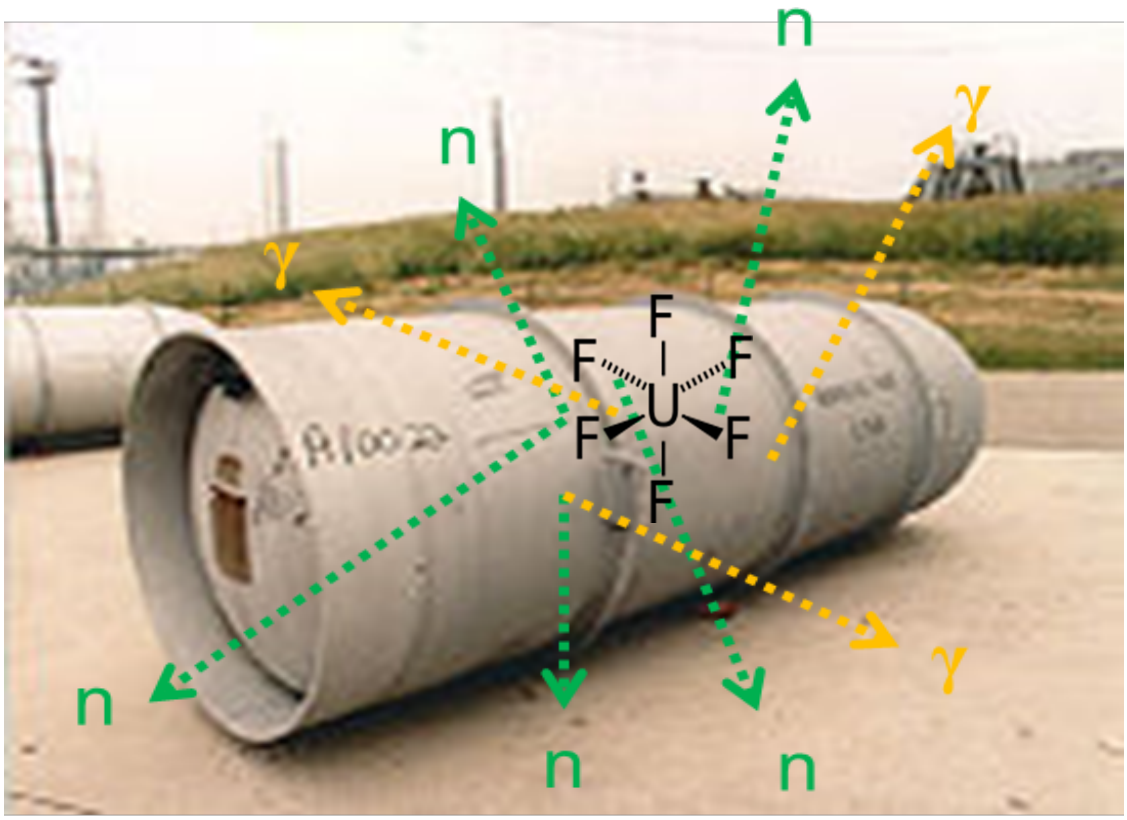

Fig. 1-2. Model 30B UF_6 container showing schematic neutron and gamma emission from the decays and reactions occurring within the container.

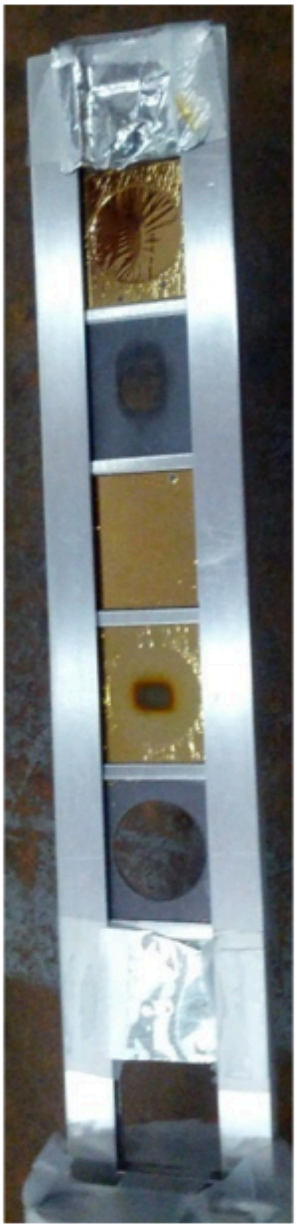

Fig. 2-1. Target ladder for the alpha-beam experiment including LaF_3 target (with gold backing) in the third position from the bottom.

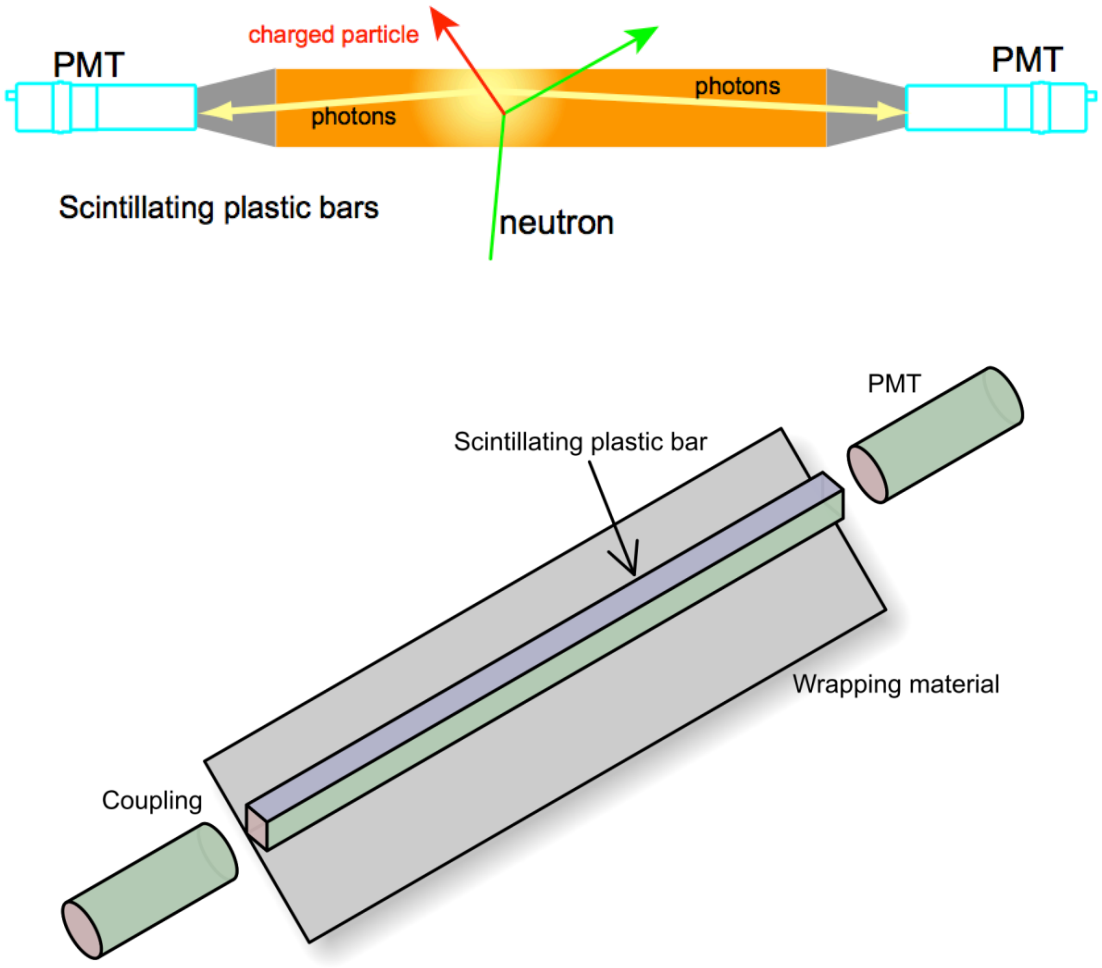

Fig. 2-2. Diagram of a standard plastic scintillator neutron detector bar (top) and a drawing of the components of one VANDLE module [Pet16].

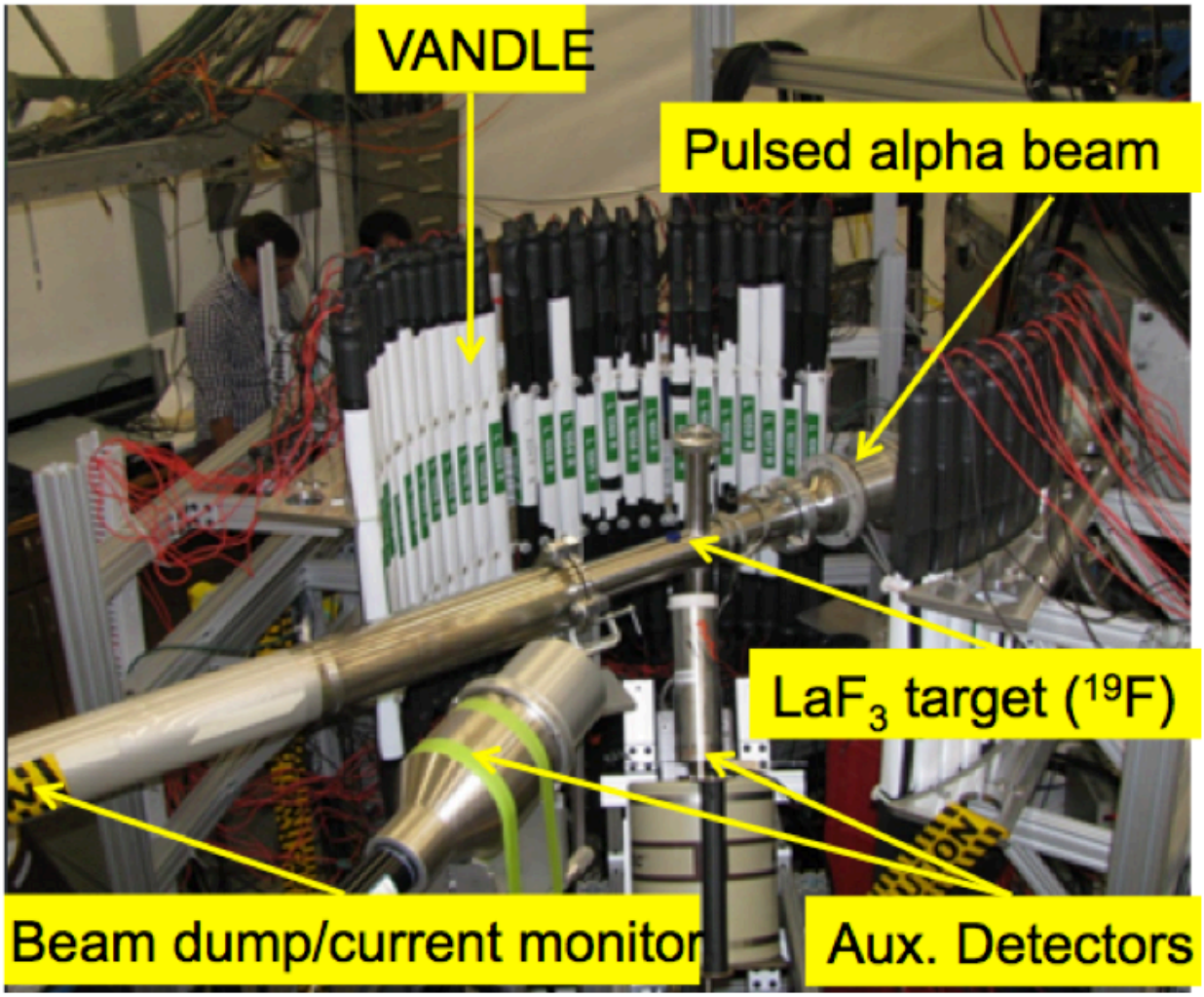

Fig. 2-3. VANDLE detector arrangement for the alpha-beam experiment.

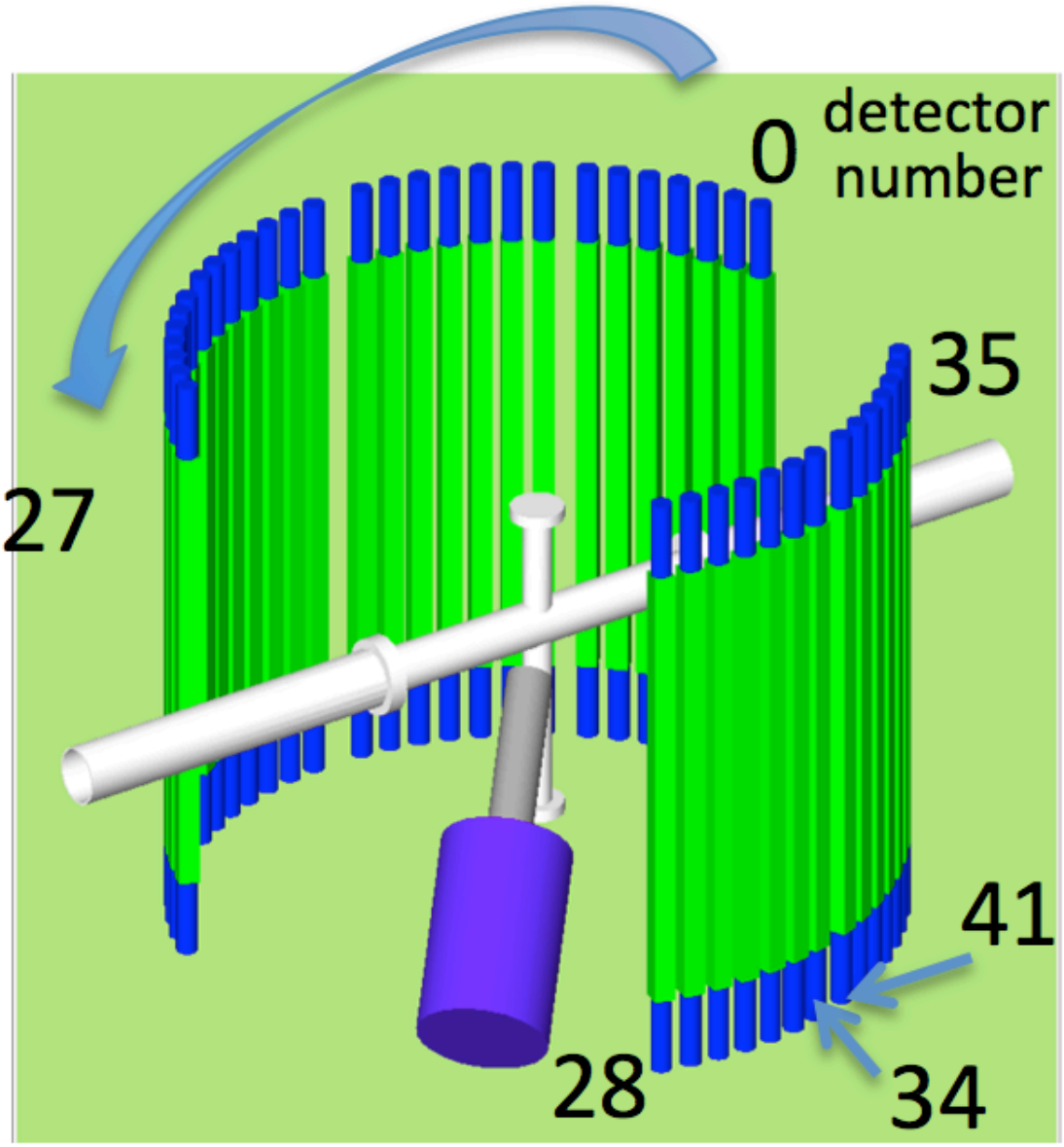

Fig. 2-4. VANDLE detector bar numbering scheme for the alpha-beam experiment.

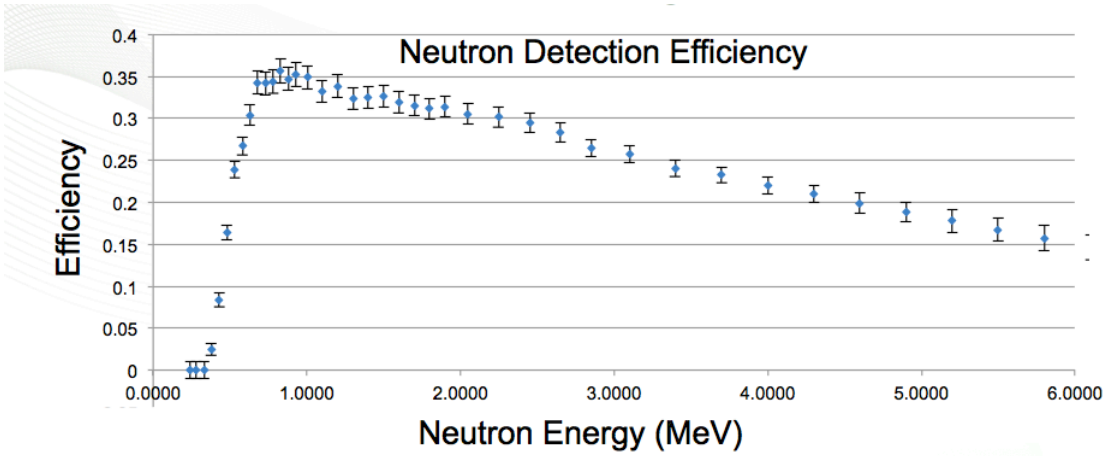

Fig. 2-5. VANDLE efficiency calibration with 60 keVee (electron equivalent energy) threshold [Pet16].

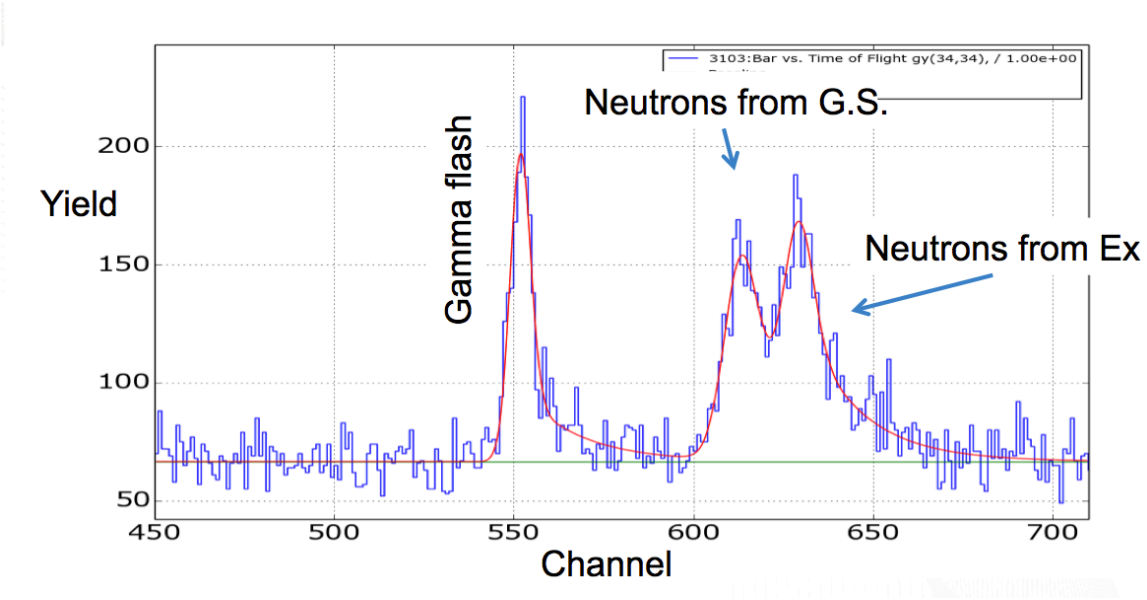

Fig. 2-6. Representative neutron TOF spectrum from one VANDLE detector bar.

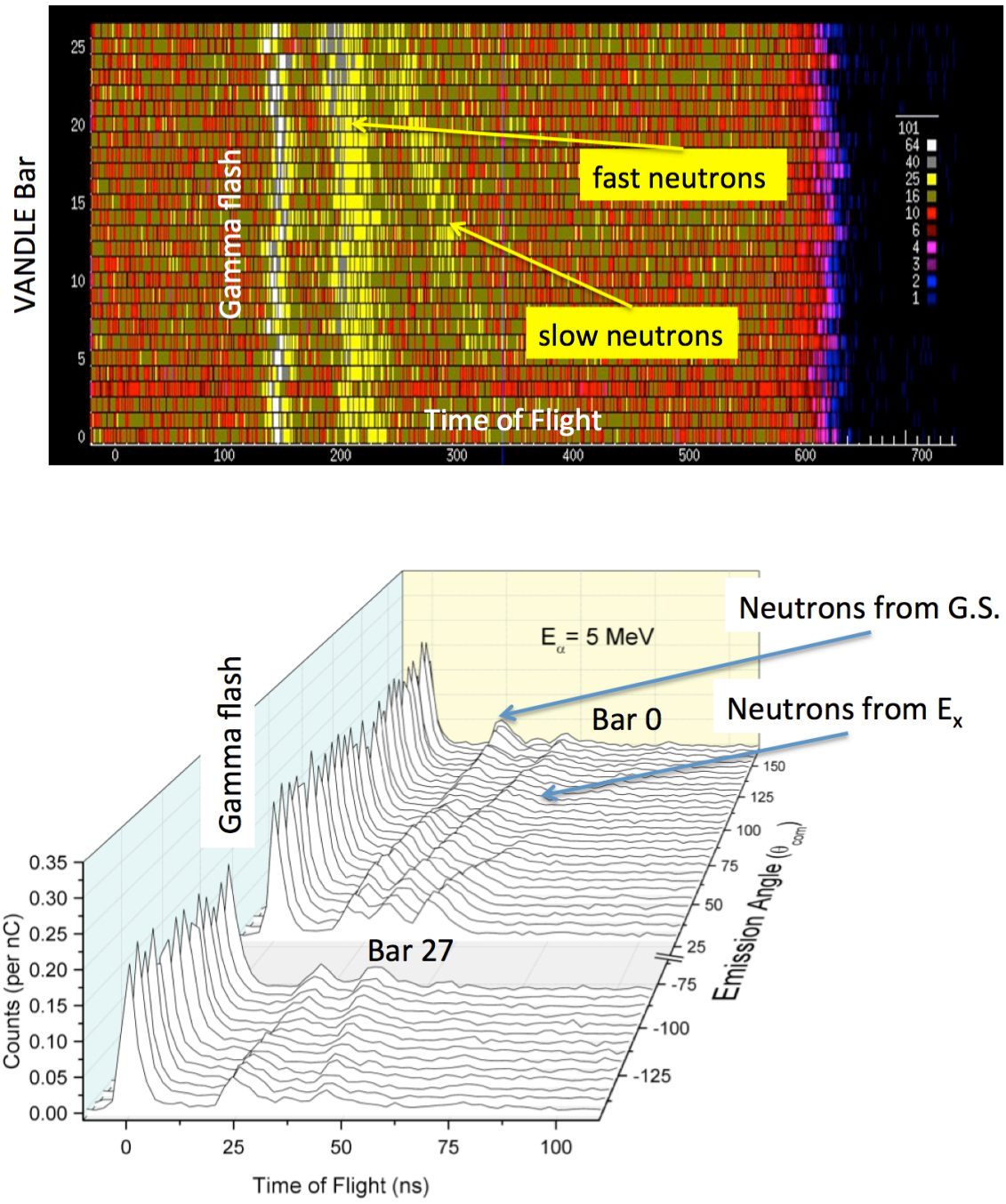

Fig. 2-7. Raw TOF spectra for the VANDLE array showing gamma flash, faster neutrons to the ^{22}Na ground state, and slower neutrons to excited states in ^{22}Na; shown in a 2-dimensional projection (top) and a 3-dimensional plot (bottom).

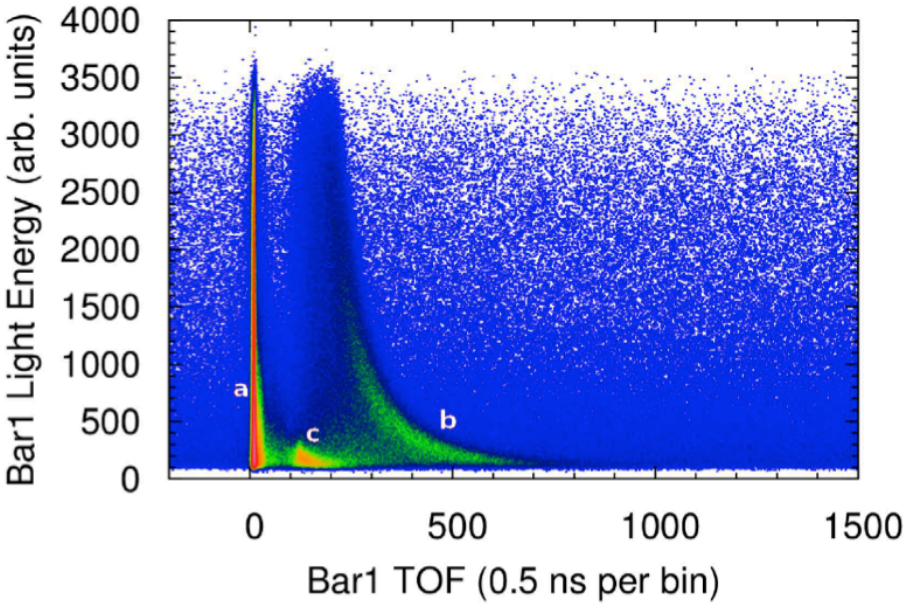

Fig. 2-8. Neutron-gamma discrimination with VANDLE: (a) gamma-rays from the target arrive at VANDLE first (gamma flash); (b,c) neutrons scatter off protons and carbon nuclei that in turn induce scintillation light yield depending on their energy.

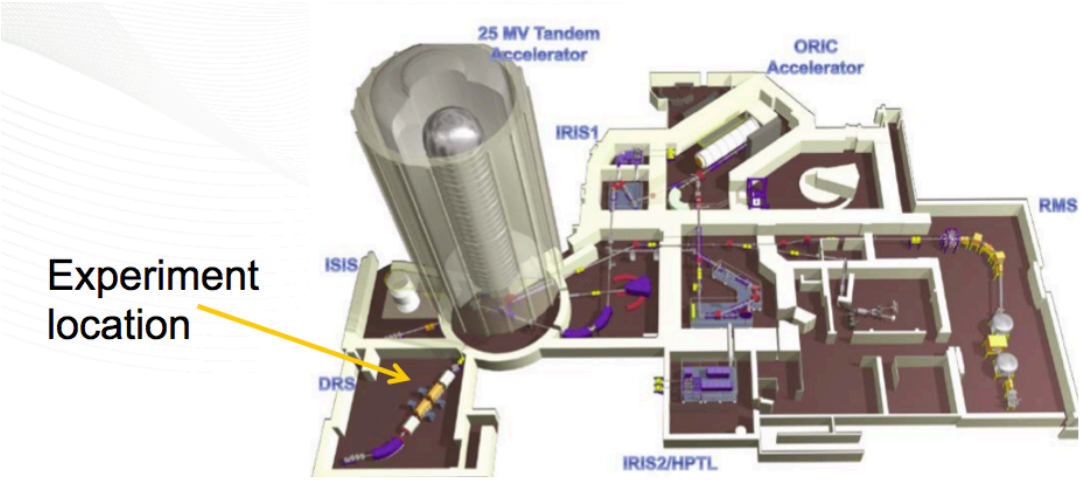

Fig. 2-9. Floor plan of the accelerator laboratory in the ORNL Physics Division used for the fluorine-beam experiment.

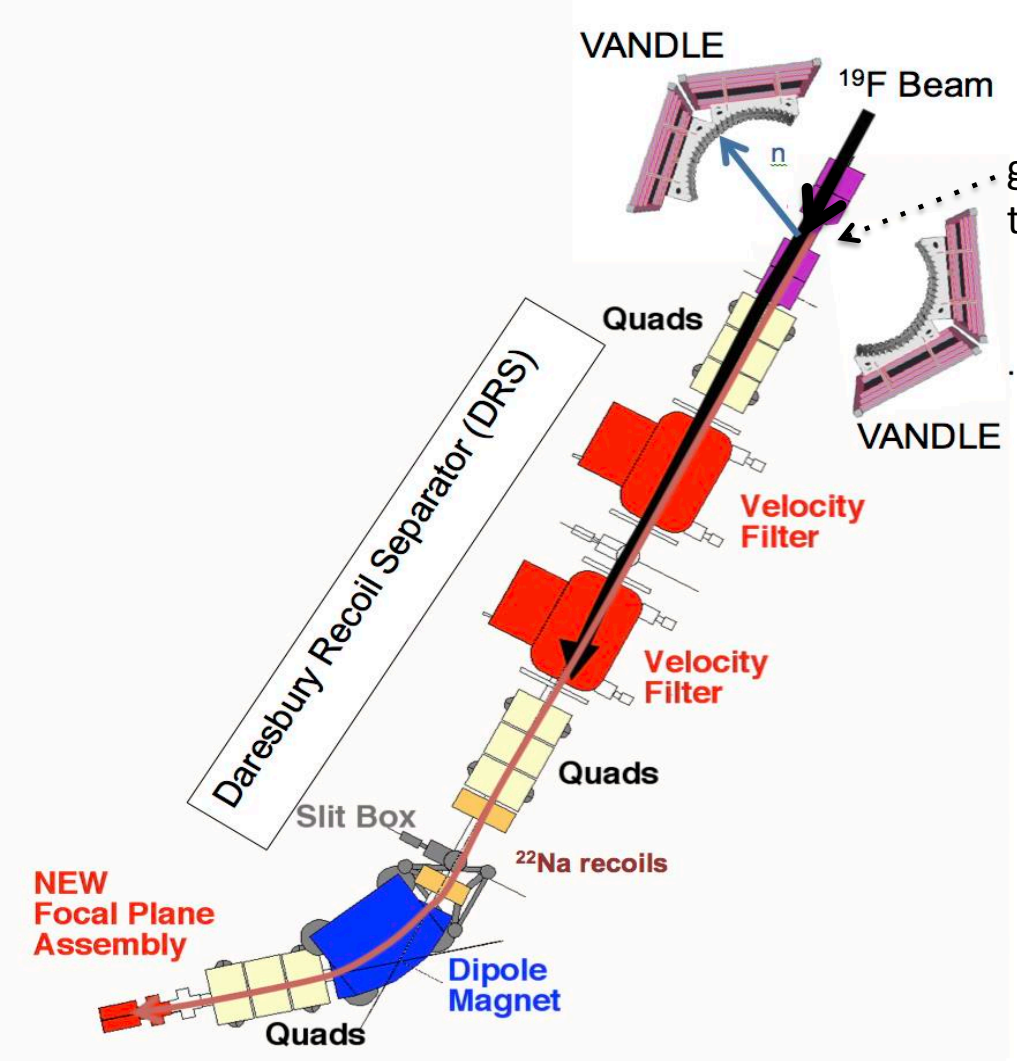

Fig. 2-10. Experimental arrangement for the fluorine-beam experiment showing the VANDLE system to detect neutrons near the gas target system (at top right) and a focal plane detector system to detect the ^{22}Na particles at the end of the Daresbury Recoil Separator (bottom left).

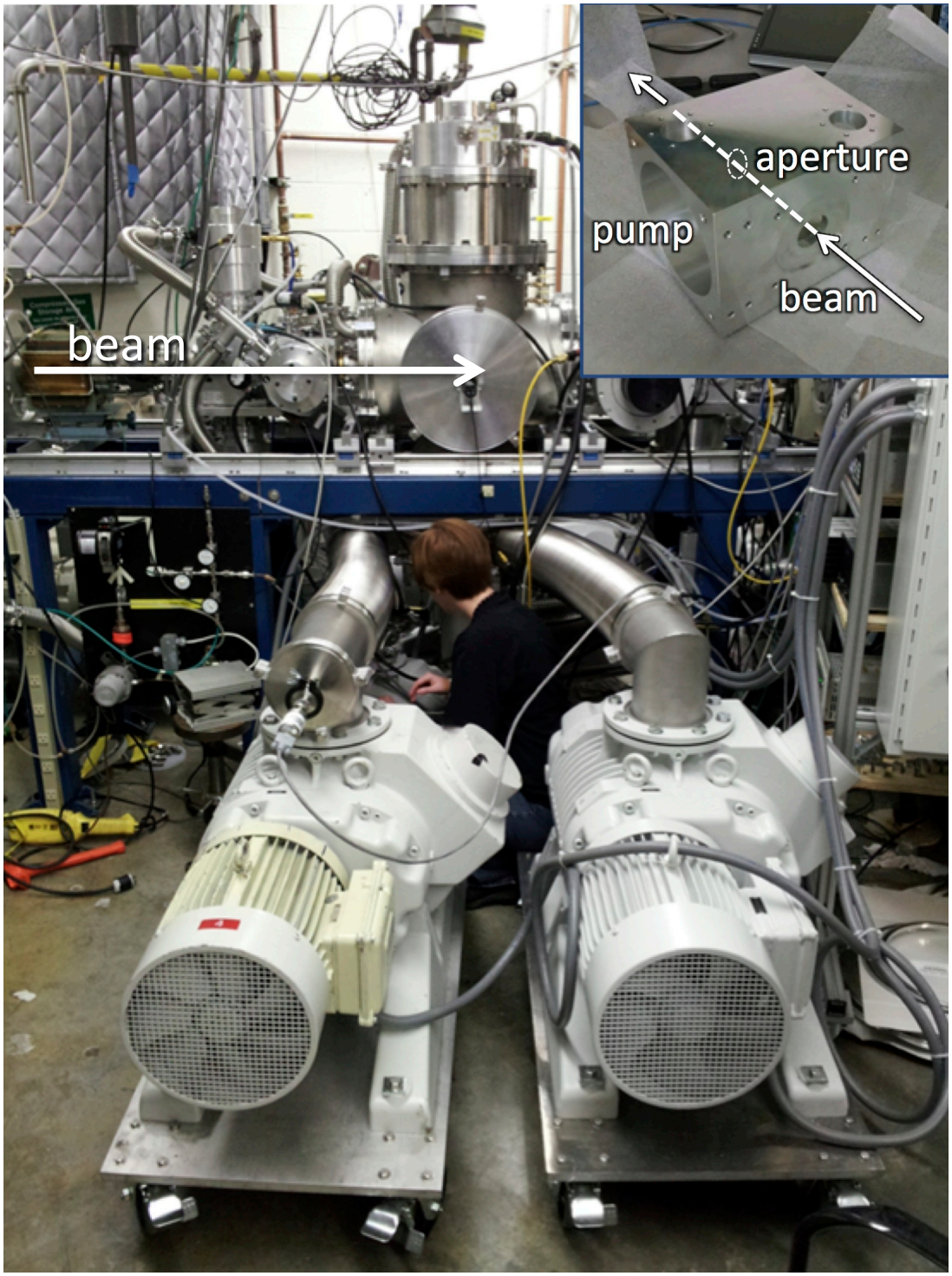

Fig. 2-11. Gas target pumping system from JENSA used for the fluorine-beam experiment [Chi14]. The inset shows one of four differential pumping chambers that that beam travels through and that contains a differential pumping aperture for the windowless target system.

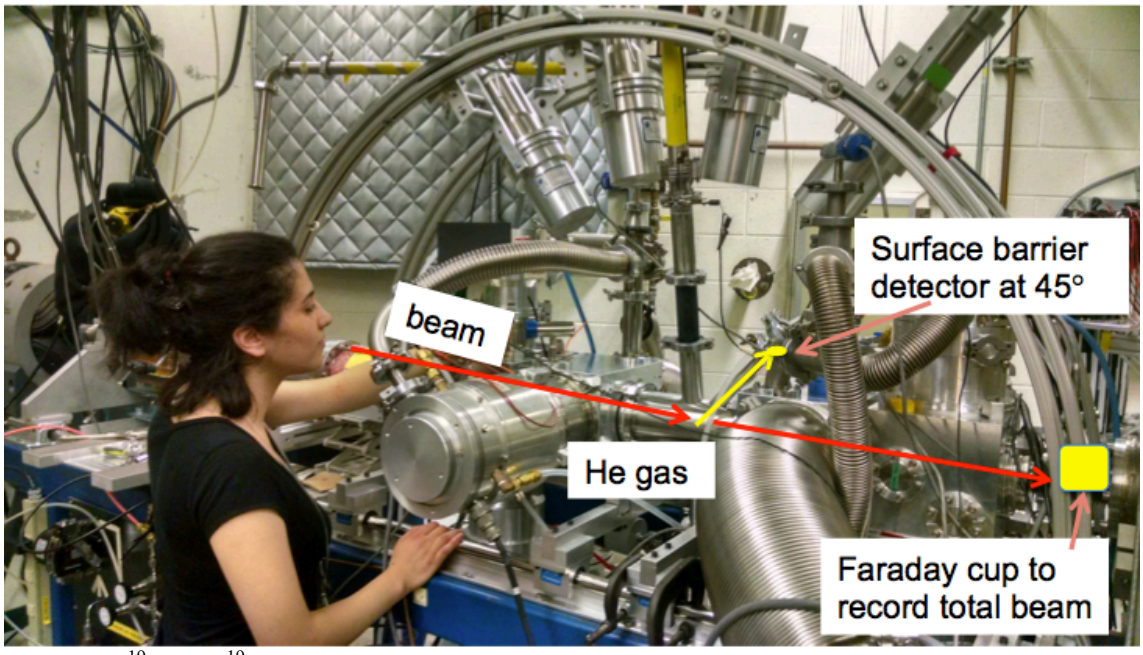

Fig. 2-12. $^{19}F(\alpha,\alpha)^{19}F$ scattering measurement setup at ORNL; alpha particles are scattered out of the gas target by the beam at an upward angle of 45 degrees and into a silicon surface barrier detector.

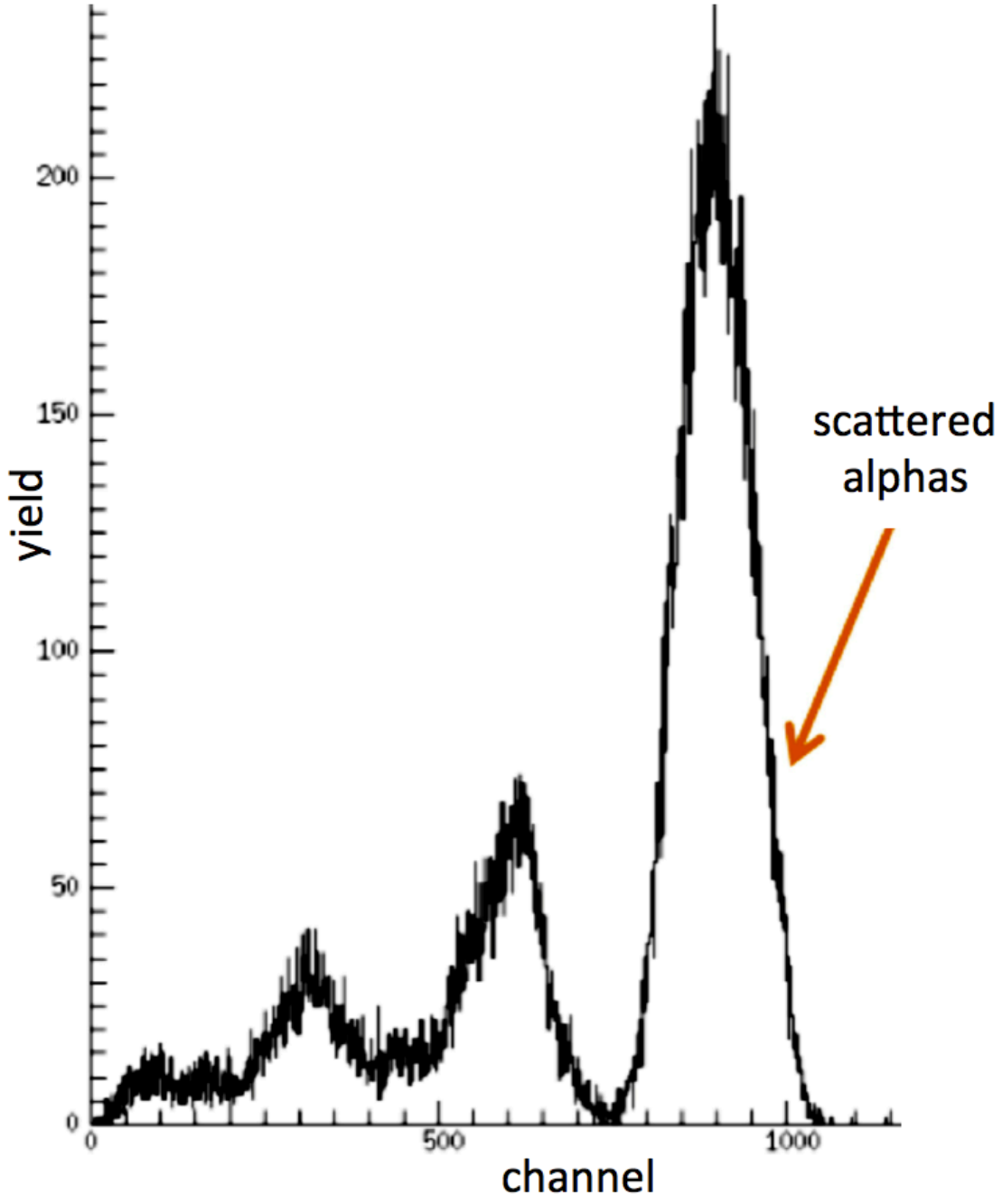

Fig. 2-13. Typical spectrum of our measurement of $^{19}F(\alpha,\alpha)^{19}F$ at one beam energy, with the peak from scattered alphas indicated.

Fig. 2-14. VANDLE detector array setup (beam right, view from side) at ORNL for the fluorine-beam experiment.

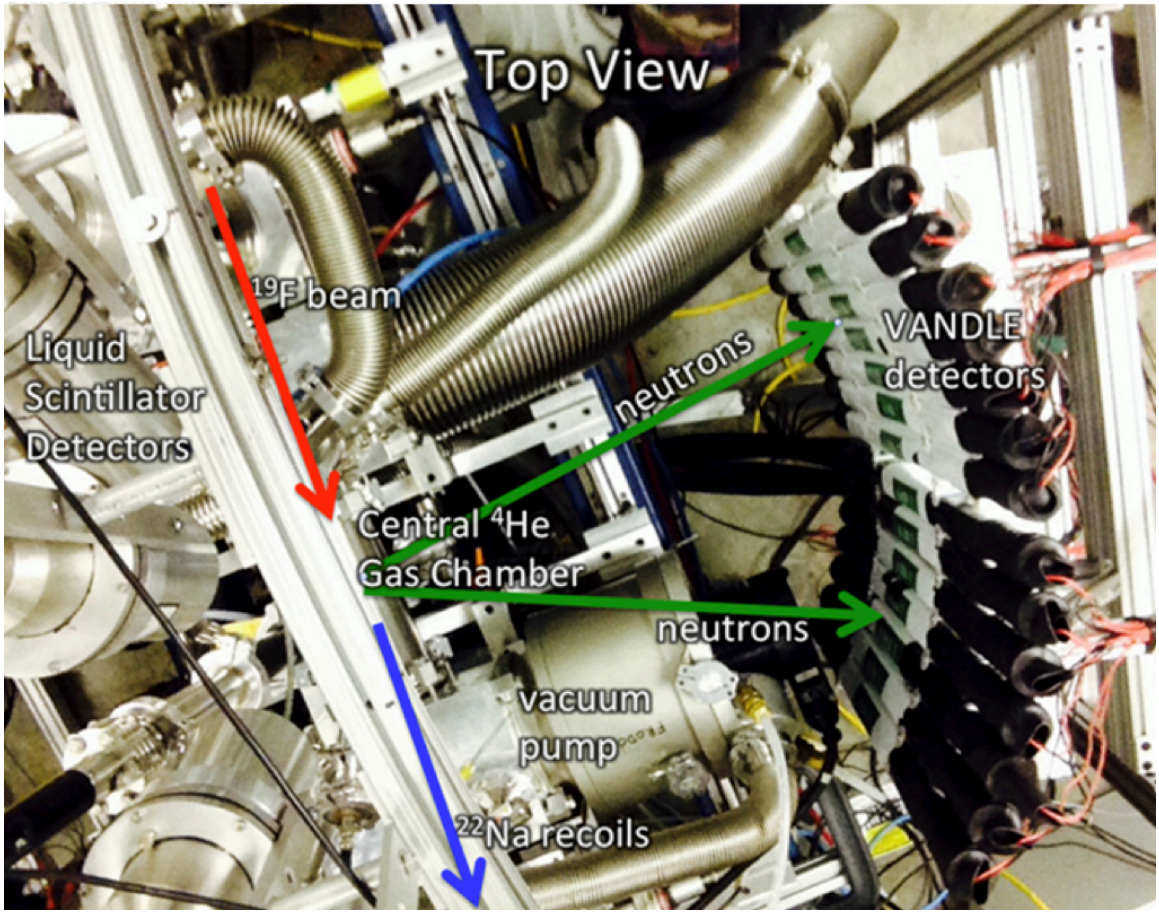

Fig. 2-15. VANDLE detector array setup (view from top) at ORNL for the fluorine-beam experiment.

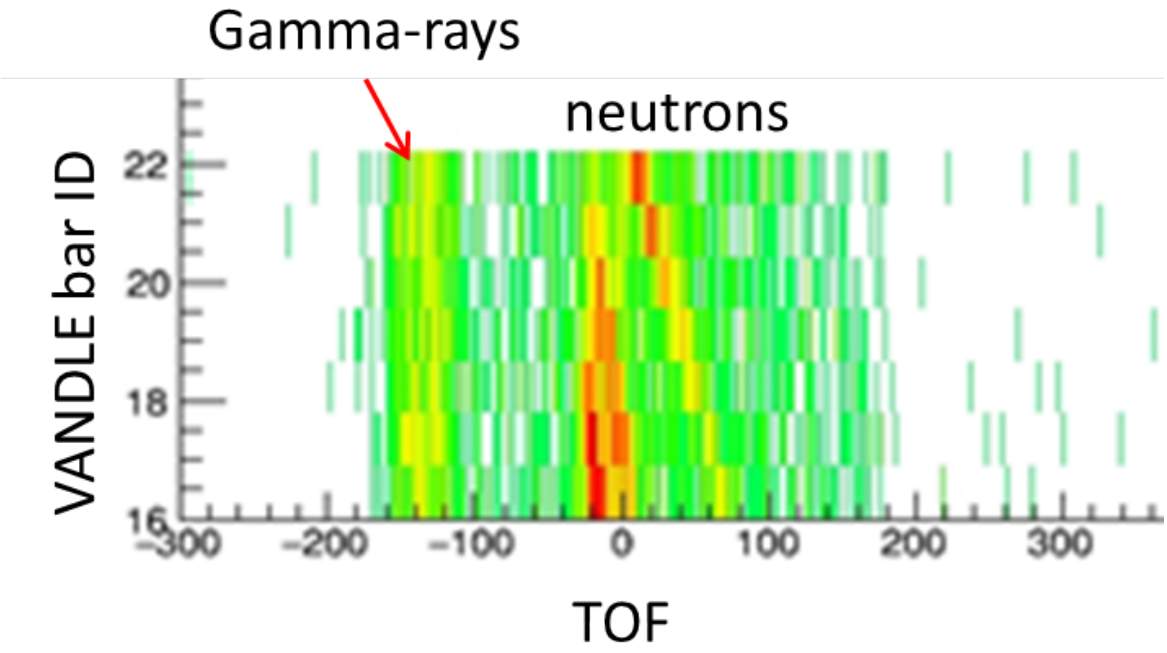

Fig. 2-16. Typical ^{22}Na-gated neutron TOF spectrum from VANDLE in the fluorine-beam experiment. For VANDLE bars 16-22 shown, the gamma-rays from the target are easily separated from the neutrons. The kinematics of the reaction determine the changing neutron energies as a function of angle (bar position).

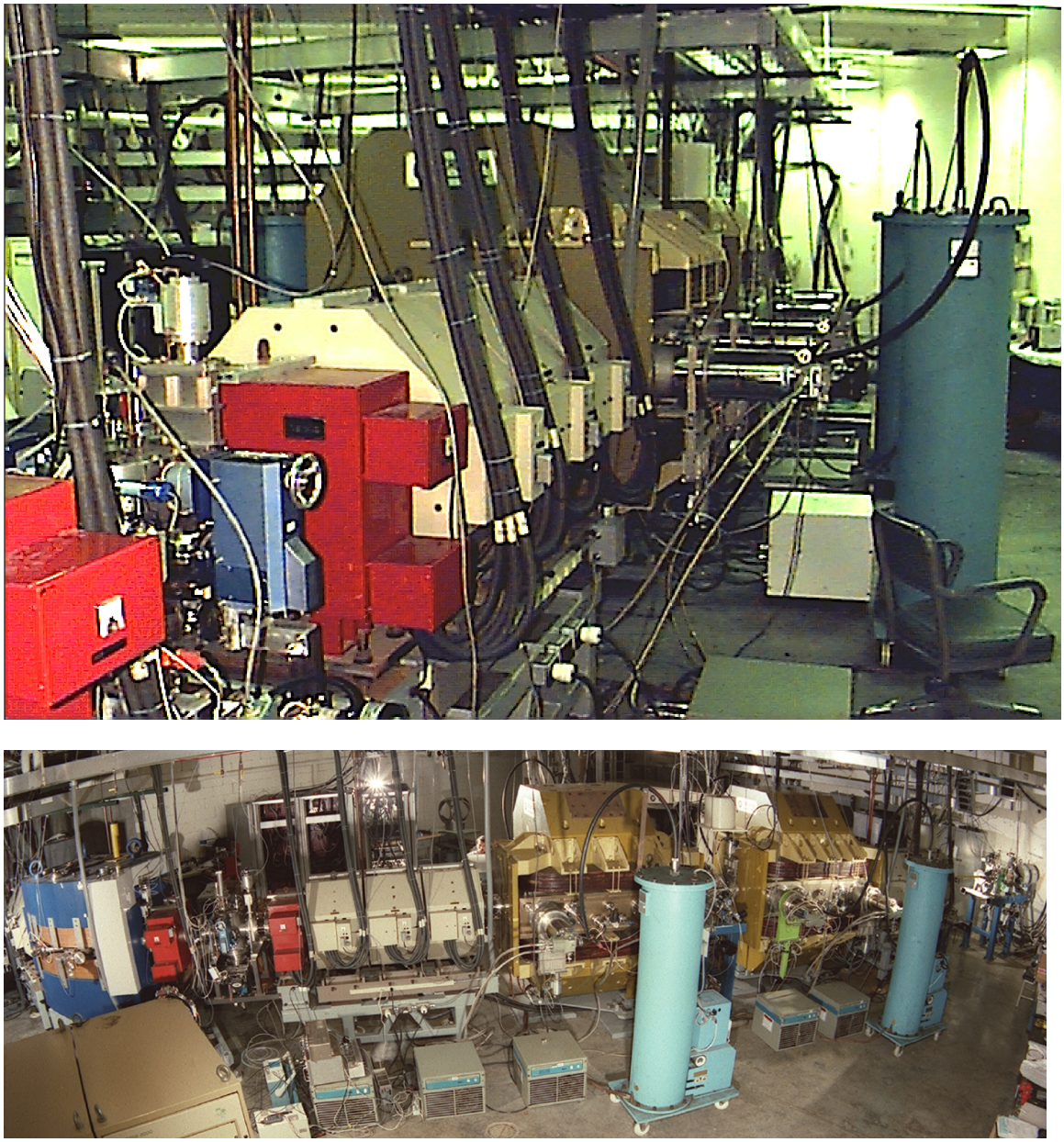

Fig. 2-17. Two views of the Daresbury Recoil Separator (DRS) [Chi09] used to separate the unreacted ^{19}F beam particles from the ^{22}Na reaction products in our measurement of the $^{19}F(\alpha,n)^{22}Na$ reaction with a fluorine beam.

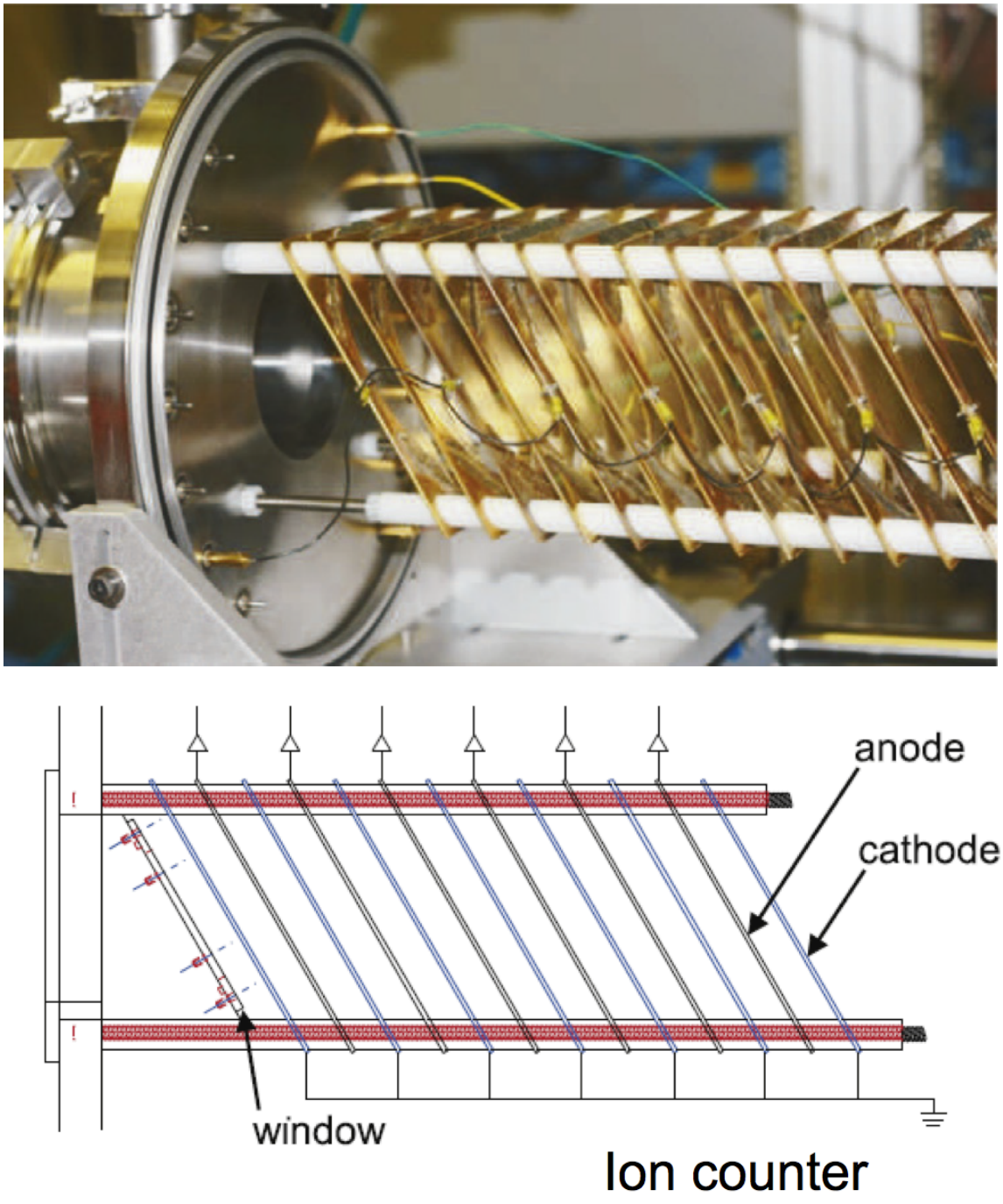

Fig. 2-18. Gas Ionization Counter [Cha14] used for the detection of the ^{22}Na reaction products in our fluorine-beam experiment. Top: photograph of tilted-foil assembly inside the counter, with the outer container removed. Bottom: diagram of counter interior, where the particles enter from the left through the window.

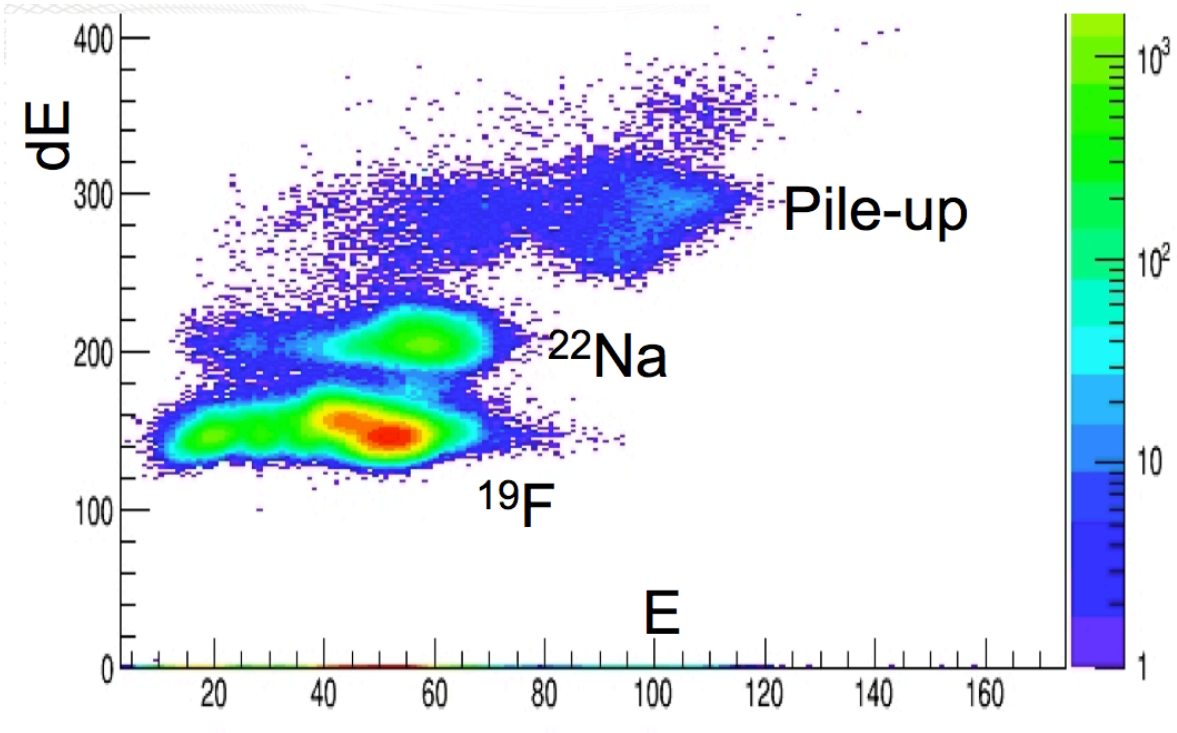

Fig. 2-19. Particle identification spectrum (energy loss vs. total energy) from the gas ionization counter showing ^{22}Na from ^{19}F(α,n)^{22}Na as well as scattered ^{19}F beam particles and their pile-up signals.

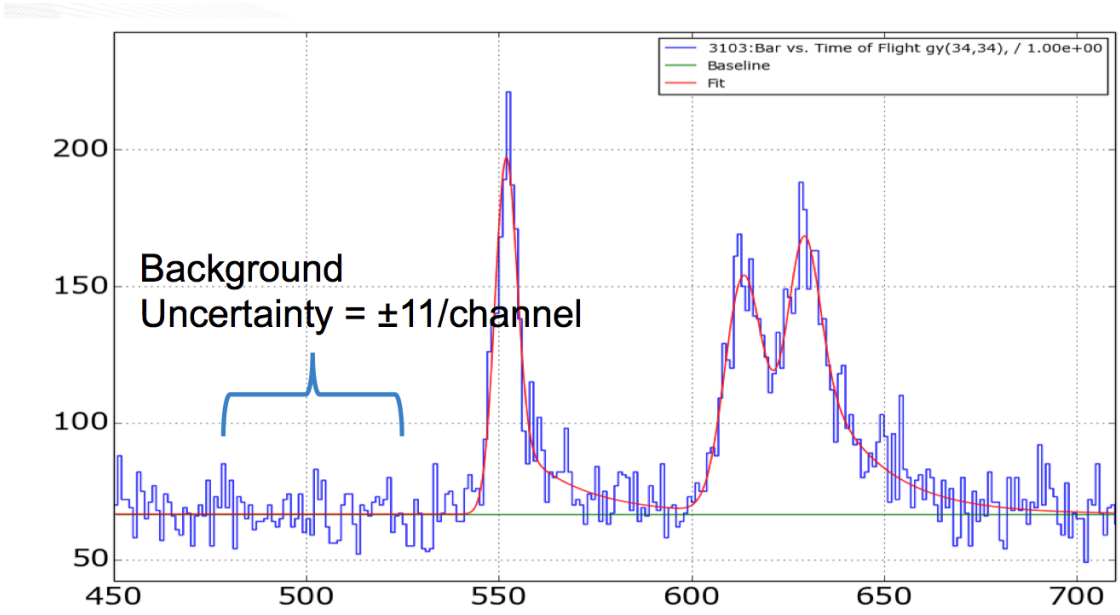

Fig. 3-1. Neutron TOF spectrum in alpha-beam experiment showing uncertainty in background determination of yields.

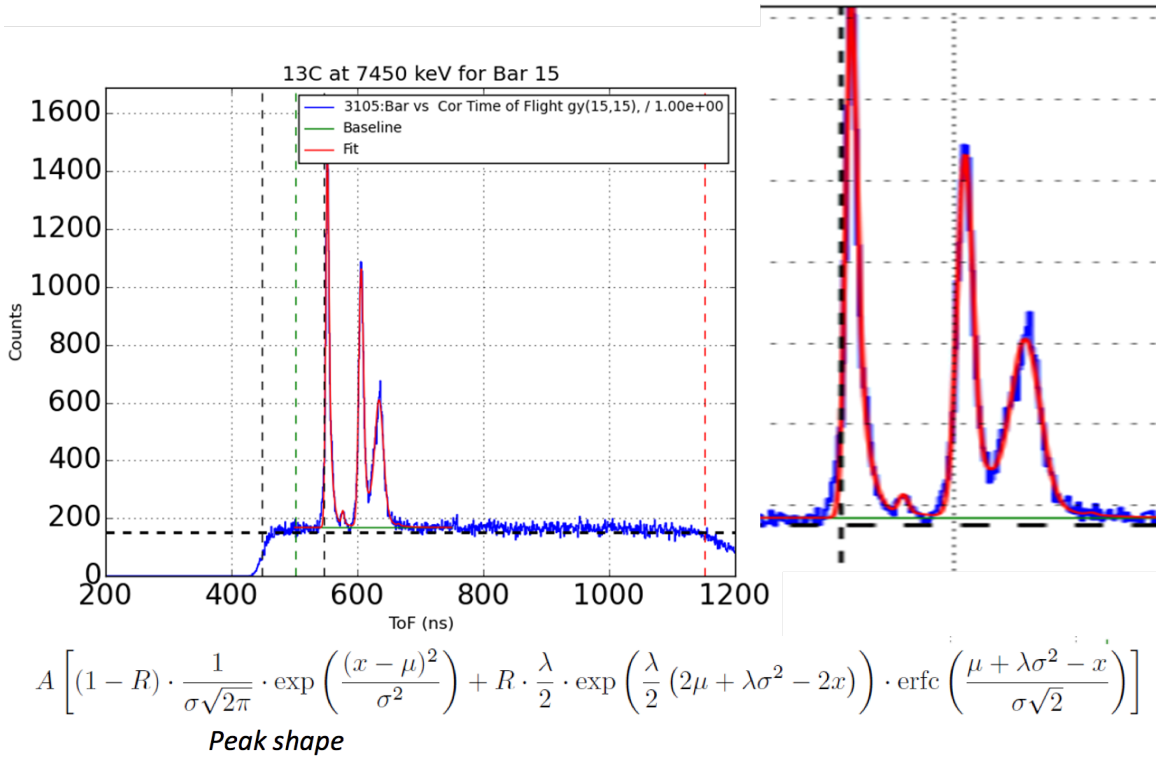

Fig. 3-2. Peak fits to a neutron TOF spectra from our measurement of $^{13}C(\alpha,n)^{16}O$. The full spectrum is shown in the upper left, and an enlargement is shown in the upper right. The sparse level density in ^{16}O provided clean peaks to see the TOF response shape and refine the peak shape formula (listed in the bottom of the figure) that includes a Gaussian with a decaying exponential term. This spectrum was taken with an alpha beam energy of 7.450 MeV. The four peaks are from gamma-rays followed by neutrons populating the ground state and first few excited states in ^{16}O. At this energy, 90% of the reaction yield results from neutrons populating the excited states rather than the ground state.

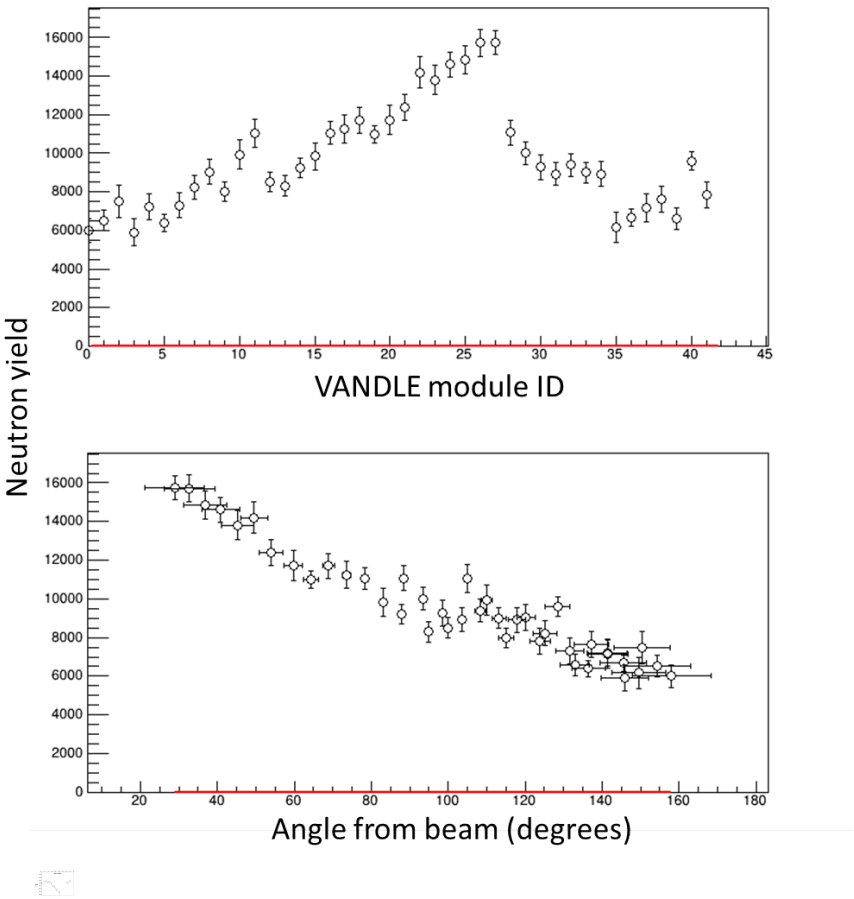

Fig. 3-3. Distribution of neutron yields across the array in alpha-beam experiment. The top plot is the *measured neutron yield vs. bar* for all 42 VANDLE bars (numbered 0-41). The lower plot is the same data displayed as *measured yield vs. angle* distribution The horizontal error bars in the lower panel represents the full angle coverage of the VANDLE bar centered at that position.

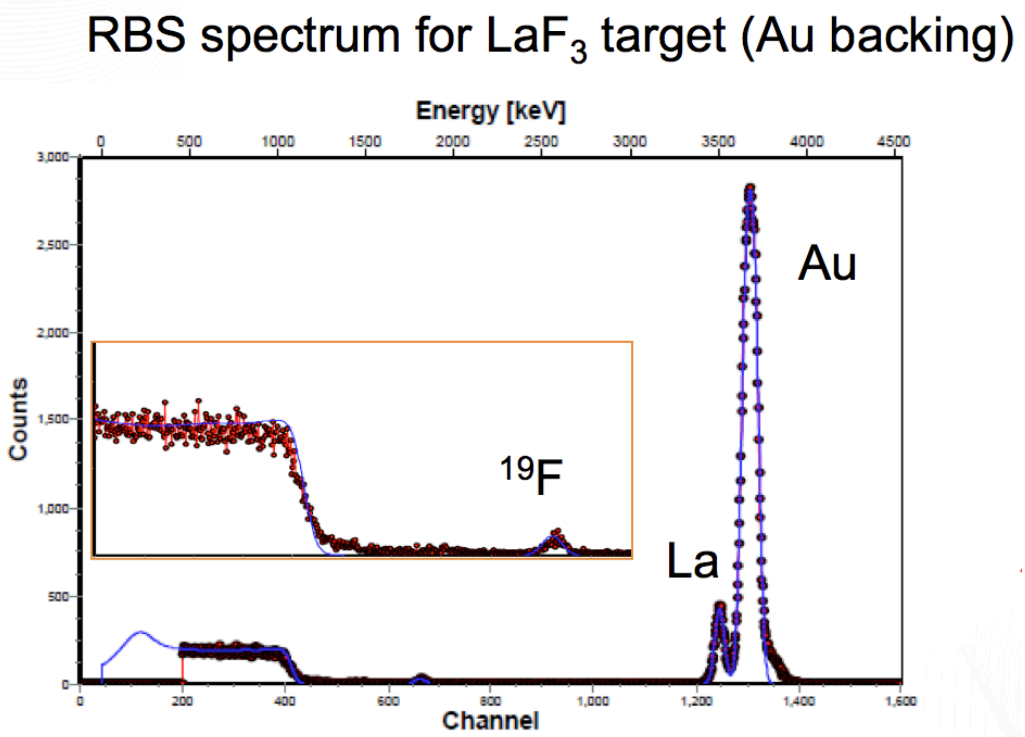

Fig. 3-4. Rutherford backscattering (RBS) spectrum used to determine thickness of LaF_3 targets in alpha-beam experiment.

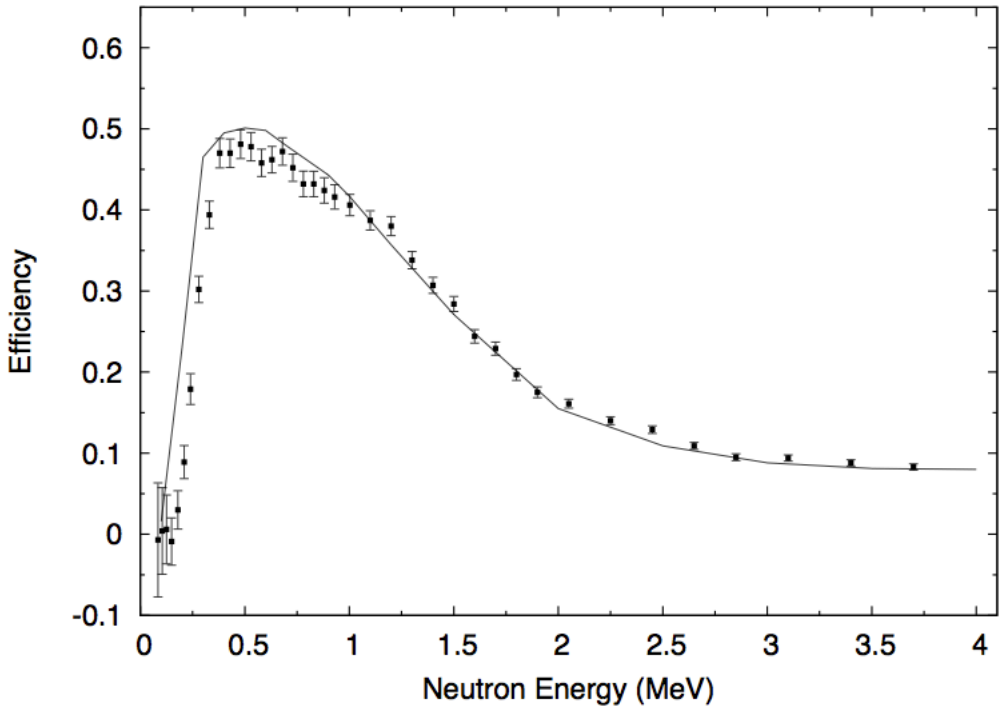

Fig. 3-5. GEANT4 simulation of the response of a VANDLE bar with a threshold of 31 keVee to a ^{252}Cf neutron source (solid line) and corresponding measurements (data points) [Pet16].

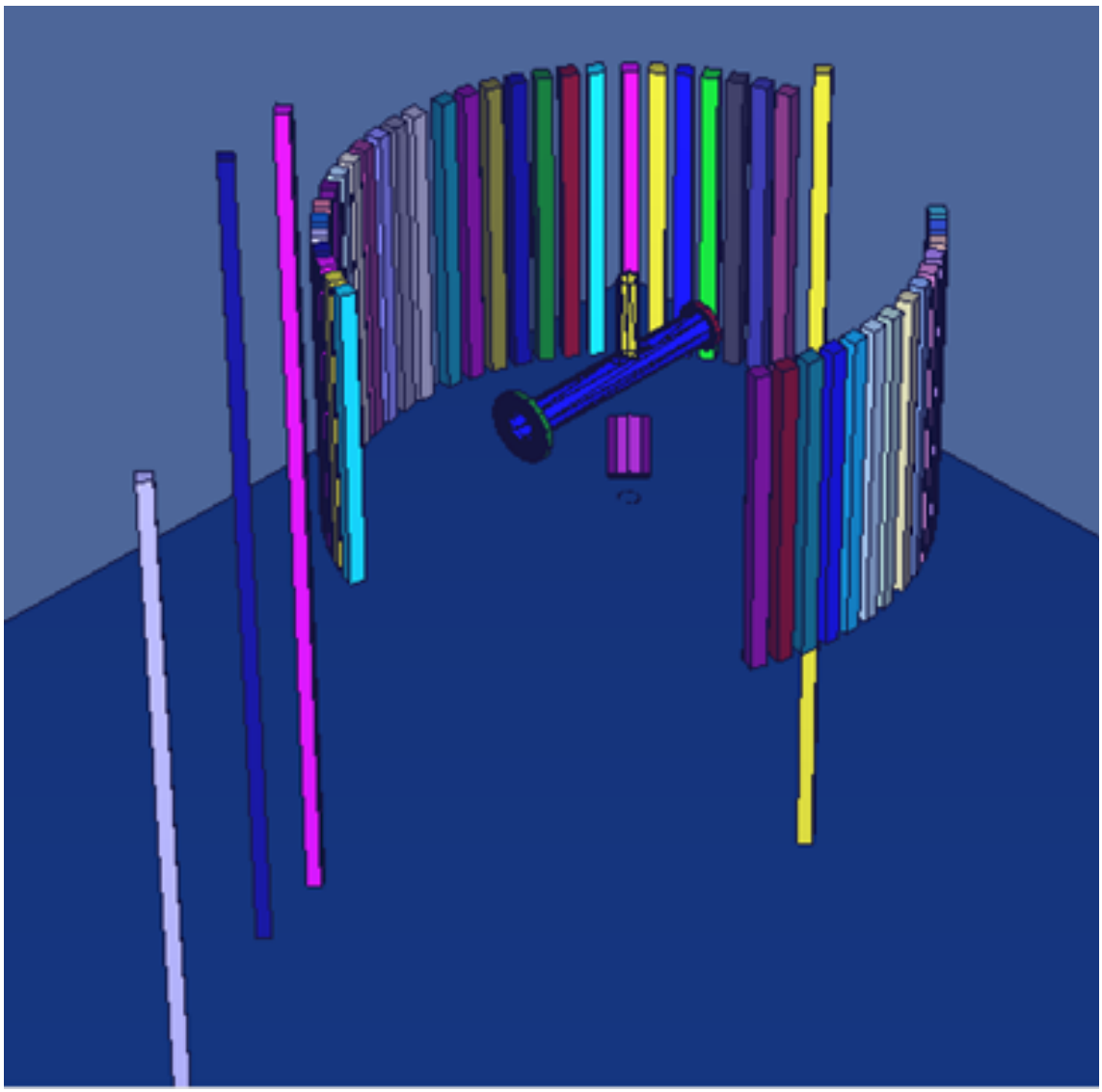

Fig. 3-6. VANDLE detector geometry input for MCNP6 simulations of the *predicted yield vs. angle* distribution in the alpha-beam experiment.

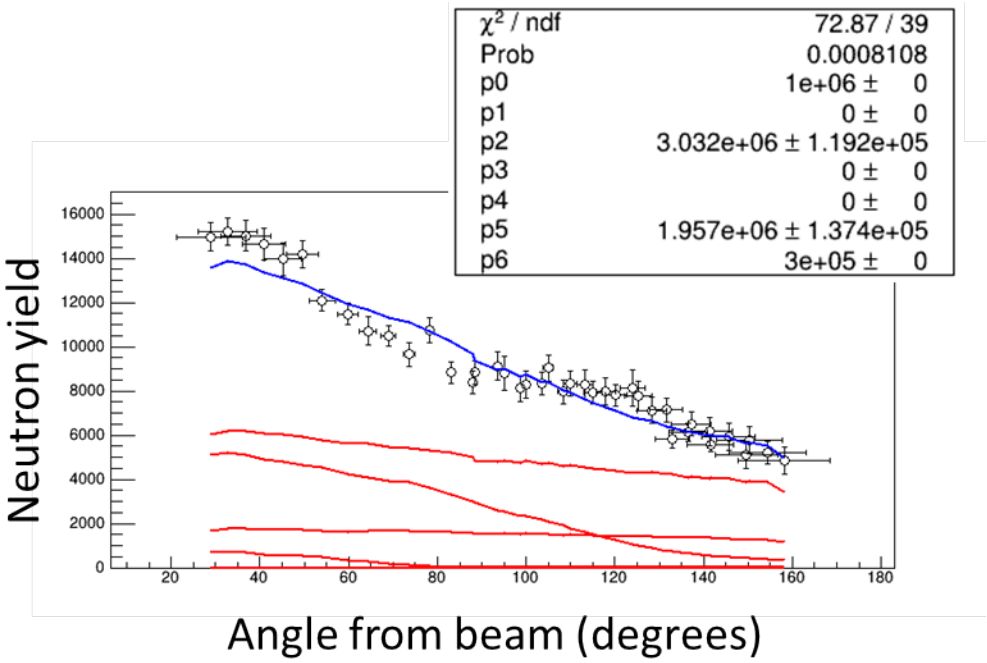

Fig. 3-7. *Measured yield vs. angle* distribution at one energy (data points) and corresponding MCNP6 simulation of *predicted yield per level vs. angle* distributions (red curves) and *predicted total yield vs. angle* distribution (blue curve). The inset shows the fitted variables for each partial cross section. Constraints on the relative weights for these variables are determined by analyzing the TOF spectra.

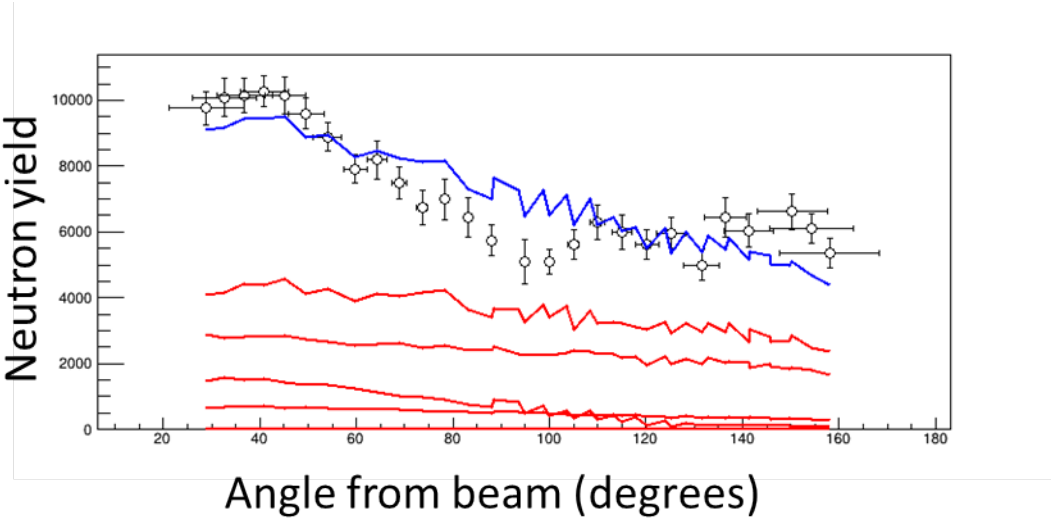

Fig. 3-8. *Measured yield vs. angle* distribution (data points) shown with a GEANT4 simulation of the *predicted yield per level vs. angle* distribution (red curves) and *total yield vs. angle* distribution (blue curve).

```
The Correlation Matrix:
 1.000000e+00, -2.759033e-03, -1.394626e-03, -8.203520e-01,
-2.759033e-03,  1.000000e+00,  1.669761e-09, -5.304310e-04,
-1.394626e-03,  1.669761e-09,  1.000000e+00, -5.189754e-04,
-8.203520e-01, -5.304310e-04, -5.189754e-04,  1.000000e+00,
```

Fig. 3-9. Correlation matrix from the fit of the *measured yield vs. angle* distribution with an MCNP6 simulation with four fit variables corresponding to the partial cross sections to the ^{22}Na ground state and first 3 excited states. The constraint on the sum of the contributions from different levels results in substantial off-diagonal elements. Thus, the error of the total is not necessarily equal to the sum of the errors for all the variables.

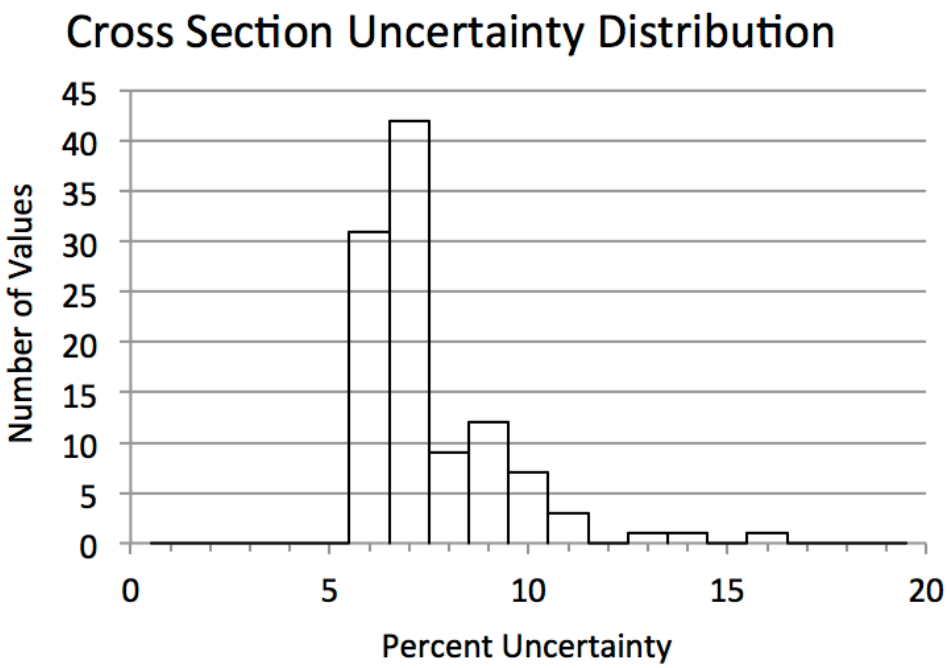

Fig. 3-10. Distribution of uncertainties in the alpha-beam experiment; the average of the distribution is 7.55%.

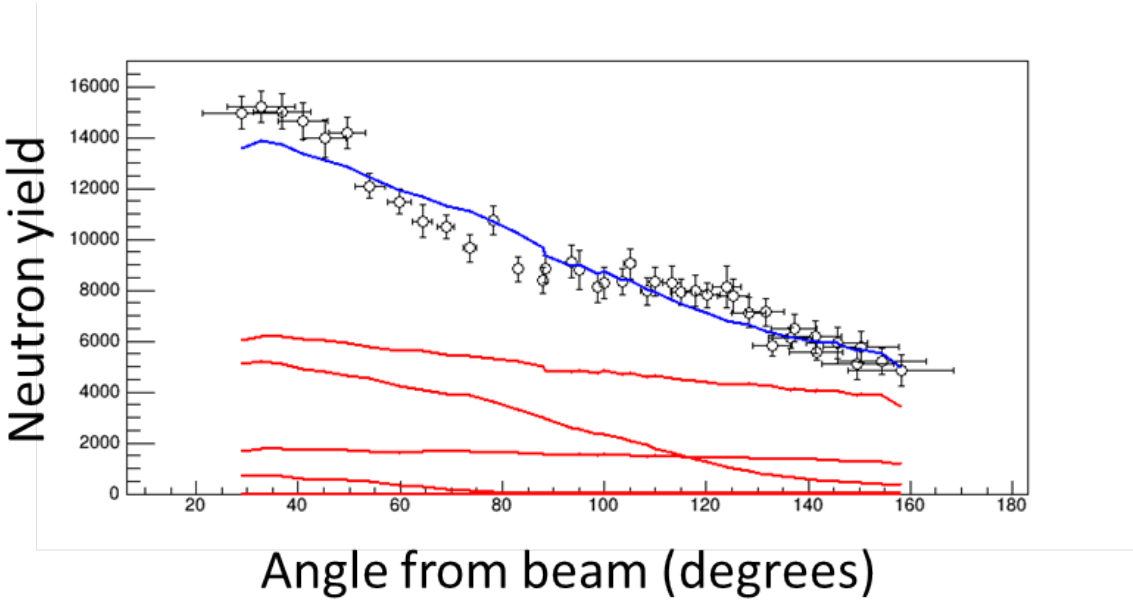

Fig. 3-11. Similar to Fig. 3-7. Illustrating that predicted contributions of different ^{22}Na levels (red curves) to the total predicted yield (blue curve) have similar angular distributions across the VANDLE array. Different weighted sums of these distributions (corresponding to different sets of partial cross sections) can, in some cases, lead to fits of equal quality (reduced chi-squared) but different total cross sections. In other cases, the partial cross sections differ from fits of equal quality but the total cross sections values agree within fit uncertainties.

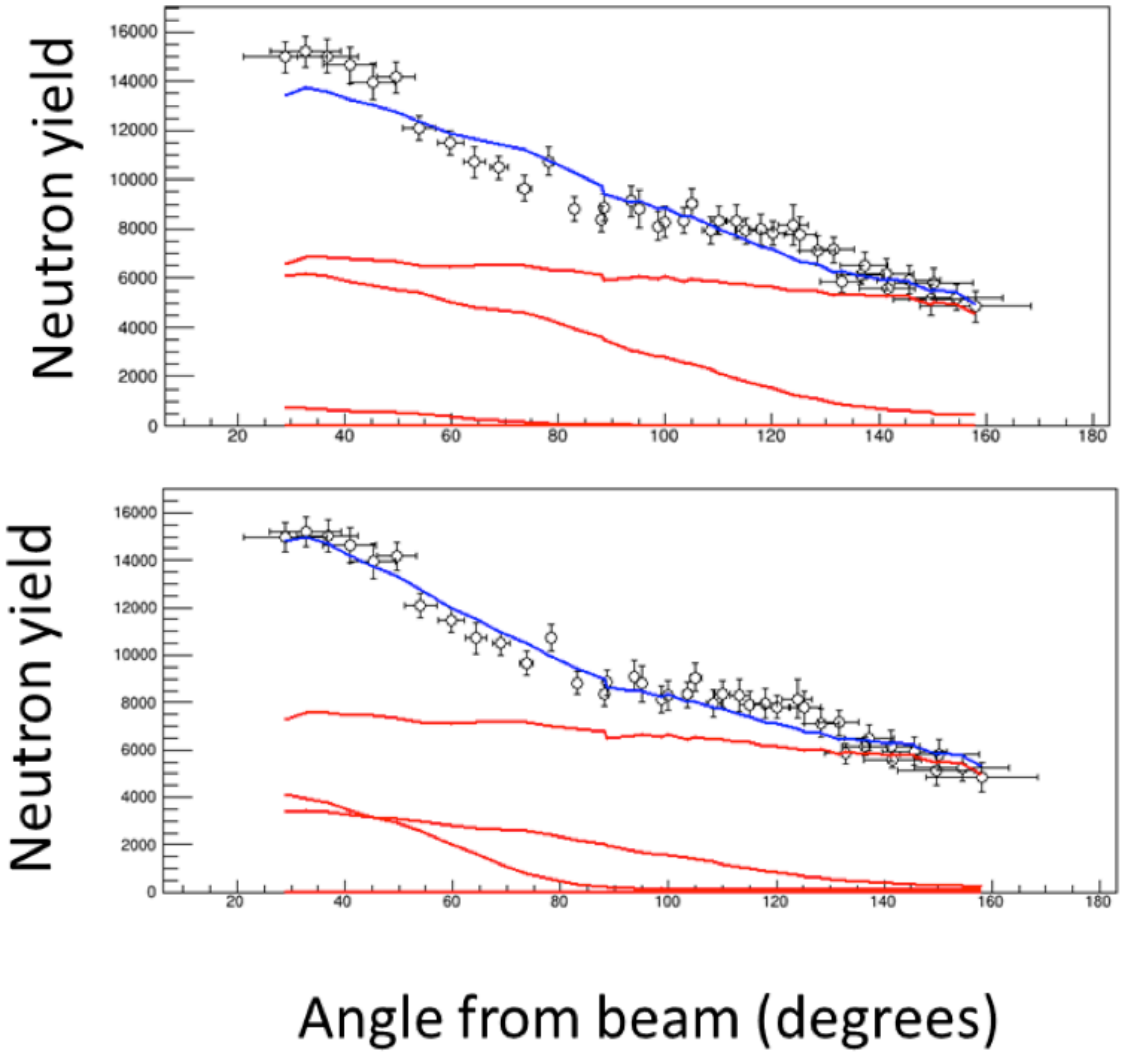

Fig. 3-12. Comparison of two different fits of the MCNP6 simulation of *predicted yield vs. angle* distribution (blue curve) to the same *measured yield vs. angle* distribution (data points) at one energy in the alpha-beam experiment. Red curves show the corresponding simulations of *predicted yield per level vs. angle* distributions. The top plot has nearly equal weights to both the ground state and a mid-level state in ^{22}Na, while the bottom plot has nearly equal weight to the highest energy level and the medium-energy level. By analyzing the TOF spectrum and recording the relative intensities to these levels, we constrain the weights – the fit parameters – to reflect the true partial cross sections. In this case, the two different fits of the simulation to the data result in different total cross section values.

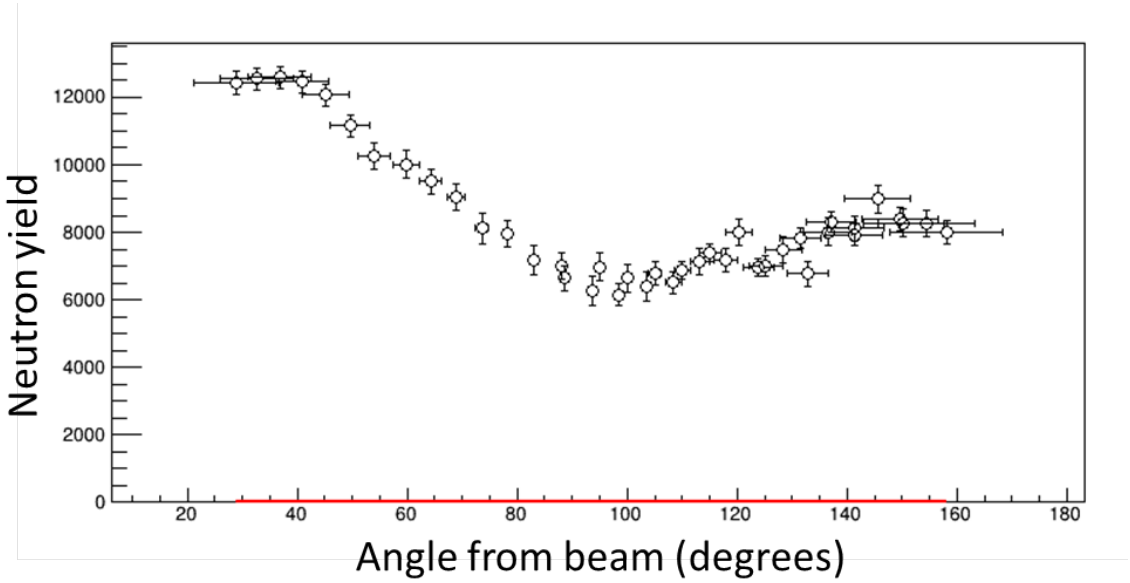

Fig. 3-13. Similar to Fig. 3-3 but for an energy where the angular distribution of yields across the array is clearly non-isotropic. In this and other spectra, a clear dipole distribution is evident. Most anisotropies, however, are due to populating highly excited levels in ^{22}Na that are forward focused because the backward neutrons are below threshold.

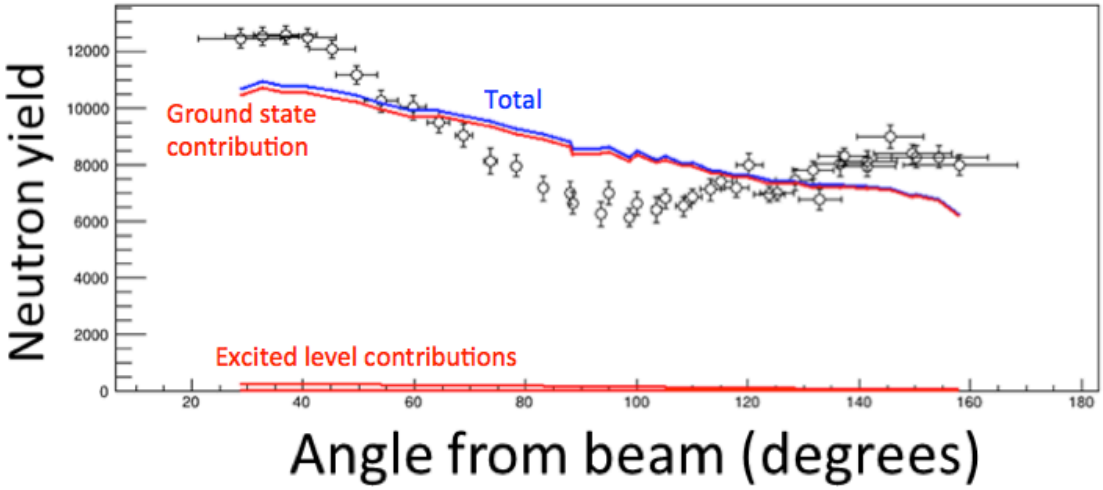

Fig. 3-14. Same data as Fig 3-13. The fit of the MCNP simulation to the spectrum shown in Fig. 3-13 illustrates the limitation of our analysis approach at energies where there is a non-isotropic angular distribution of yields across the array. At this energy, nearly all the intensity comes from populating the ground state in ^{22}Na. The overall intensity is fit well, even if the shape is not. The fit uncertainty for cases like this where there is a dipole distribution is typically larger due to the poor fit to the data.

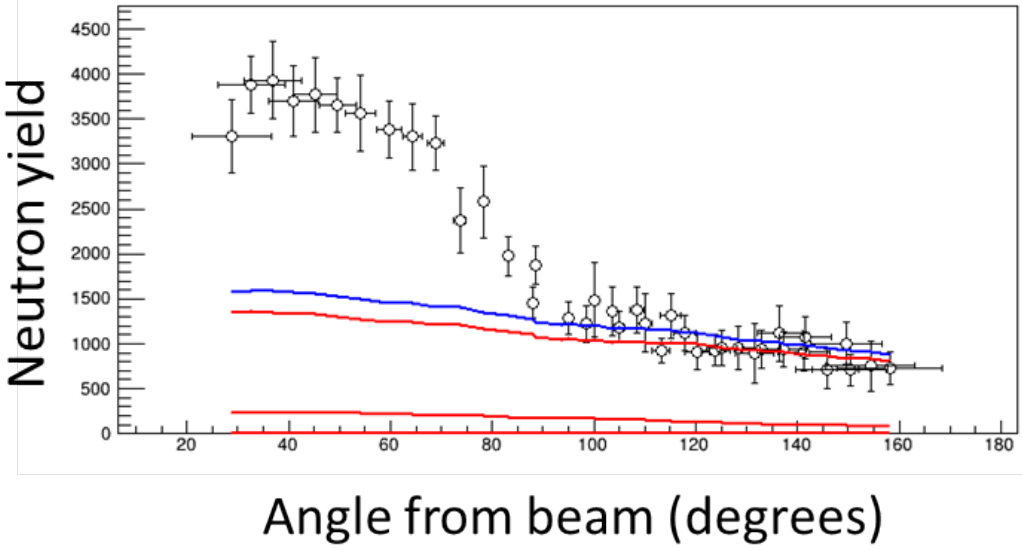

Fig. 3-15. Example of a *measured yield vs. angle* distribution that exhibits strong yields at forward angles in the lab frame. In these cases the forward focus of the distribution is not due populating a highly excited state, but due to strong anisotropy of a reaction to a low ^{22}Na energy level. Two fits were done for such runs, one for the smooth portion of the distribution (displayed here) and another to account for the extra intensity in the forward peak; these fits were appropriately scaled and added to determine the total cross section.

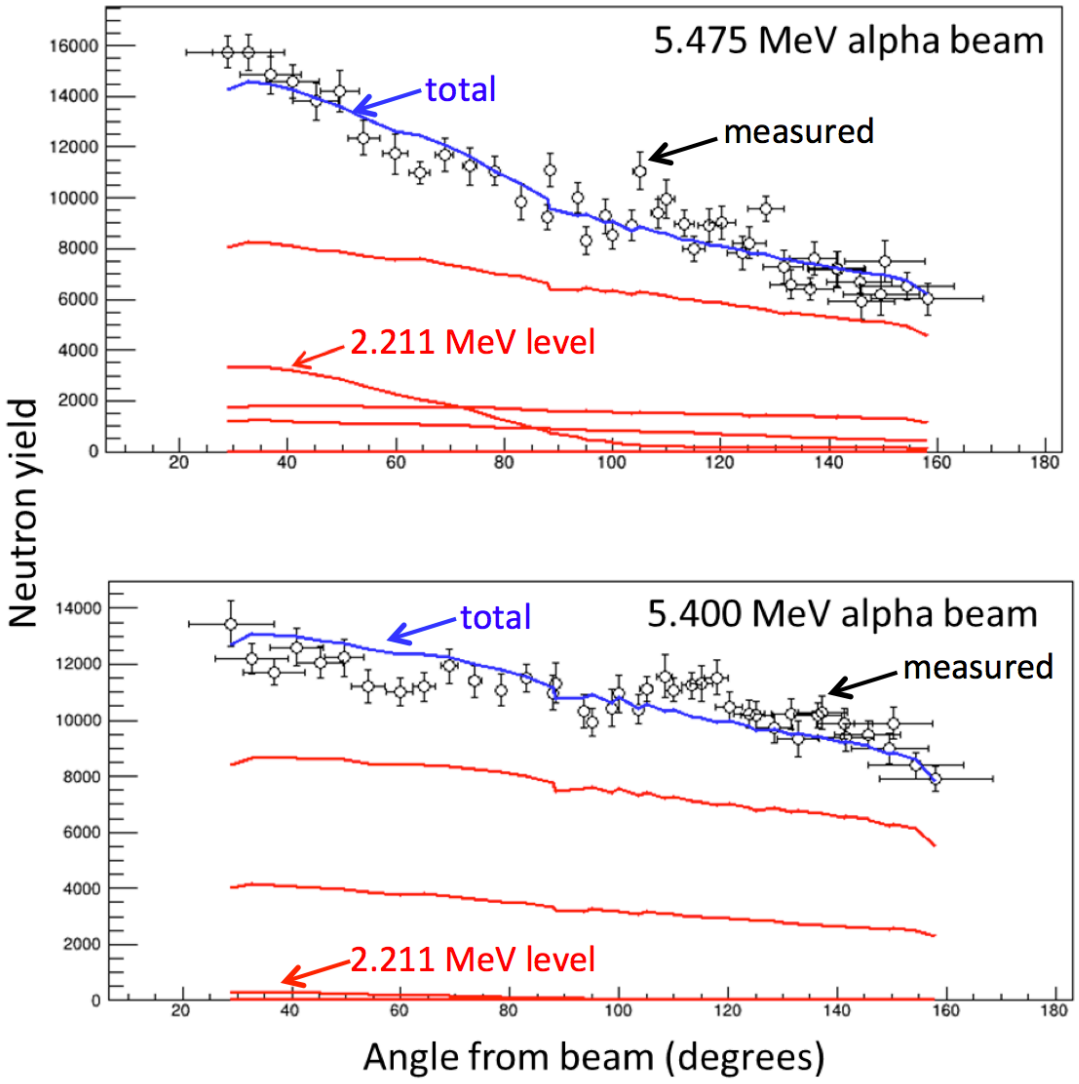

Fig. 3-16. Bottom: predicted yield for neutrons from reactions to the 2.211 MeV ^{22}Na excited state (labeled red curve) are too low in energy to be above detector threshold and contribute to the predicted total yield (blue curve). In such cases where these neutrons will contribute to the total neutron yield, we constrained the respective partial cross section by examining the uncalibrated TOF spectra which has a much lower detection threshold. Top: at a beam energy that is three steps (75 keV) higher, neutrons from reactions to the 2.211 MeV ^{22}Na excited state are above the detection threshold at forward angles.

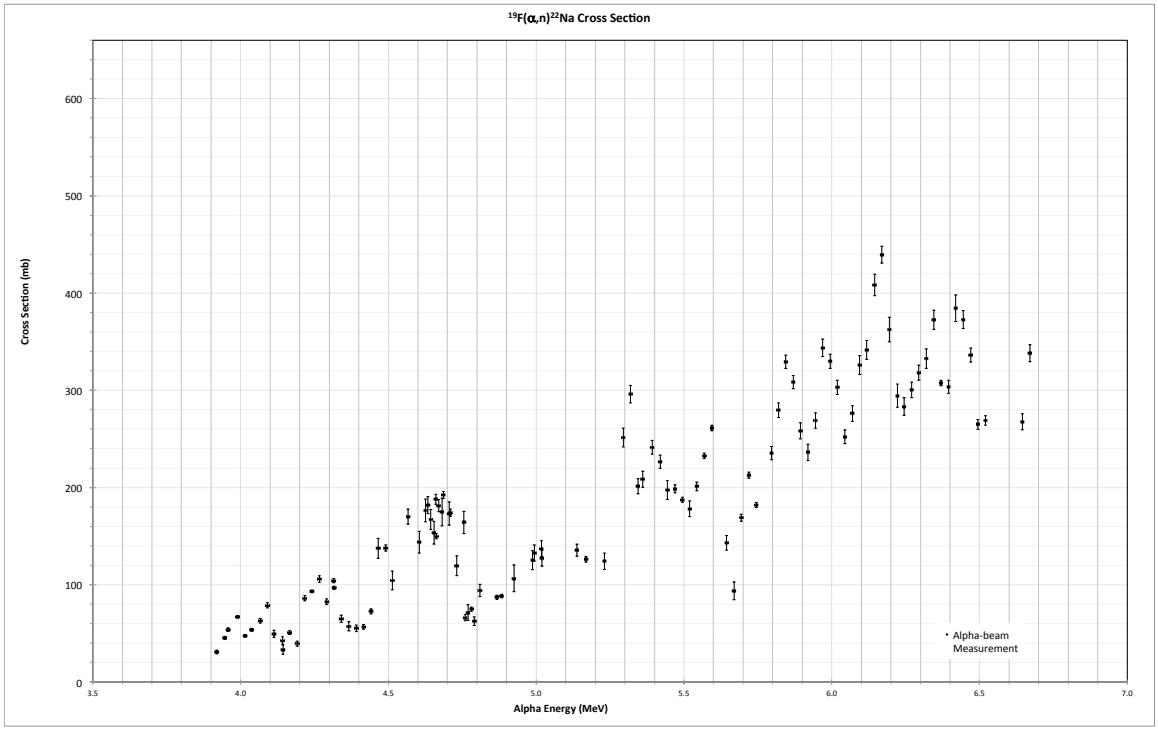

Fig. 3-17. Cross section values from the alpha-beam experiment shown with fit uncertainties but without systematic uncertainties.

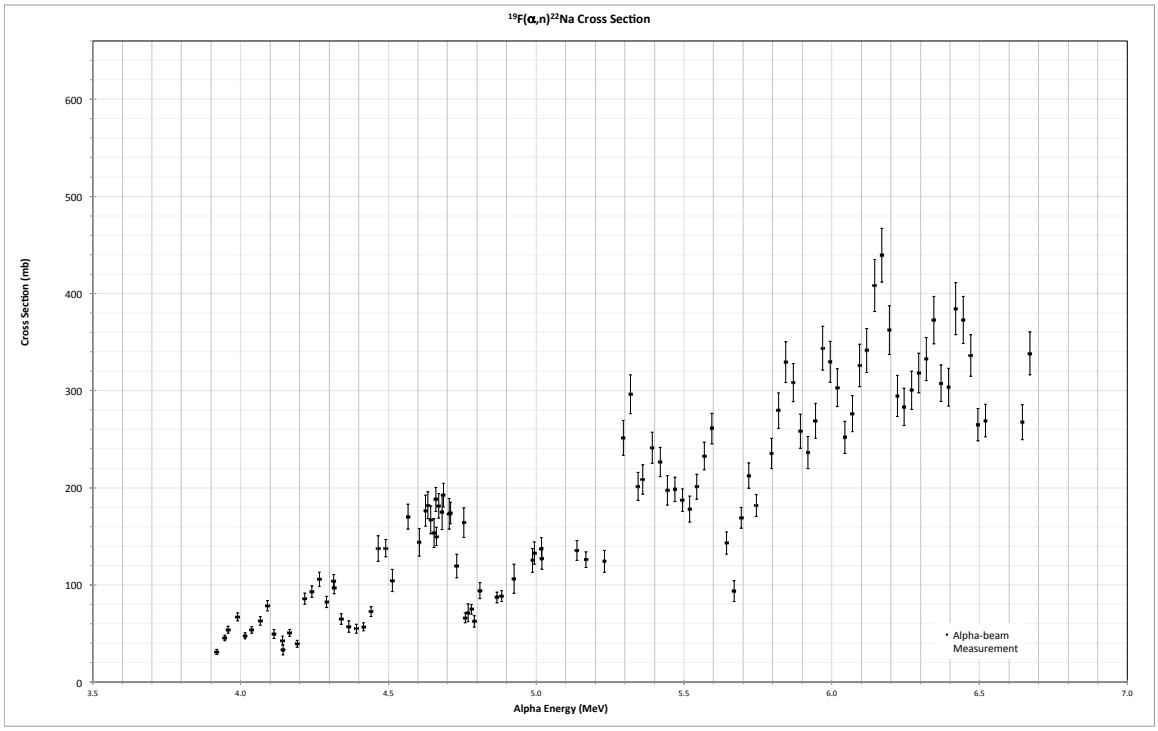

Fig. 3-18. Cross section vs. energy for the alpha-beam experiment including all uncertainties.

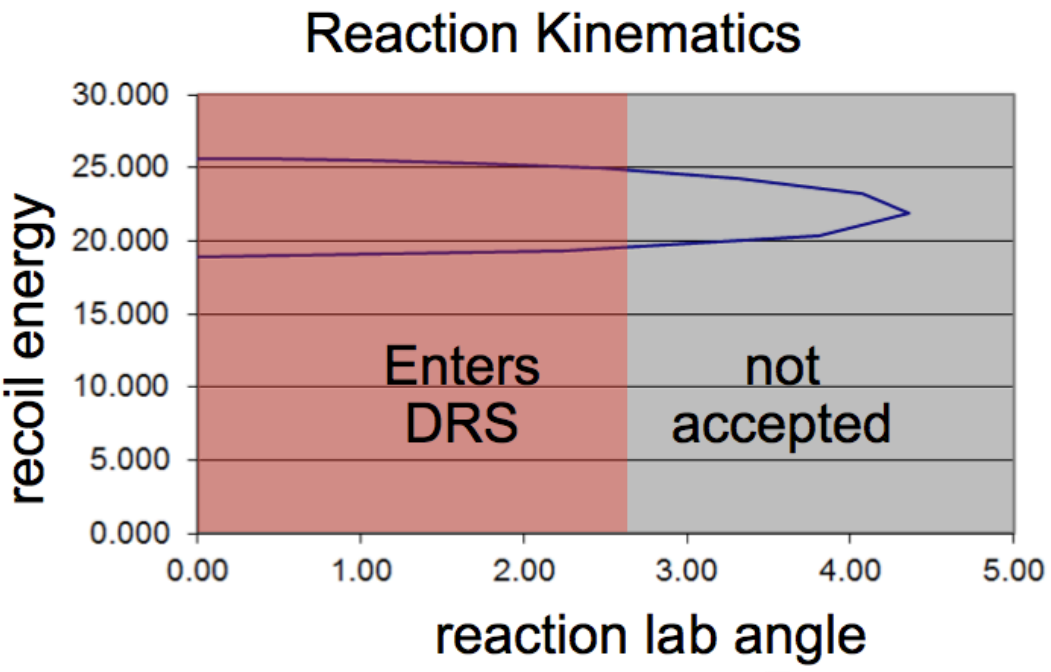

Fig. 3-19. Variation of ^{22}Na recoil energy with angle in laboratory frame, shown with acceptance of the DRS for the fluorine-beam experiment. Events with angles greater than 2.6 degrees will not be transmitted through the DRS to the focal plane for counting.

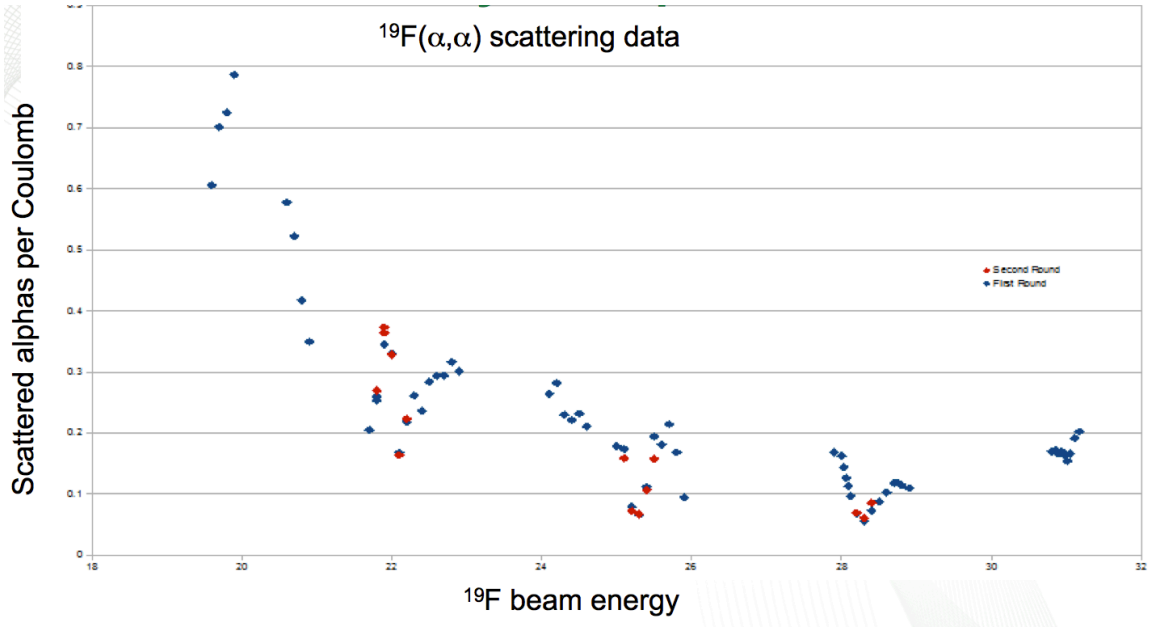

Fig. 3-20. Excitation function of our ^{19}F(α,α)^{19}F measurement, used for normalization of the fluorine-beam experiment. The blue and red data points show our first and second set of measurements, respectively, that we made to check reproducibility.

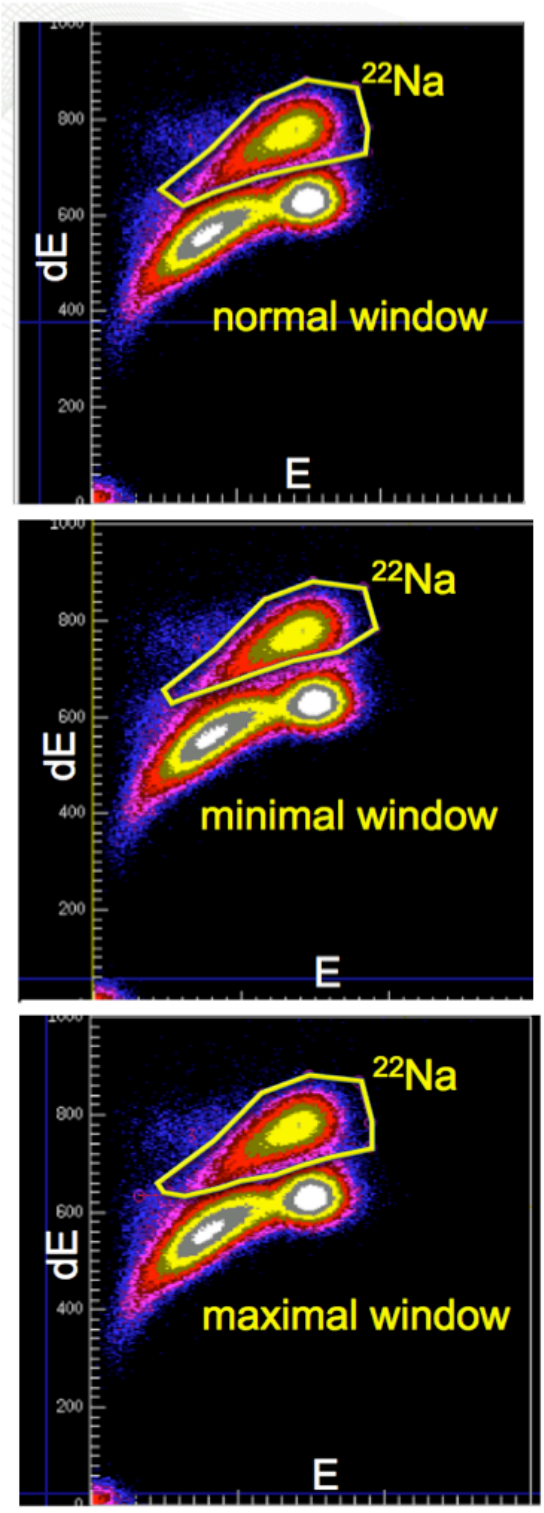

Fig. 3-21. Identification of ^{22}Na ions in the gas ionization counter at DRS focal plane by plotting energy loss dE versus total energy E. A normal two-dimensional gate ("window") is shown at top, along with a minimal and a maximal window shown in the middle and bottom, respectively, to determine the uncertainty in the ^{22}Na yields.

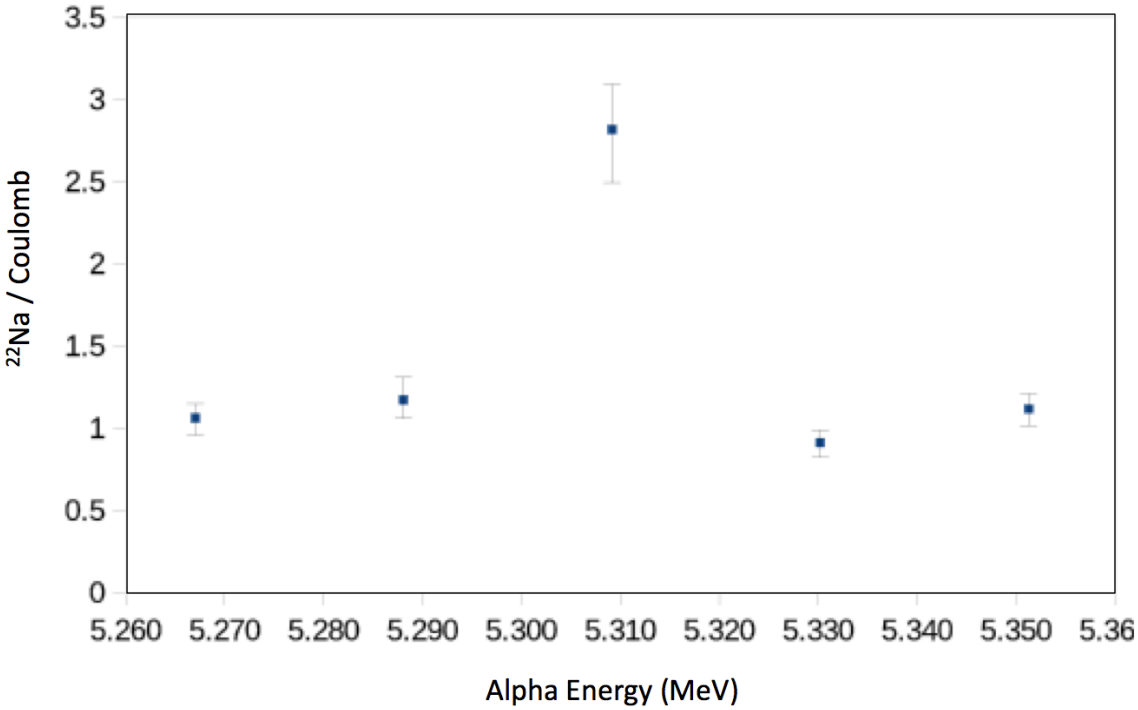

Fig. 3-22. ^{22}Na yield per Coulomb as function of energy at energies near 5.300 MeV as measured at DRS focal plane in the gas ionization counter.

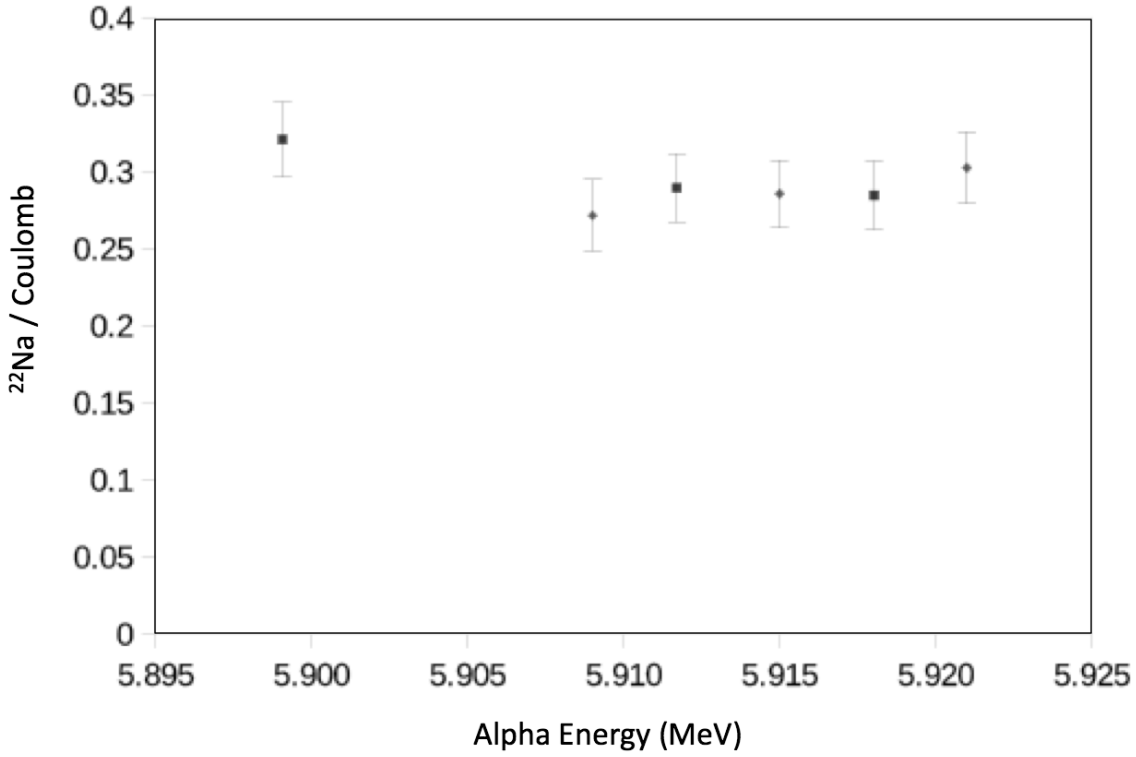

Fig. 3-23. ^{22}Na yield per Coulomb as function of energy at energies near 5.910 MeV as measured at DRS focal plane in the gas ionization counter.

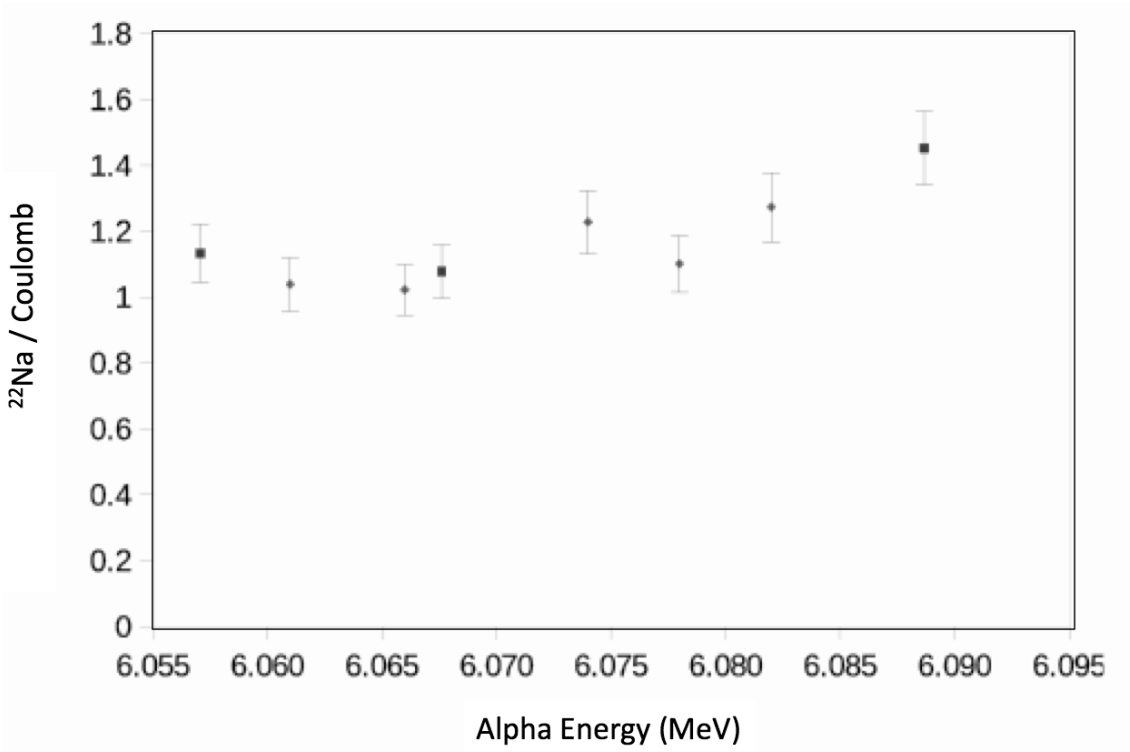

Fig. 3-24. ^{22}Na yield per Coulomb as function of energy at energies near 6.075 MeV as measured at DRS focal plane in the gas ionization counter.

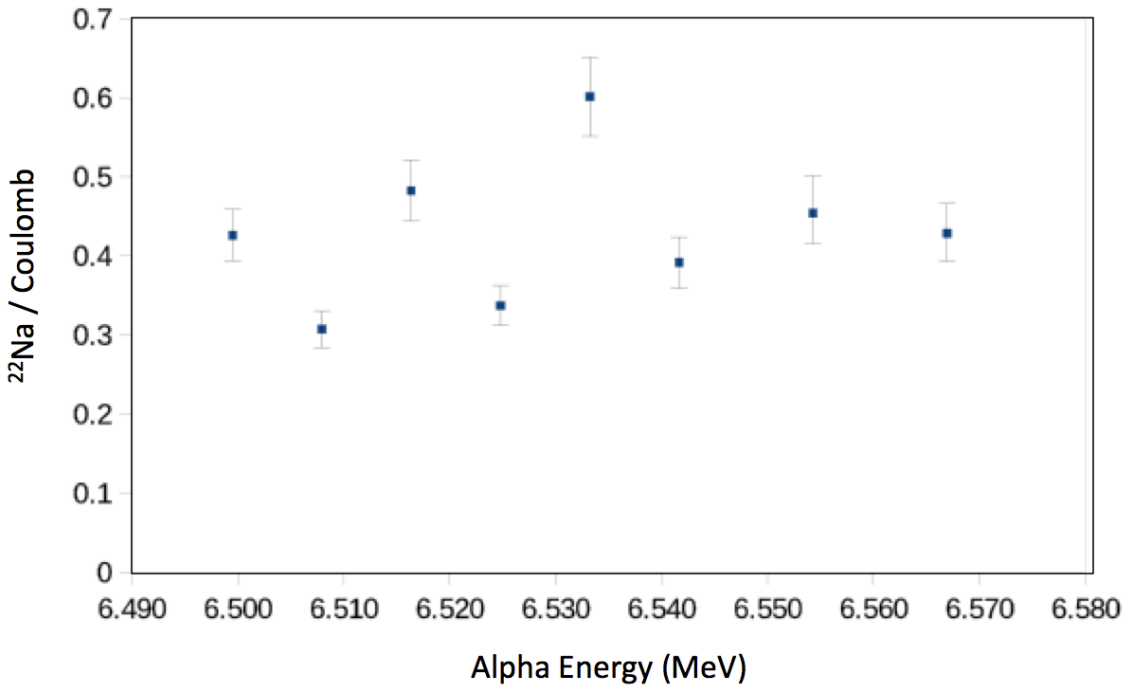

Fig. 3-25. ^{22}Na yield per Coulomb as function of energy at energies near 6.530 MeV as measured at DRS focal plane in the gas ionization counter.

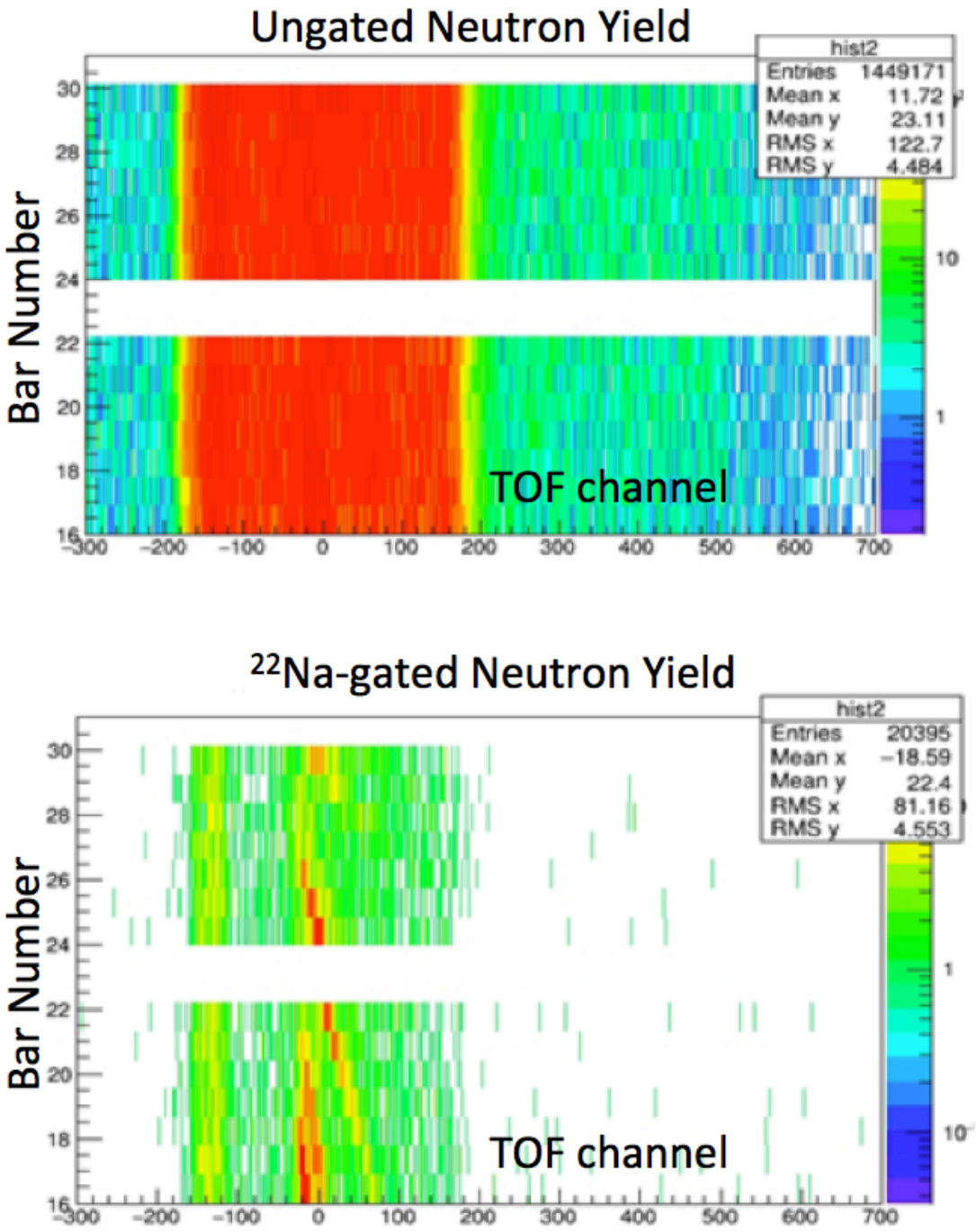

Fig. 3-26. Neutron TOF spectra in the fluorine-beam experiment – ungated (top) and gated on ^{22}Na recoils (bottom).

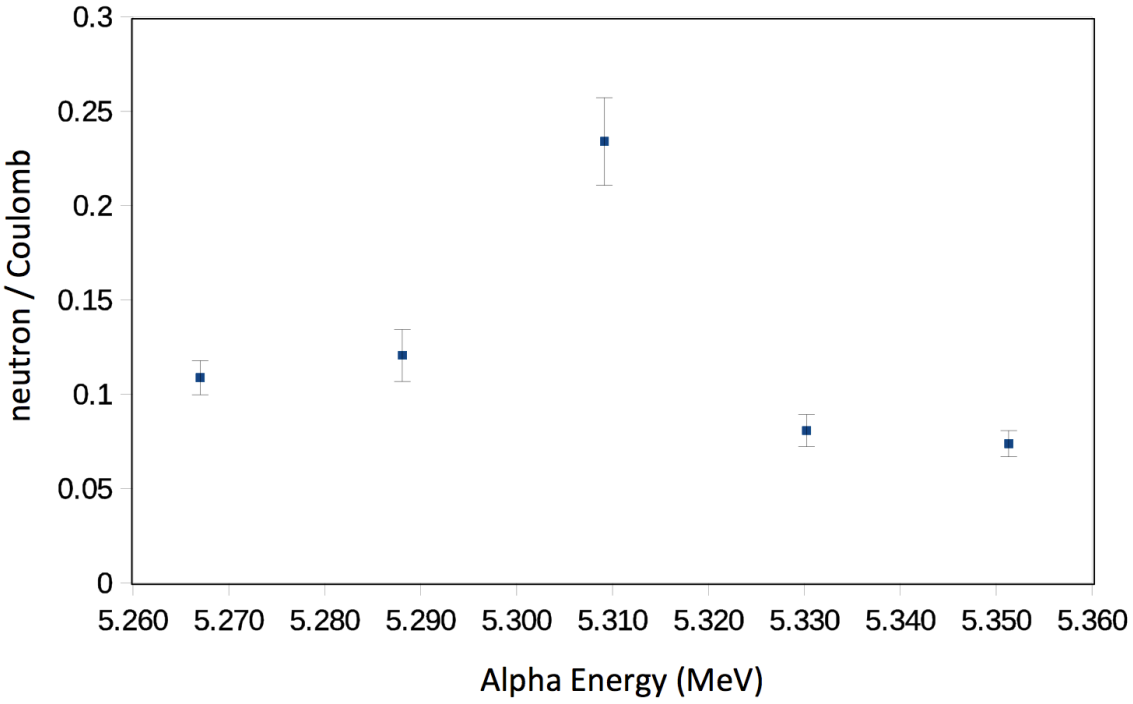

Fig. 3-27. ^{22}Na-gated neutron yield per Coulomb as function of energy at energies near 5.300 MeV as measured in the VANDLE array.

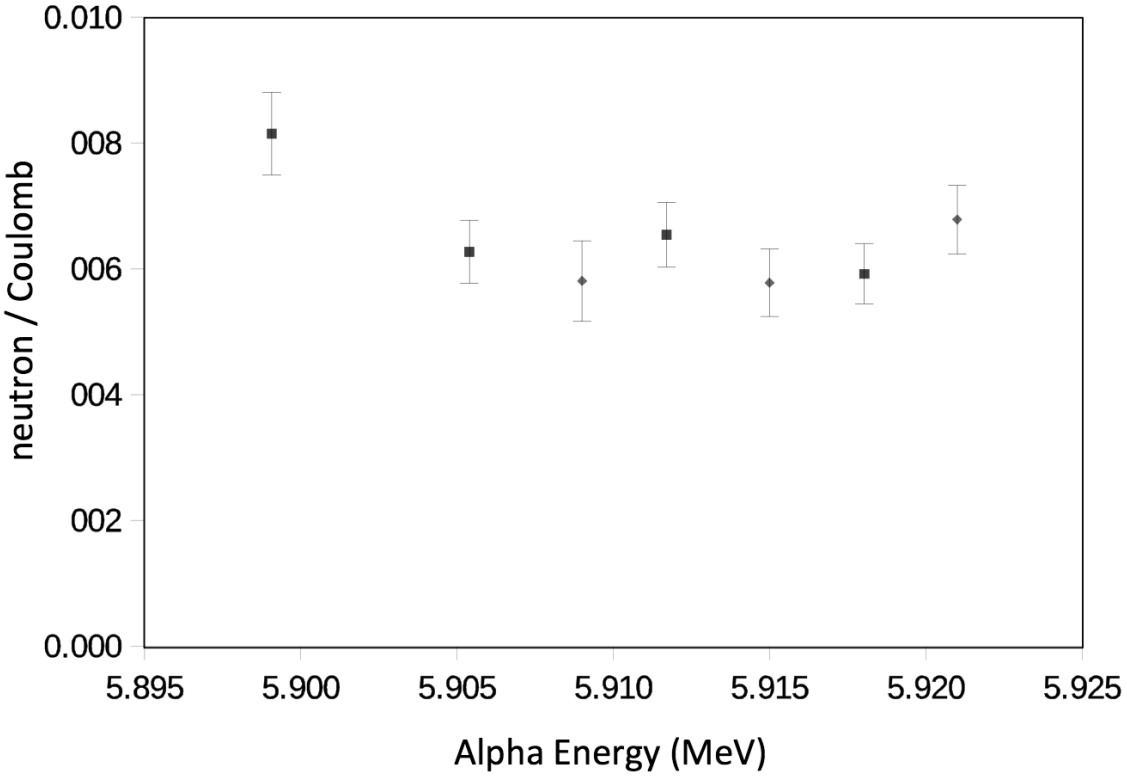

Fig. 3-28. ^{22}Na-gated neutron yield per Coulomb as function of energy at energies near 5.910 MeV as measured in the VANDLE array.

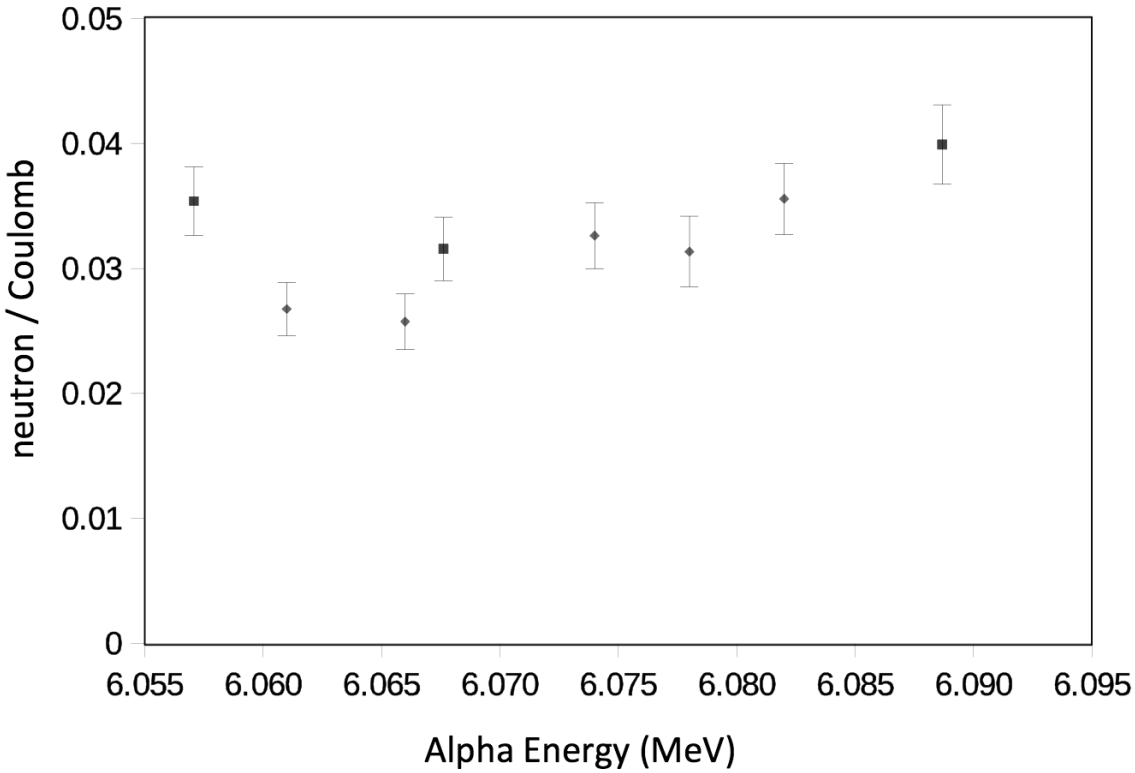

Fig. 3-29. ^{22}Na-gated neutron yield per Coulomb as function of energy at energies near 6.075 MeV as measured in the VANDLE array.

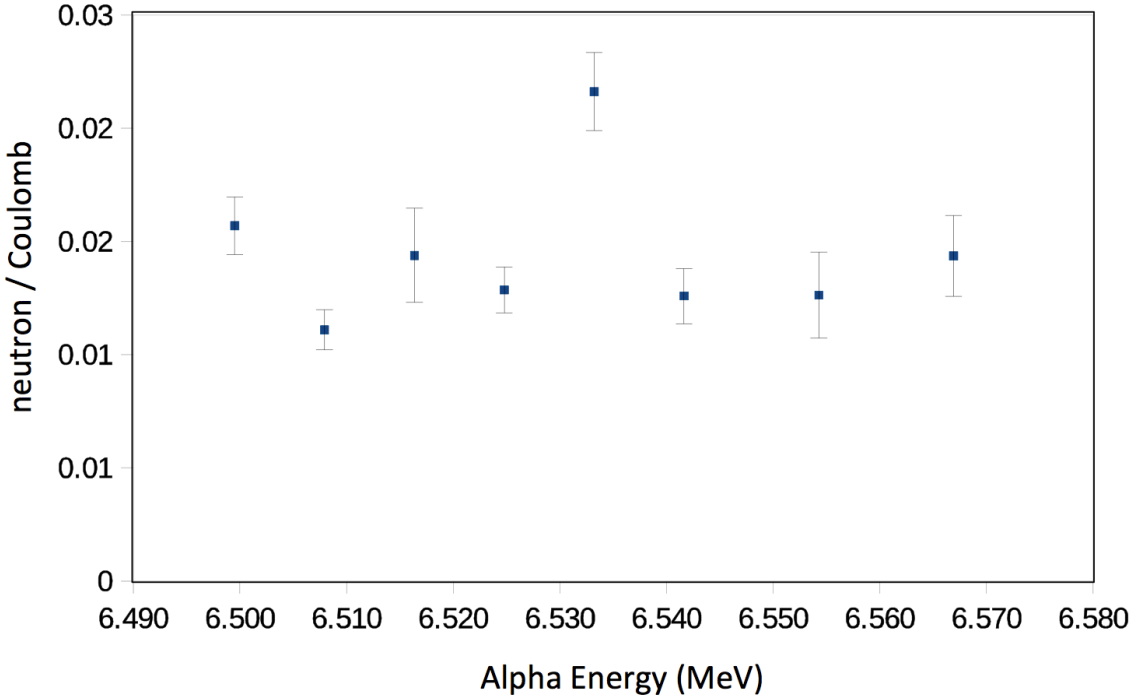

Fig. 3-30. ^{22}Na-gated neutron yield per Coulomb as function of energy at energies near 6.530 MeV as measured in the VANDLE array.

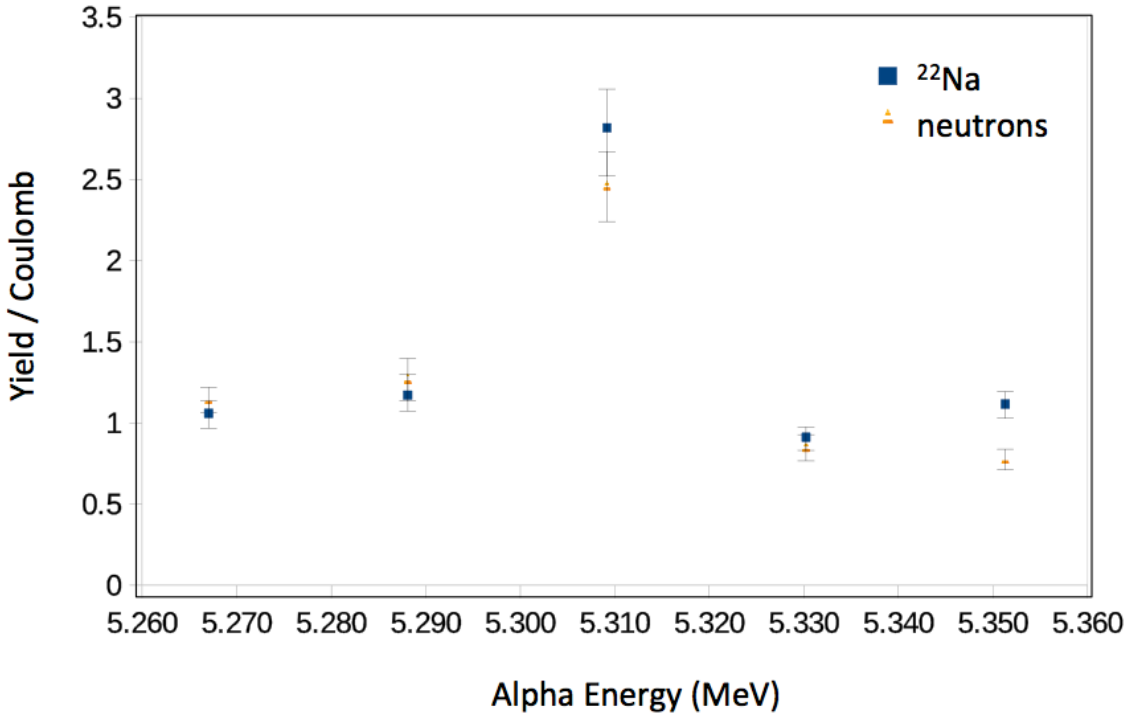

Fig. 3-31. ^{22}Na yield per Coulomb overlaid with scaled ^{22}Na-gated neutron yield per Coulomb as function of energy at energies near 5.300 MeV in the fluorine-beam experiment.

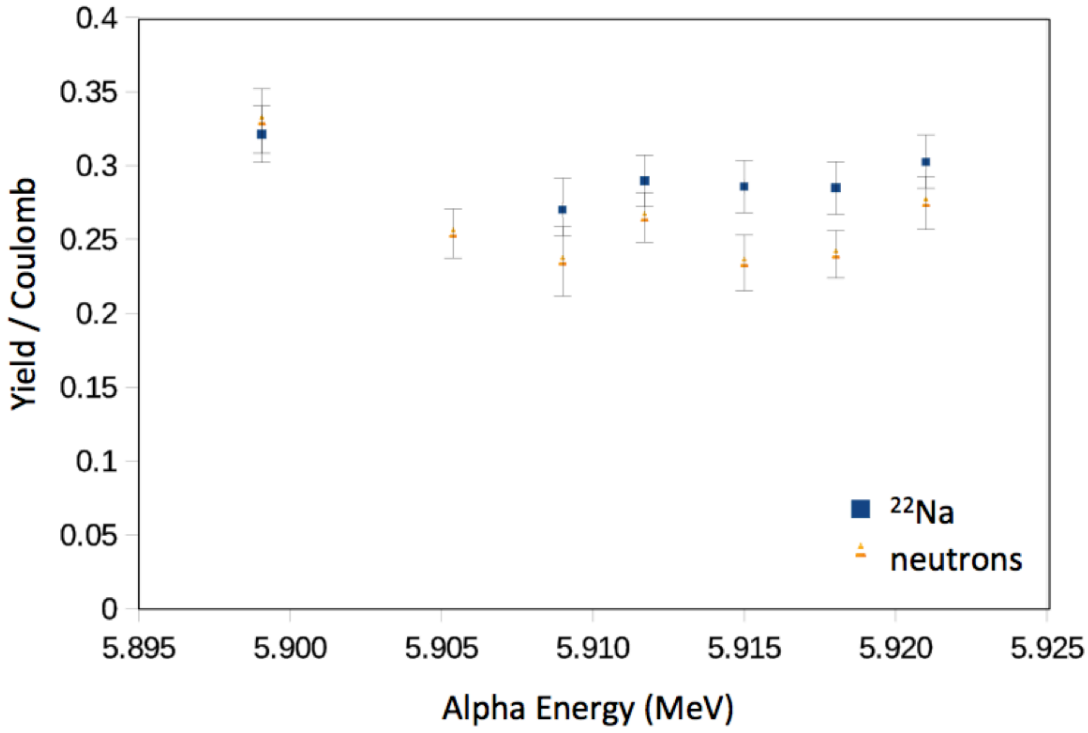

Fig. 3-32. ^{22}Na yield per Coulomb overlaid with scaled ^{22}Na-gated neutron yield per Coulomb as function of energy at energies near 5.910 MeV in the fluorine-beam experiment.

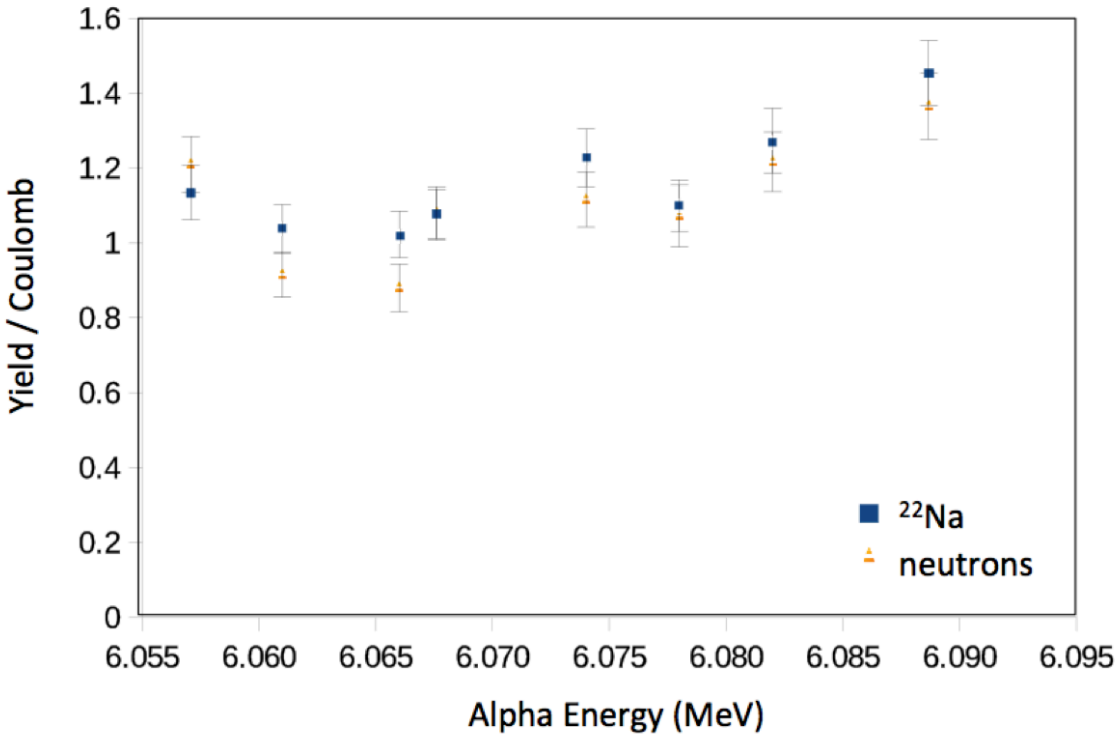

Fig. 3-33. ^{22}Na yield per Coulomb overlaid with scaled ^{22}Na-gated neutron yield per Coulomb as function of energy at energies near 6.075 MeV in the fluorine-beam experiment.

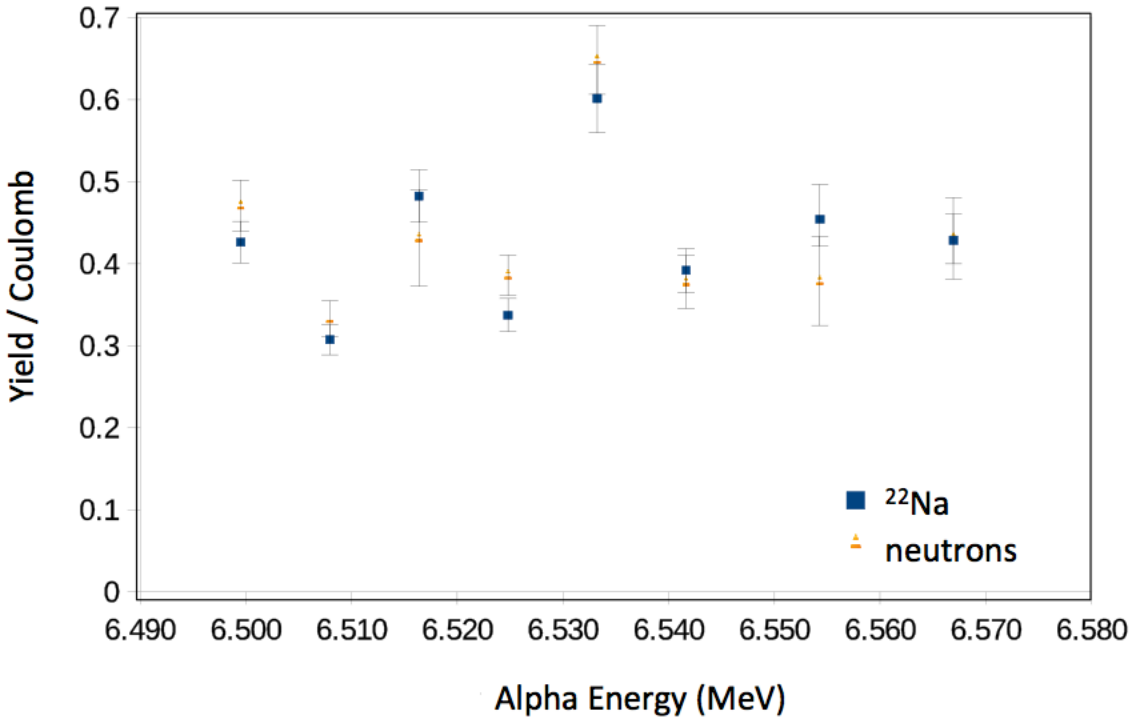

Fig. 3-34. ^{22}Na yield per Coulomb overlaid with scaled ^{22}Na-gated neutron yield per Coulomb as function of energy at energies near 6.530 MeV in the fluorine-beam experiment.

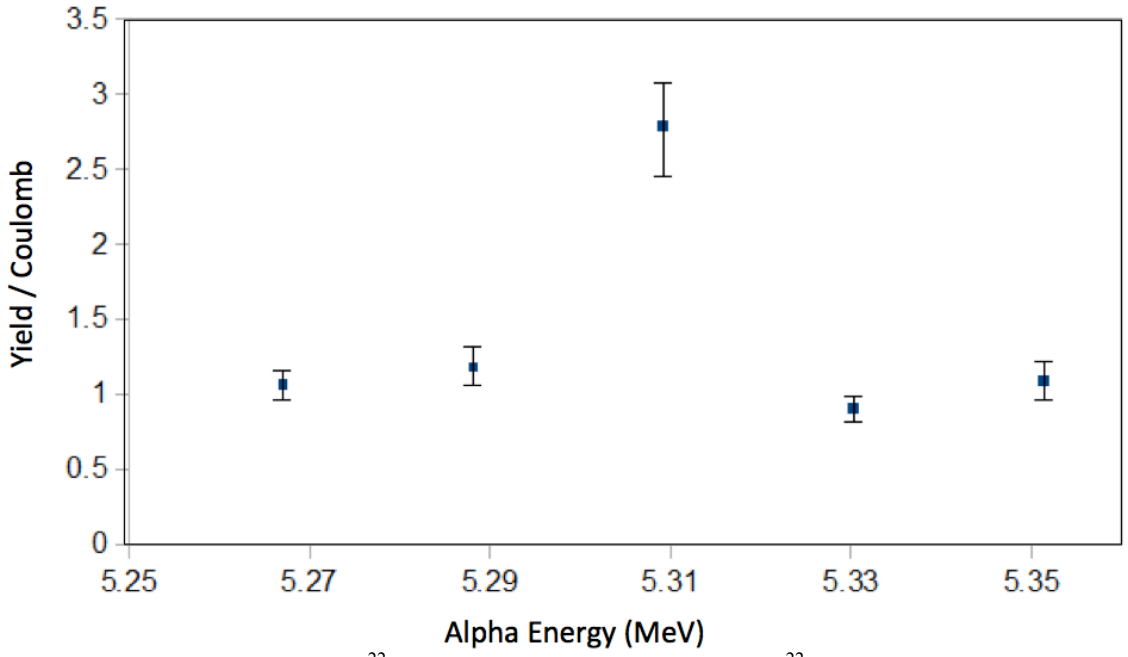

Fig. 3-35. Weighted average of ^{22}Na yield per Coulomb and scaled ^{22}Na-gated neutron yield per Coulomb (relative cross section) as function of energy at energies near 5.300 MeV in the fluorine-beam experiment.

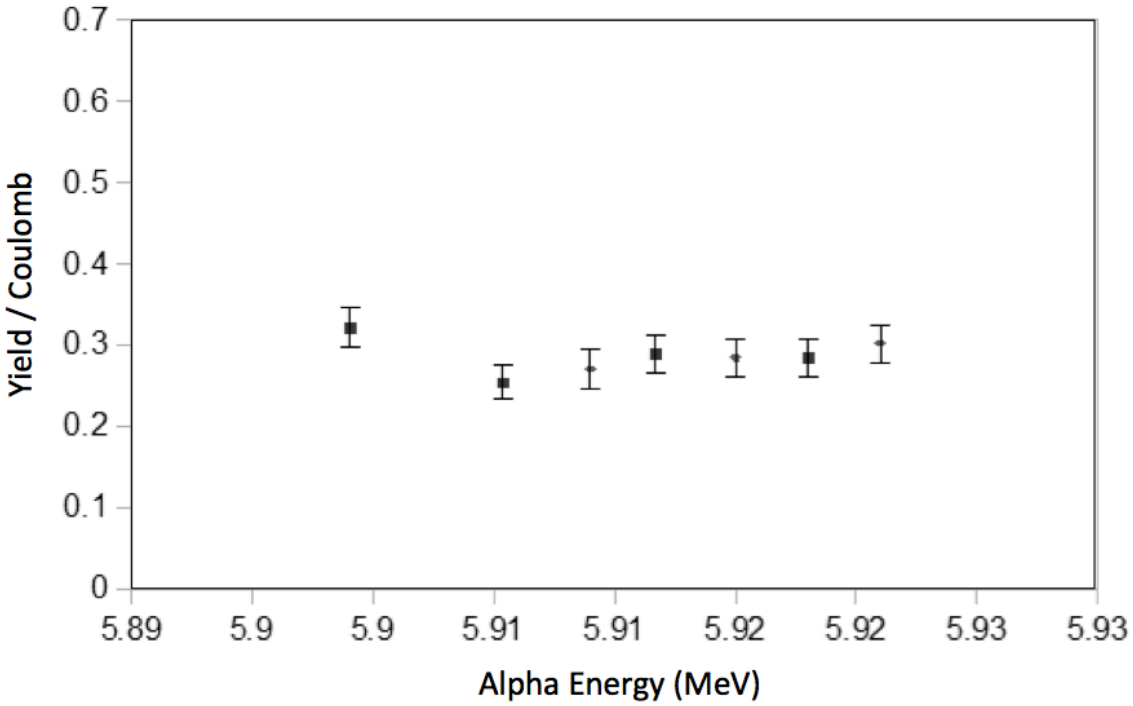

Fig. 3-36. Weighted average of ^{22}Na yield per Coulomb and scaled ^{22}Na-gated neutron yield per Coulomb (relative cross section) as function of energy at energies near 5.910 MeV in the fluorine-beam experiment.

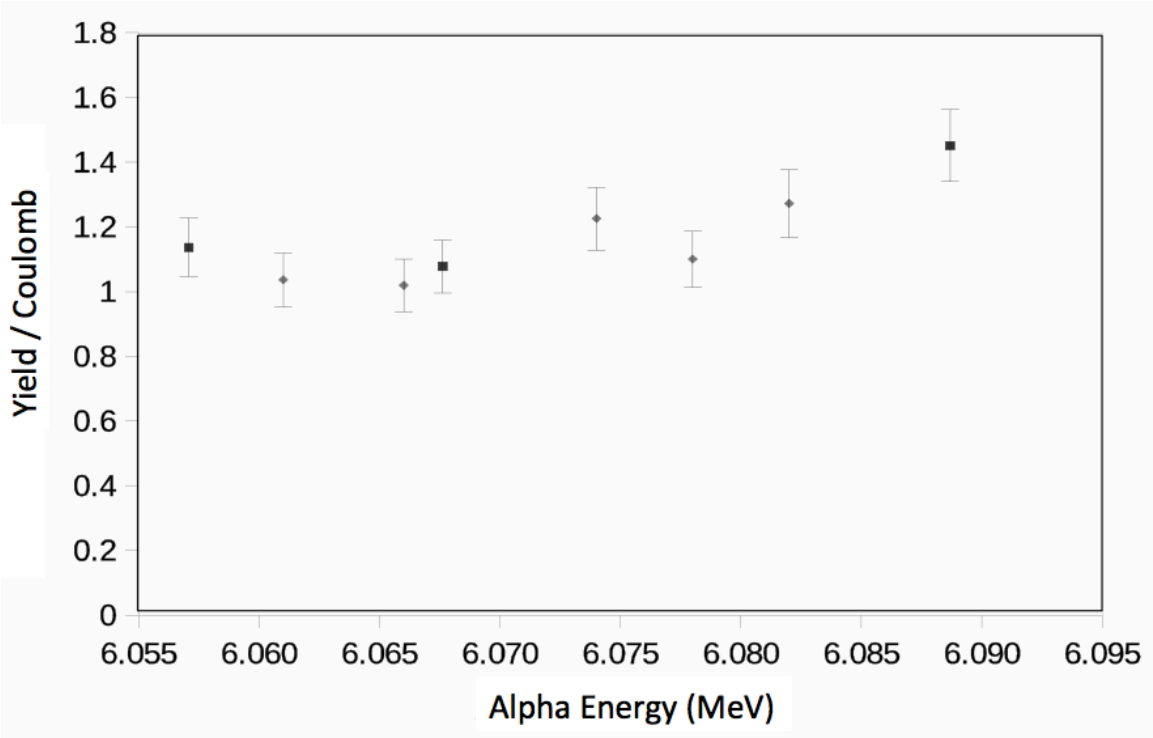

Fig. 3-37. Weighted average of ^{22}Na yield per Coulomb and scaled ^{22}Na-gated neutron yield per Coulomb (relative cross section) as function of energy at energies near 6.075 MeV in the fluorine-beam experiment.

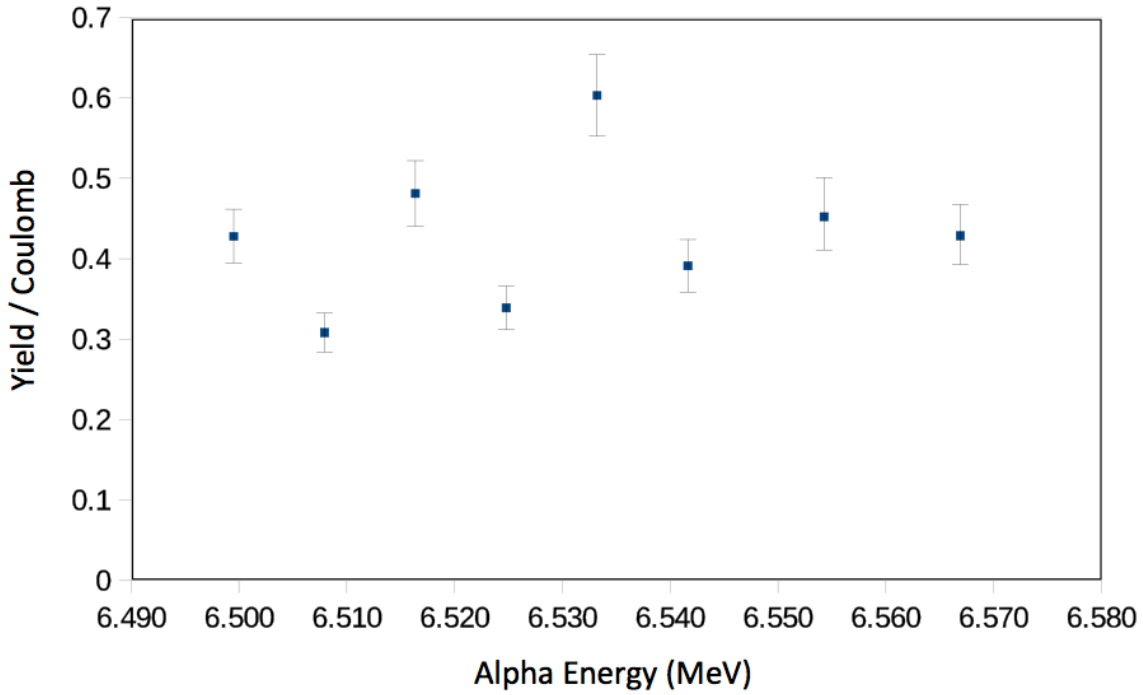

Fig. 3-38. Weighted average of ^{22}Na yield per Coulomb and scaled ^{22}Na-gated neutron yield per Coulomb (relative cross section) as function of energy at energies near 6.530 MeV in the fluorine-beam experiment.

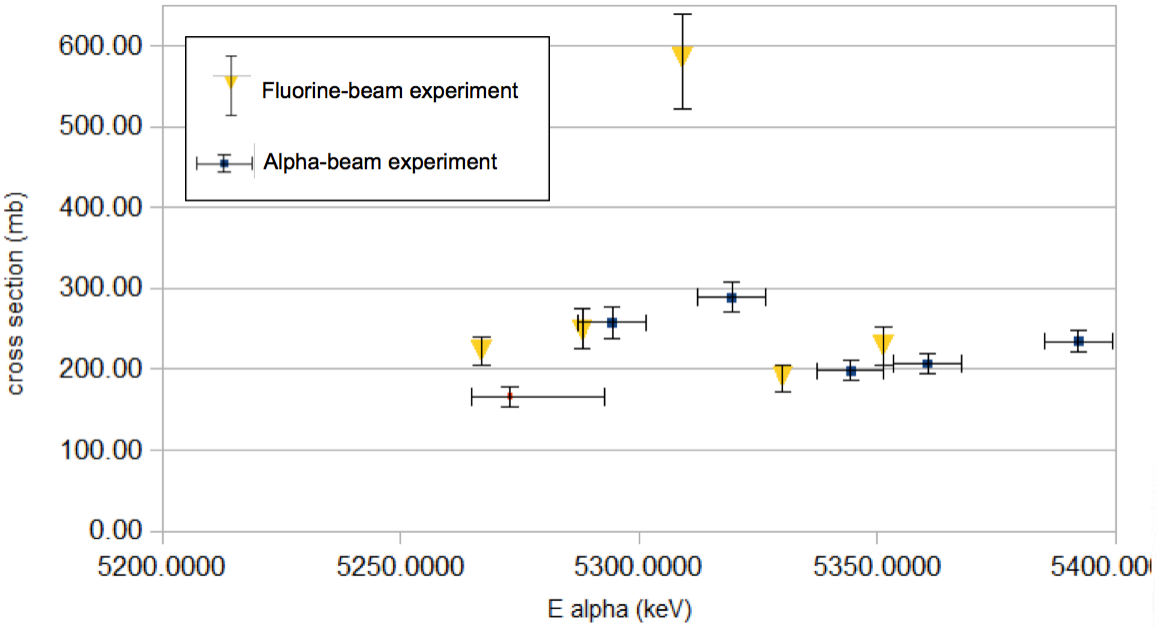

Fig. 3-39. Cross section as a function of energy at energies near 5.300 MeV resulting from scaling the fluorine-beam experiment relative cross section to the absolute cross section from the alpha-beam experiment.

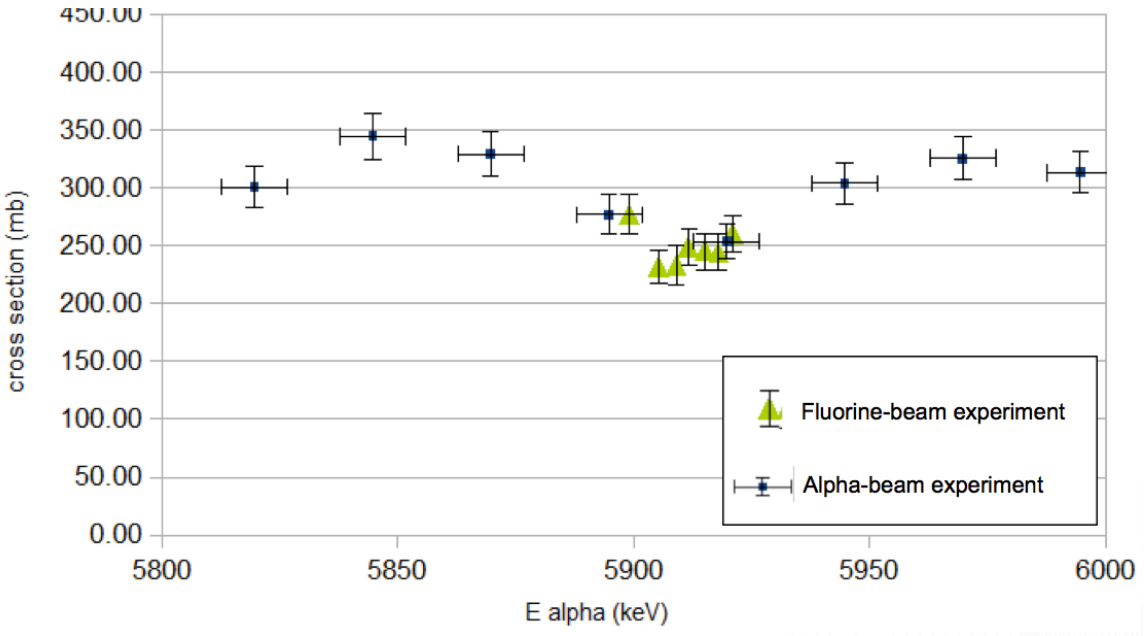

Fig. 3-40. Cross section as a function of energy at energies near 5.910 MeV resulting from scaling the fluorine-beam experiment relative cross section to the absolute cross section from the alpha-beam experiment.

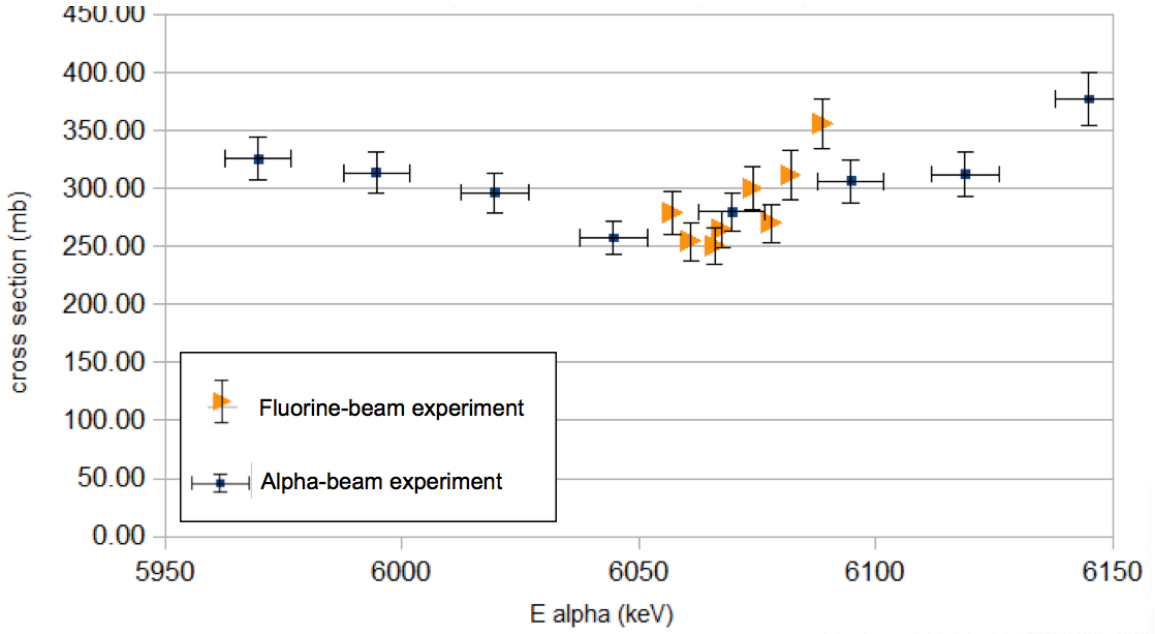

Fig. 3-41. Cross section as a function of energy at energies near 6.075 MeV resulting from scaling the fluorine-beam experiment relative cross section to the absolute cross section from the alpha-beam experiment.

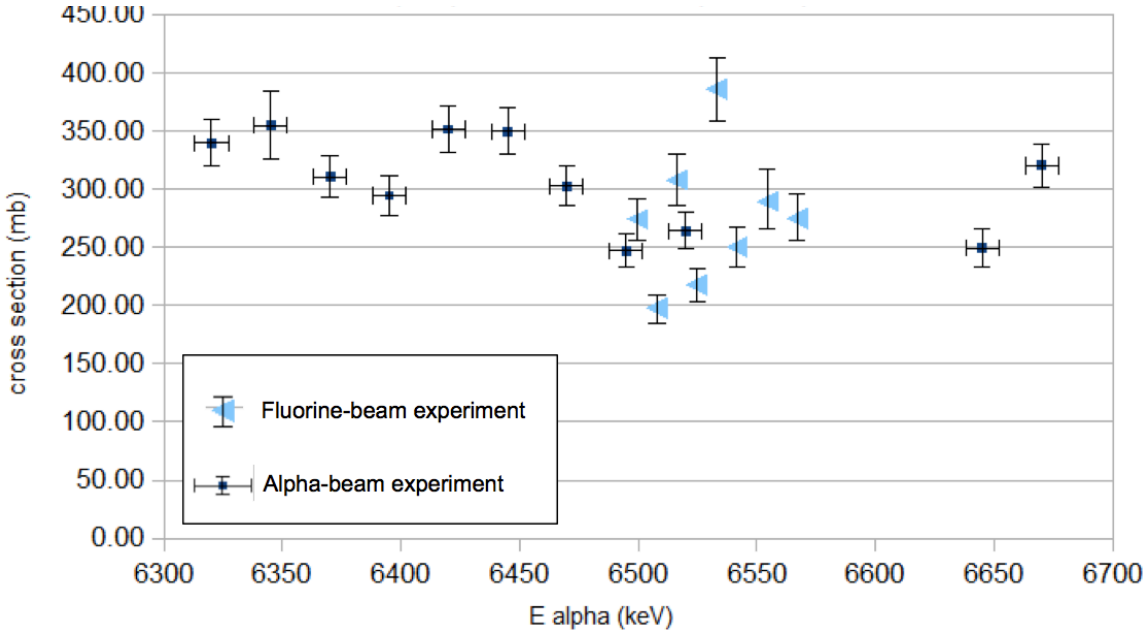

Fig. 3-42. Cross section as a function of energy at energies near 6.530 MeV resulting from scaling the fluorine-beam experiment relative cross section to the absolute cross section from the alpha-beam experiment.

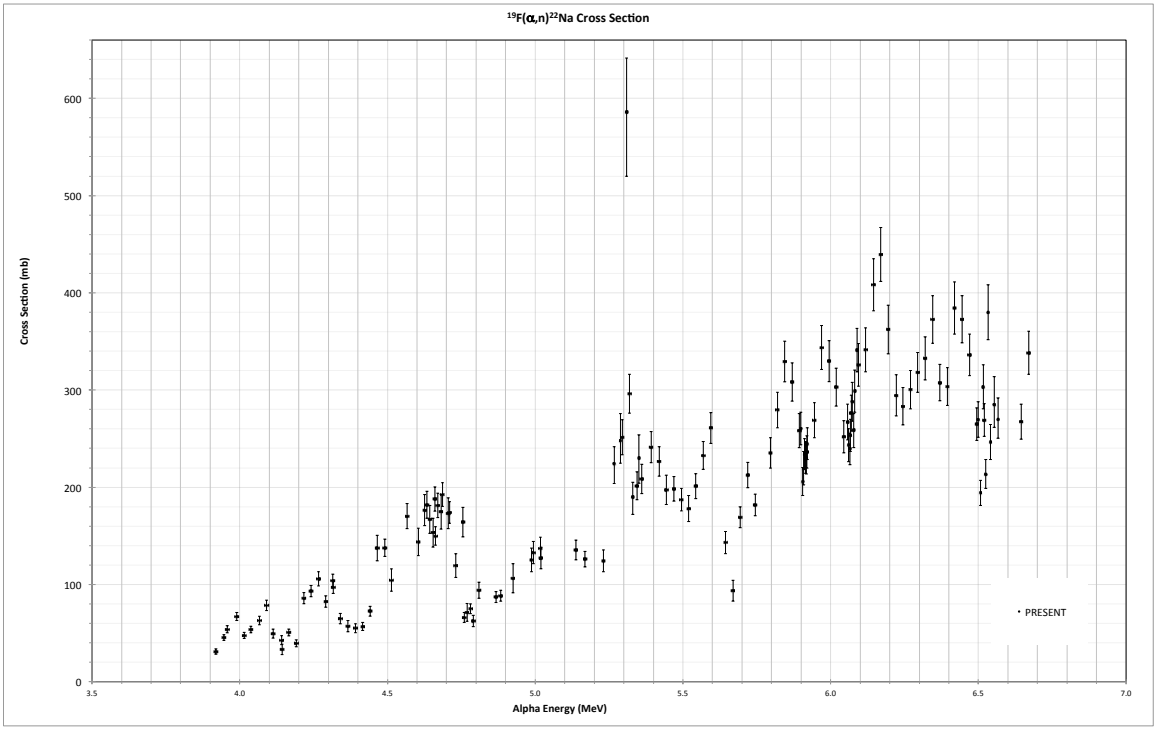

Fig. 3-43. Combined absolute cross section results with both alpha-beam and fluorine-beam experiments, with all uncertainties.

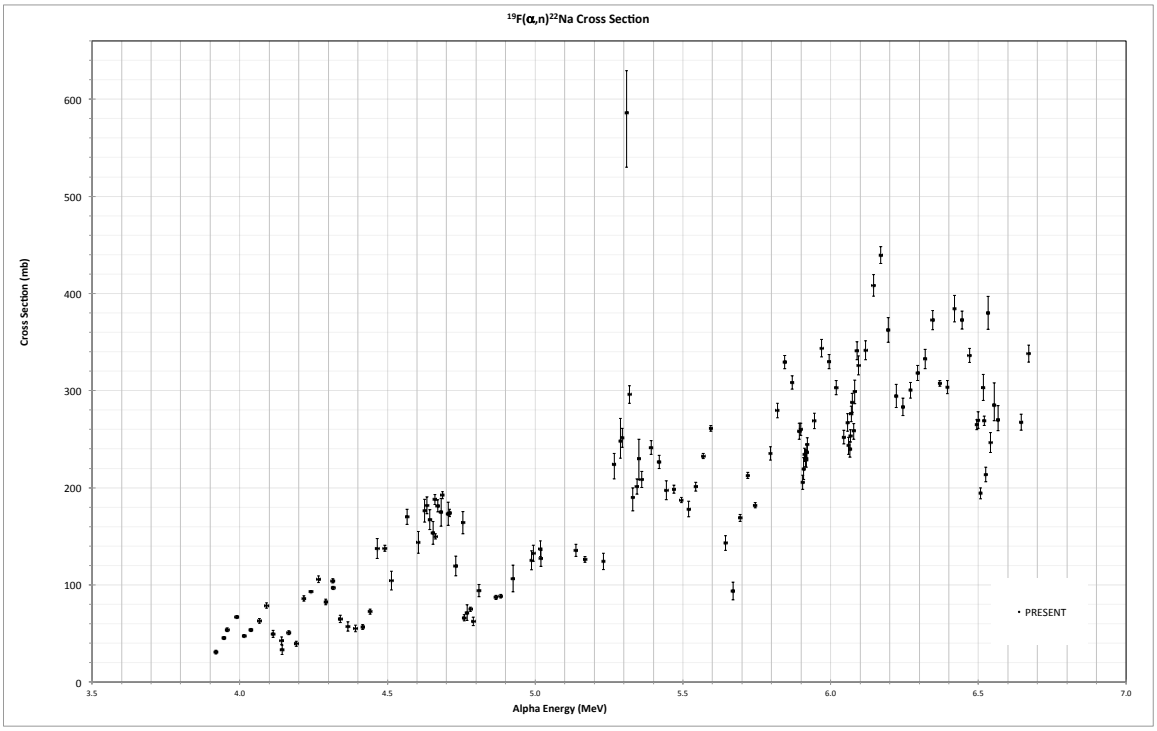

Fig. 3-44. Combined absolute cross section results with both alpha-beam and fluorine-beam experiments, without systematic uncertainties.

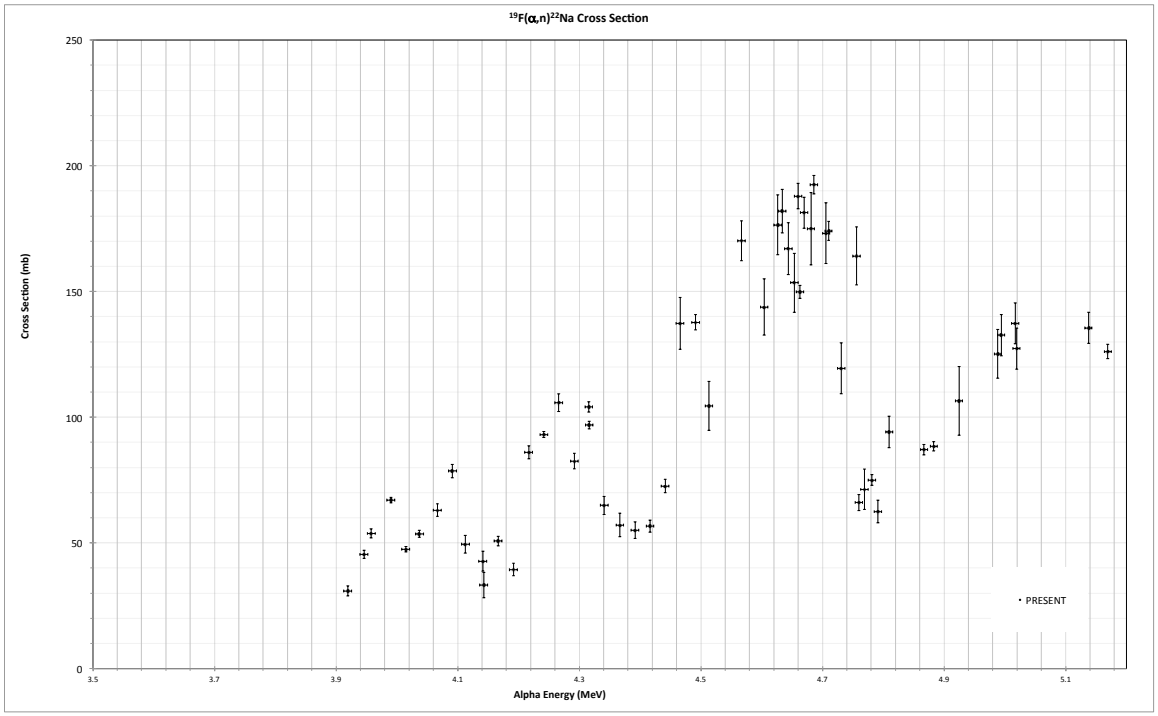

Fig. 3-45. Detailed plot of final results below 5.2 MeV bombarding energy without systematic uncertainties.

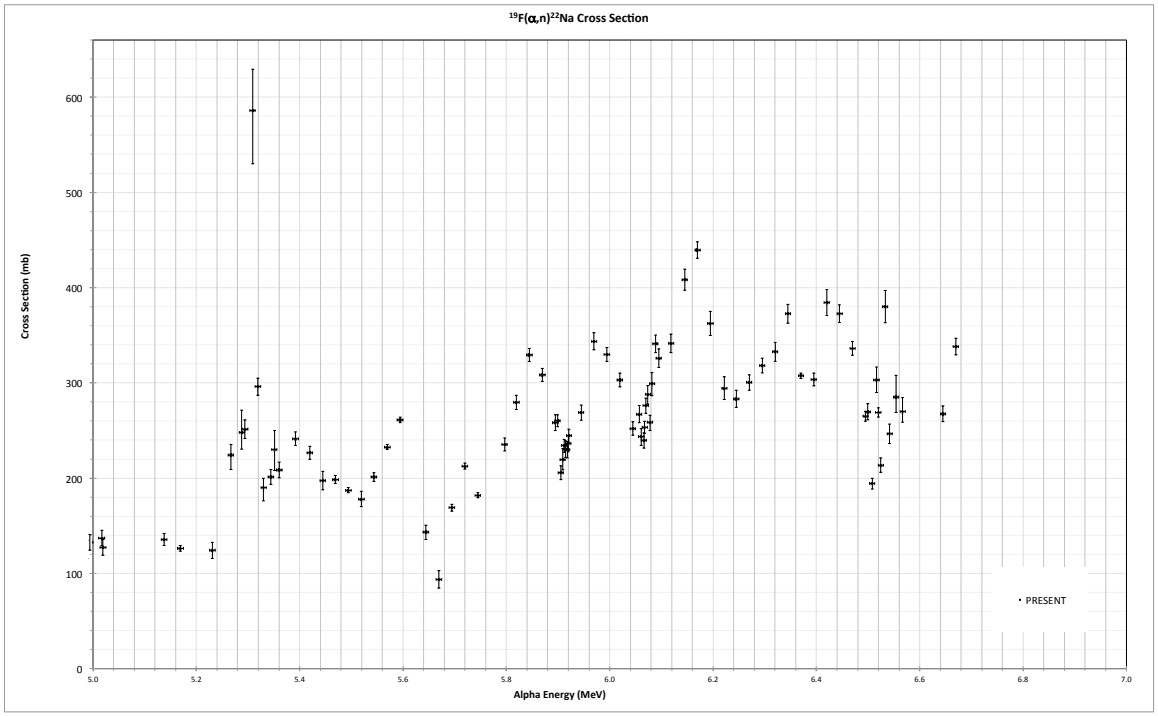

Fig. 3-46. Detailed plot of final results above 5.2 MeV bombarding energy without systematic uncertainties.

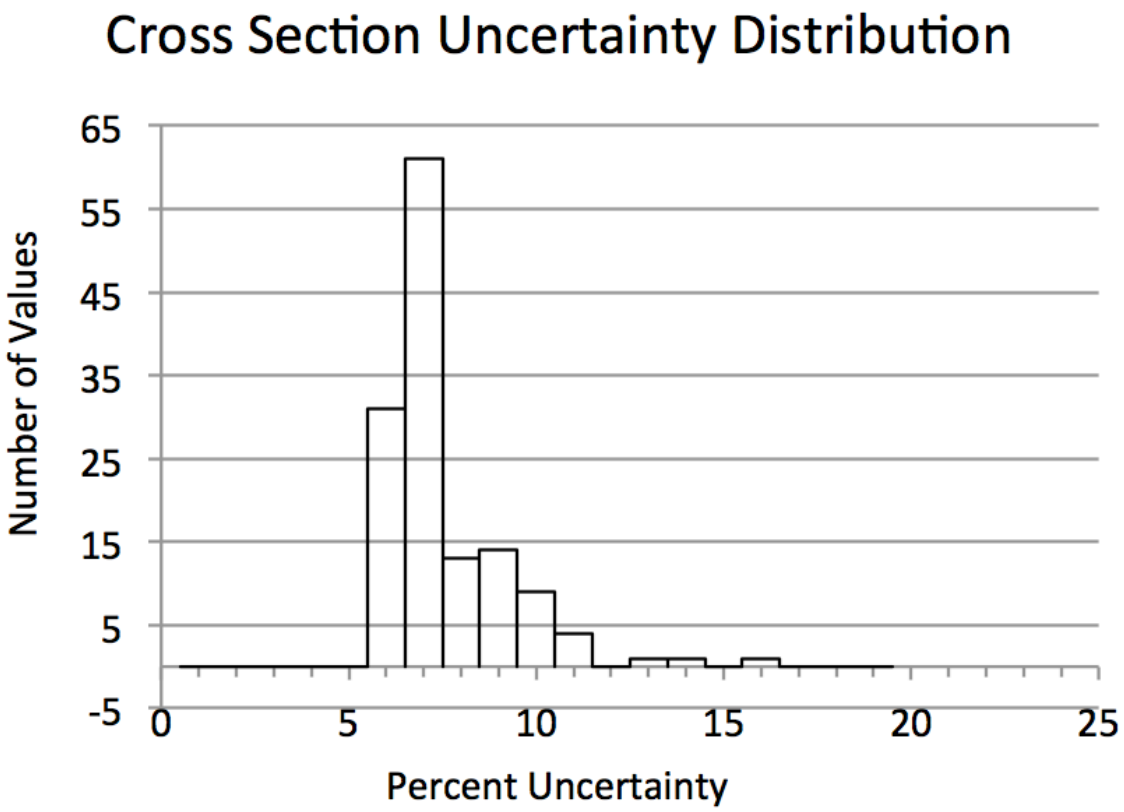

Fig. 3-47. Distribution of percent uncertainties in final data set. The average uncertainty is 7.6%.

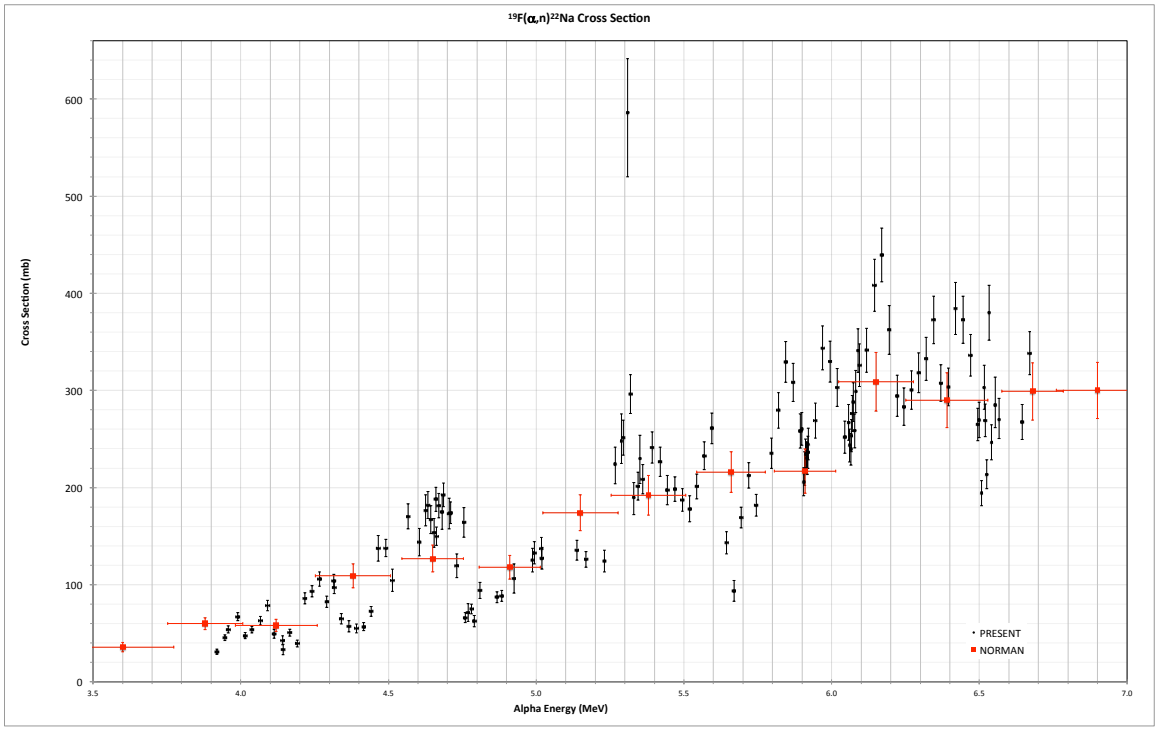

Fig. 4-1. Comparison of present result with the thick target measurement of Norman *et al.* [Nor84].

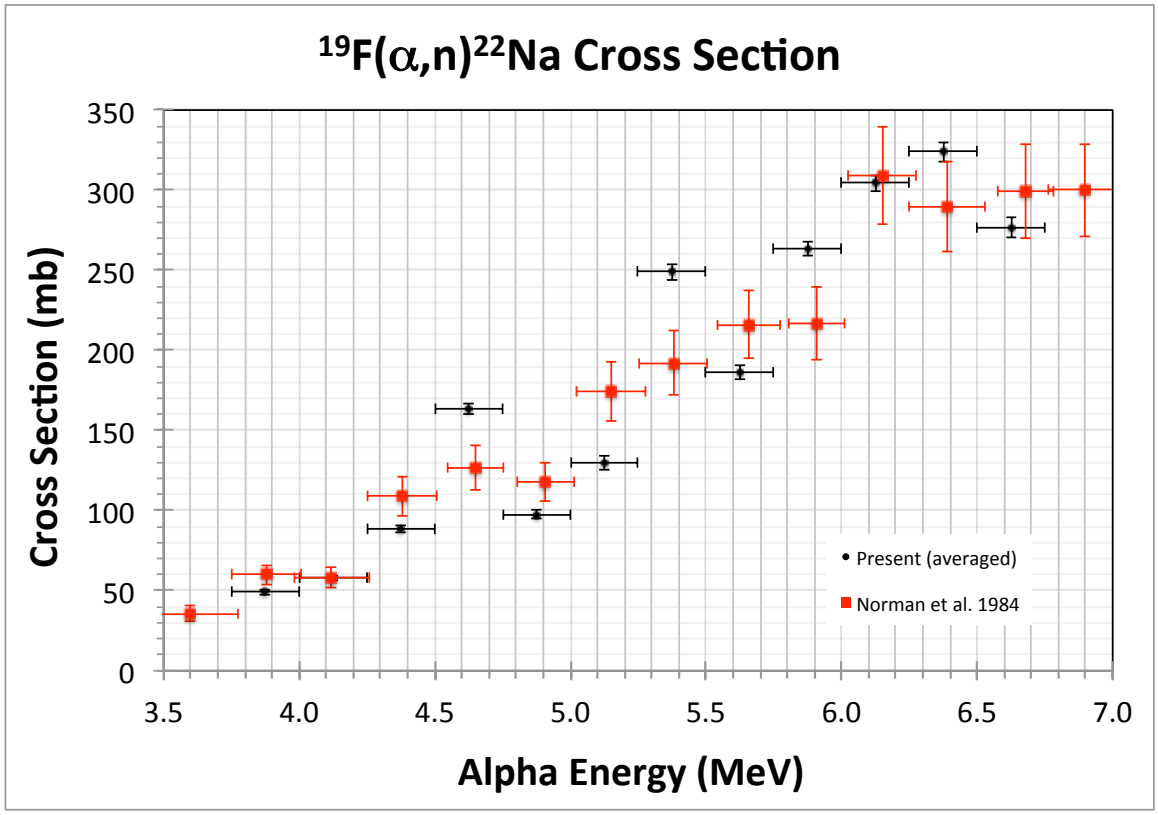

Fig. 4-2. Comparison of an energy-average of present result with Norman *et al.* [Nor84].

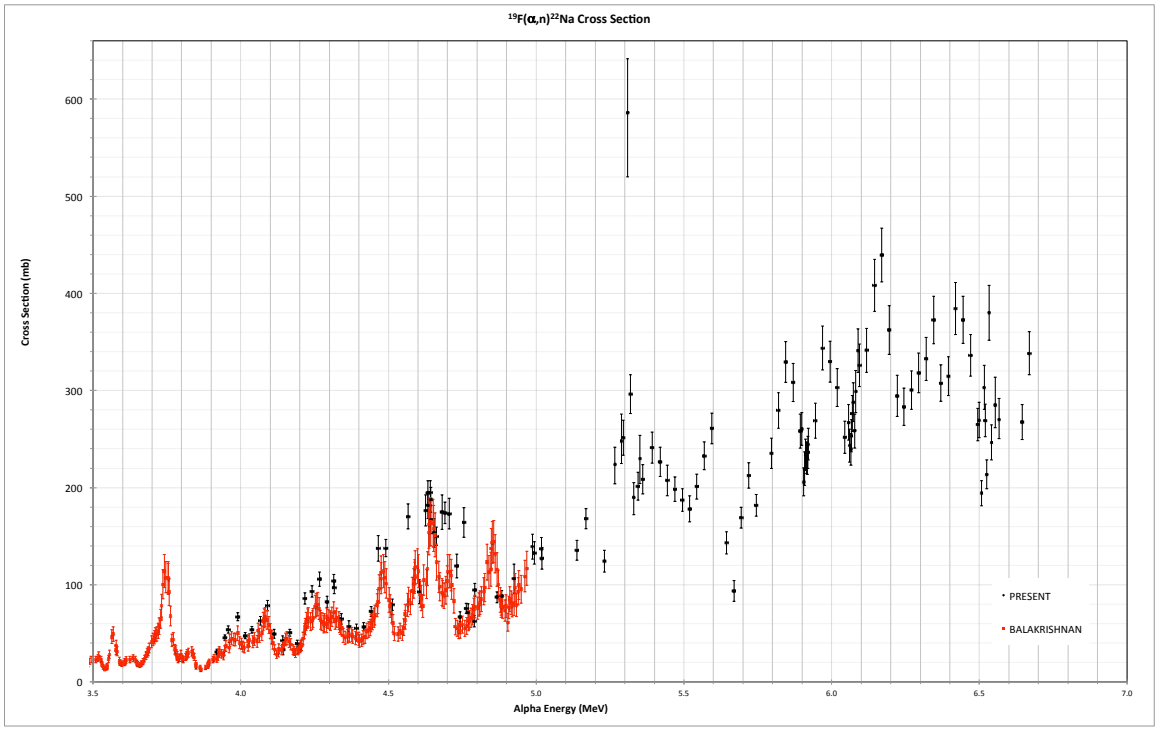

Fig. 4-3. Comparison of present result with the measurement of Balakrishnan *et al.* [Bal78].

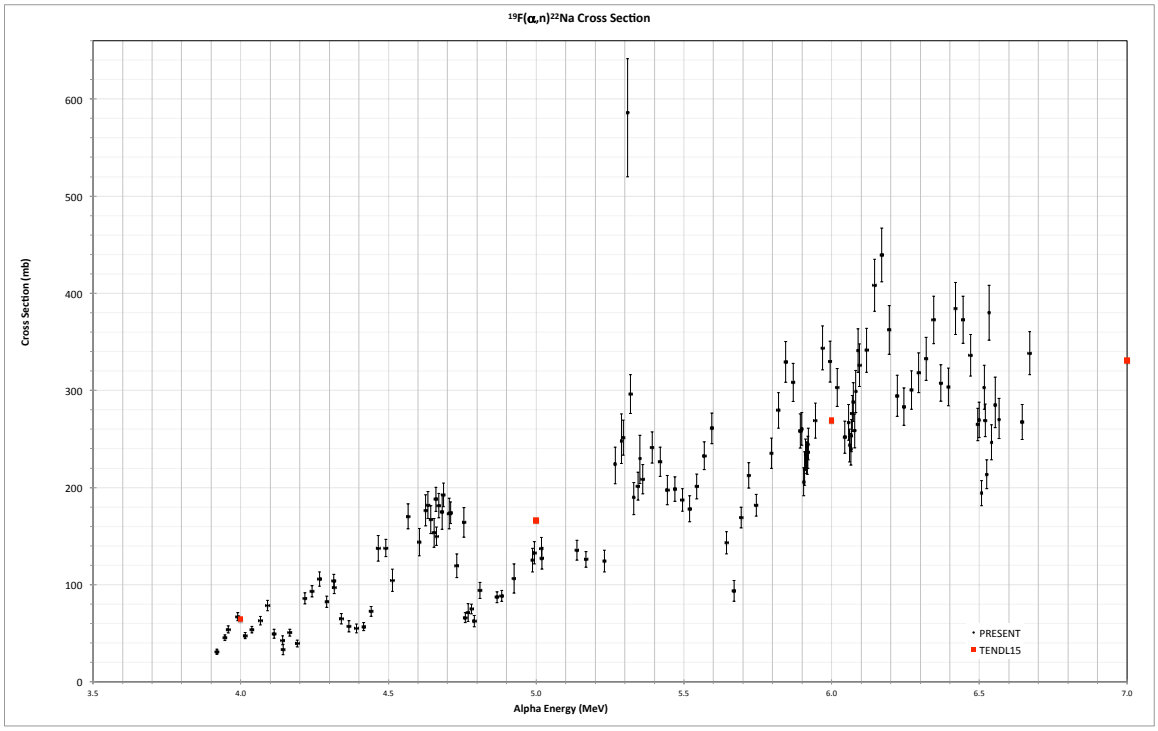

Fig. 4-4. Comparison of present result with the calculated cross section in TENDL [TEN15].

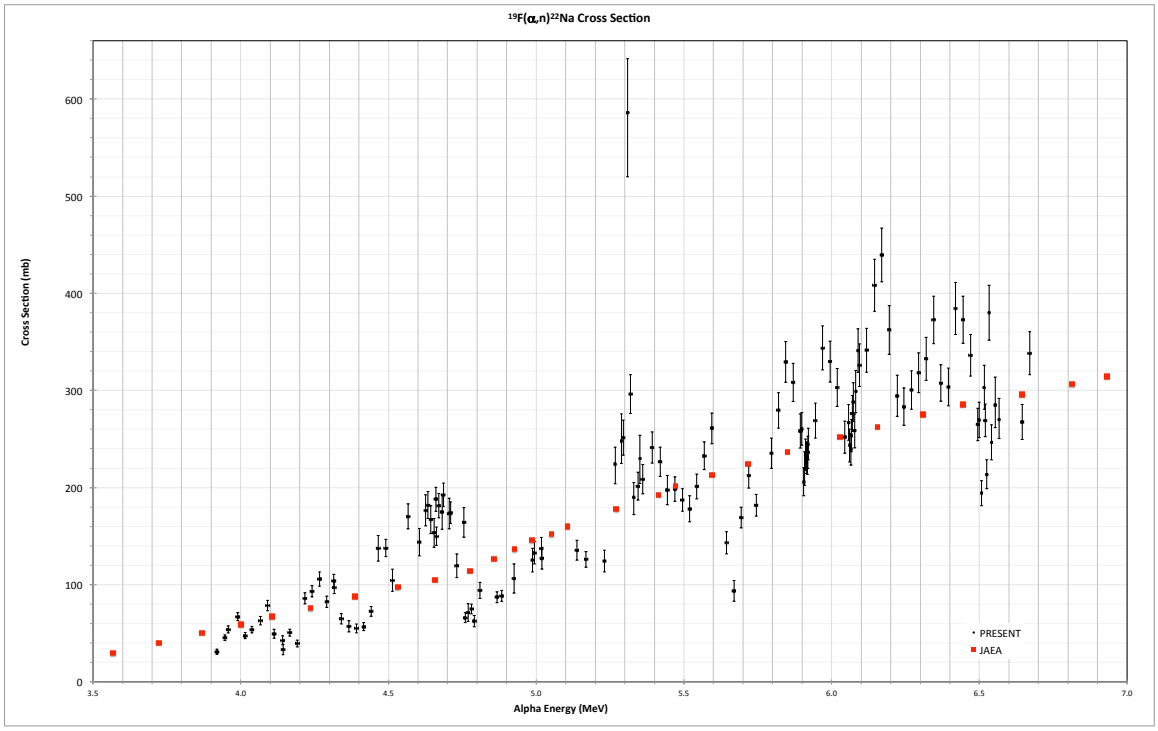

Fig. 4-5. Comparison of present result with the evaluated cross section in JENDL [Mur06].

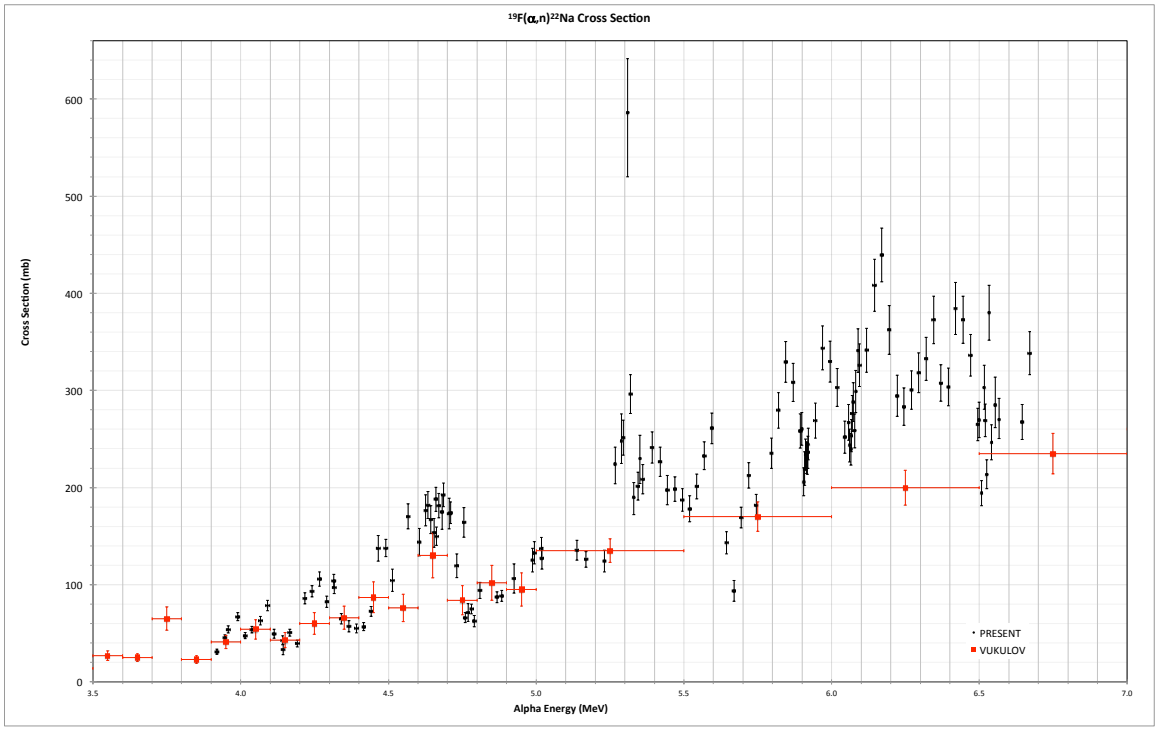

Fig. 4-6. Comparison of present result with the evaluation of Vukulov *et al.* [Vuk83].

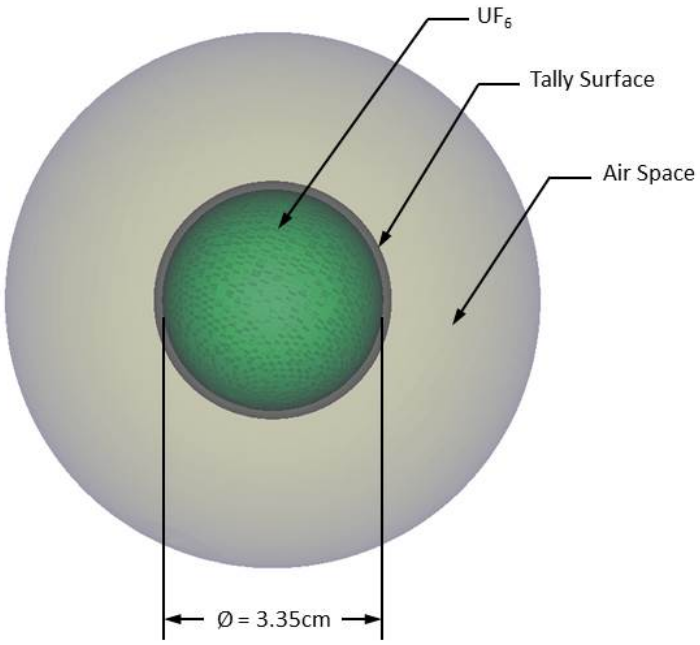

Fig. 5-1. The MCNP6 geometry used for the application impact study of our $^{19}F(\alpha,n)^{22}Na$ cross section. A 100-gram sphere of UF_6 with varying enrichment was modeled in an open air environment. A concentric but larger spherical surface was used to tally the neutron emissions exiting the UF_6 material.

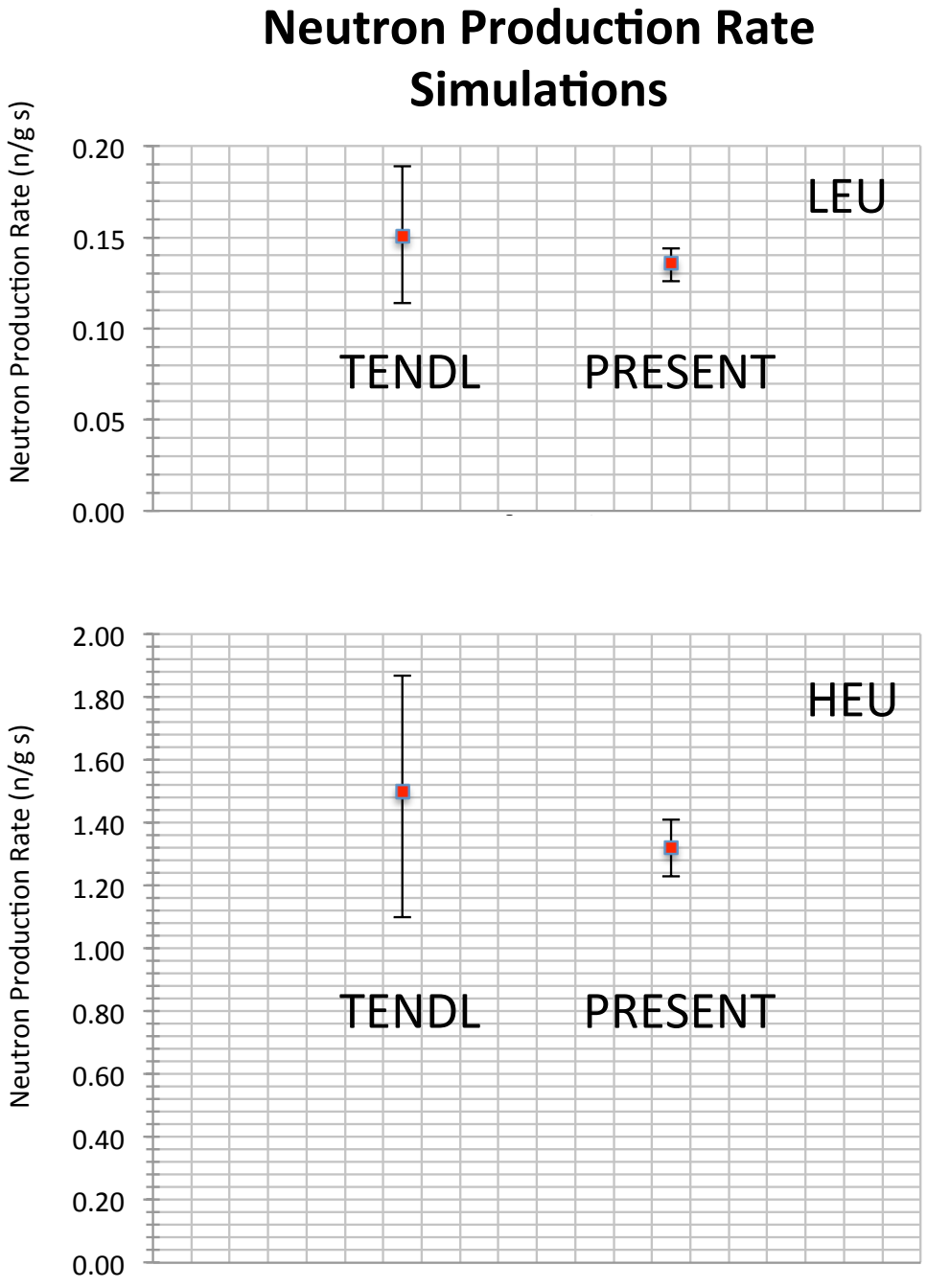

Fig. 5-2. Neutron production rate simulations with different $^{19}F(\alpha,n)^{22}Na$ cross sections. Top: neutron production rate from a 100g sphere of UF_6 (Fig. 5-1) with 3% enriched uranium (LEU) with TENDL and present cross sections. Bottom: similar simulations with a 57.38% enrichment (HEU). Uncertainties in production rates were determined by utilizing maximum and minimum (±1 sigma) values of the cross section as input for the simulation. Use of the present cross section reduces the neutron emission rate by 10% (LEU) and 12% (HEU), and reduces the uncertainty in the neutron emission rate by a factor of 3.6 compared to simulations with the TENDL cross section. Results are tabulated in Table 12.

TABLES

Table 1: Uncertainties from the alpha-beam experiment (§3.a.9).

Component	Uncertainty Contribution %
Statistical yield uncertainties	< 1
Sub-threshold partial cross section	0 - 6
VANDLE detection efficiency	4
beam current	0.1 – 7
target thickness	2
simulation	4
fitting procedure	1 – 13
Total uncertainty	6 – 16

Table 2: Absolute cross section from the alpha-beam experiment (§3.a.11). E_{eff} is the laboratory energy of the alpha particle in the center of target; ΔE_{tgt} is the full energy loss of the beam in the target; σ is the cross section; δσ− and δσ+ are the asymmetric total cross section uncertainties. This data is plotted in Fig. 3-18.

E_{eff} (MeV)	ΔE_{tgt} (MeV)	σ (mb)	δσ− (mb)	δσ+ (mb)
3.92	0.0135	30.9	2.72	2.72
3.95	0.0130	45.4	3.15	3.15
3.96	0.0130	53.8	3.71	3.71
3.99	0.0130	67.0	4.18	4.18
4.01	0.0130	47.5	3.06	3.06
4.04	0.0130	53.6	3.49	3.49
4.07	0.0130	63.0	4.51	4.51
4.09	0.0130	78.6	5.43	5.43
4.11	0.0130	49.5	4.60	4.60
4.14	0.0130	42.7	4.70	4.70
4.143	0.0130	33.2	5.41	5.41
4.17	0.0130	50.7	3.59	3.59
4.19	0.0130	39.4	3.44	3.44
4.22	0.0125	86.0	5.78	5.78
4.24	0.0125	93.1	5.71	5.71
4.27	0.0125	106.0	7.26	7.26
4.29	0.0125	82.5	5.83	5.83
4.316	0.0125	104.0	6.57	6.57
4.32	0.0125	96.9	6.01	6.01
4.34	0.0125	64.9	5.35	5.35
4.37	0.0125	57.1	5.80	5.80
4.39	0.0125	55.1	4.67	4.67
4.42	0.0125	56.6	4.14	4.14
4.44	0.0125	72.6	5.12	5.12
4.47	0.0125	137.0	13.22	13.22
4.49	0.0125	138.0	8.80	8.80
4.51	0.0120	104.0	11.56	11.56
4.57	0.0120	170.0	12.91	12.91
4.604	0.0120	144.0	14.14	14.14
4.626	0.0120	176.0	15.91	15.91
4.634	0.0120	182.0	13.99	13.99
4.644	0.0120	167.0	14.36	14.36
4.654	0.0120	153.0	14.91	14.91
4.66	0.0120	188.0	12.37	12.37
4.663	0.0120	150.0	9.37	9.37
4.67	0.0120	181.0	12.52	12.52
4.681	0.0120	175.0	17.80	17.80
4.686	0.0120	192.0	12.12	12.12
4.706	0.0120	173.0	15.91	15.91
4.71	0.0120	174.0	11.12	11.12
4.731	0.0120	119.0	12.41	12.41
4.756	0.0120	164.0	15.16	15.16

4.76	0.0120	66.0	5.09	5.09
4.769	0.0120	71.3	9.12	9.12
4.78	0.0120	75.0	4.99	4.99
4.791	0.0120	62.5	5.94	5.94
4.81	0.0120	94.1	8.46	8.46
4.87	0.0115	87.1	5.63	5.63
4.88	0.0115	88.4	5.63	5.63
4.92	0.0115	107.0	15.11	15.11
4.99	0.0115	125.0	12.27	12.27
4.994	0.0115	133.0	11.45	11.45
5.02	0.0115	137.0	11.56	11.56
5.019	0.0115	127.0	11.21	11.21
5.14	0.0115	136.0	10.20	10.20
5.169	0.0115	126.0	8.09	8.09
5.23	0.0110	124.0	11.22	11.22
5.294	0.0110	251.0	18.03	18.03
5.319	0.0110	296.0	19.97	19.97
5.344	0.0110	201.0	14.43	14.43
5.361	0.0110	209.0	15.09	15.09
5.392	0.0110	241.0	16.11	16.11
5.419	0.0110	227.0	15.26	15.26
5.445	0.0110	197.0	15.29	15.29
5.470	0.0110	198.0	12.58	12.58
5.495	0.0110	187.0	11.58	11.58
5.519	0.0110	178.0	13.31	13.31
5.544	0.0110	201.0	12.91	12.91
5.570	0.0110	233.0	14.21	14.21
5.594	0.0110	261.0	15.92	15.92
5.644	0.0110	143.0	11.47	11.47
5.669	0.0110	93.7	10.69	10.69
5.694	0.0110	169.0	10.76	10.76
5.720	0.0105	213.0	13.11	13.11
5.745	0.0105	182.0	11.26	11.26
5.797	0.0105	235.0	15.77	15.77
5.820	0.0105	280.0	18.38	18.38
5.845	0.0105	329.0	20.96	20.96
5.870	0.0105	308.0	19.73	19.73
5.895	0.0105	258.0	17.57	17.57
5.920	0.0105	236.0	16.55	16.55
5.945	0.0105	269.0	17.99	17.99
5.970	0.0105	343.7	22.52	22.52
5.995	0.0105	329.7	21.08	21.08
6.020	0.0105	303.0	19.56	19.56
6.045	0.0105	252.0	16.68	16.68
6.070	0.0105	276.0	18.49	18.49
6.095	0.0105	326.0	21.90	21.90
6.119	0.0105	341.0	22.69	22.69

6.145	0.0105	408.0	26.90	26.90
6.170	0.0105	439.0	27.74	27.74
6.195	0.0105	362.0	25.15	25.15
6.222	0.0100	294.0	21.28	21.28
6.245	0.0100	283.0	19.25	19.25
6.270	0.0100	300.0	19.77	19.77
6.295	0.0100	318.0	20.61	20.61
6.320	0.0100	333.0	22.32	22.32
6.345	0.0100	373.0	24.42	24.42
6.370	0.0100	308.0	18.69	18.69
6.395	0.0100	304.0	19.43	19.43
6.420	0.0100	384.0	26.82	26.82
6.445	0.0100	373.0	24.23	24.23
6.470	0.0100	336.0	21.42	21.42
6.495	0.0100	265.0	16.71	16.71
6.520	0.0100	269.0	16.87	16.87
6.645	0.0100	268.0	18.02	18.02
6.670	0.0100	338.0	22.16	22.16

Table 3: Uncertainties for relative cross sections based on ^{22}Na yields from the fluorine-beam experiment (§3.b.4).

Component	Uncertainty Contribution %
Statistical yield uncertainties	< 1
Systematic yield uncertainties	6
Event selection	2 – 10
beam / target normalization	< 1
Total uncertainty	7 – 12

Table 4: Relative yield per Coulomb from the fluorine-beam experiment based on ^{22}Na yields (§3.b.4). E_{eff} is the effective laboratory energy of an alpha particle in the center of target corresponding to the same center of mass energy as the laboratory energy of the fluorine beam; ΔE_{tgt} is the full energy loss of the beam in the target; δY− and δY+ are the asymmetric uncertainties in the ^{22}Na yield per Coulomb.

E_{eff} (MeV)	ΔE_{tgt} (MeV)	^{22}Na Yield (cts/Coulomb)	δY− (cts/Coulomb)	δY+ (cts/Coulomb)
5.267	0.005	1.06	0.090	0.080
5.288	0.005	1.17	0.100	0.130
5.309	0.005	2.82	0.300	0.250
5.330	0.005	0.91	0.080	0.070
5.351	0.005	1.12	0.090	0.080
5.899	0.005	0.32	0.021	0.021
5.905		Neutrons only		
5.909	0.005	0.27	0.020	0.021
5.912	0.005	0.29	0.019	0.019
5.915	0.005	0.29	0.019	0.019
5.918	0.005	0.28	0.019	0.019
5.921	0.005	0.30	0.020	0.020
6.057	0.005	1.13	0.080	0.080
6.061	0.005	1.04	0.070	0.070
6.066	0.005	1.02	0.070	0.070
6.068	0.005	1.08	0.070	0.070
6.074	0.005	1.23	0.080	0.080
6.078	0.005	1.10	0.080	0.070
6.082	0.005	1.27	0.090	0.090
6.089	0.005	1.45	0.090	0.090
6.500	0.005	0.43	0.030	0.030
6.508	0.005	0.31	0.020	0.020
6.516	0.005	0.48	0.030	0.030
6.525	0.005	0.34	0.022	0.022
6.533	0.005	0.60	0.040	0.040
6.542	0.005	0.39	0.030	0.030
6.554	0.005	0.45	0.030	0.040
6.567	0.005	0.43	0.030	0.030

Table 5: Uncertainties for relative cross sections based on ^{22}Na-gated neutron yields in the fluorine-beam experiment (§3.b.5).

Component	Uncertainty Contribution %
Statistical yield uncertainties	1 – 14
Systematic yield uncertainties	6
Beam / target normalization	< 1
Total	7 – 14

Table 6: Relative yield per Coulomb from the fluorine-beam experiment based on ^{22}Na-gated neutron yields (§3.b.5). E_{eff} is the effective laboratory energy of an alpha particle in the center of target corresponding to the same center of mass energy as the laboratory energy of the fluorine beam; ΔE_{tgt} is the full energy loss of the beam in the target; δY is the uncertainty in the neutron yield per Coulomb.

E_{eff} (MeV)	ΔE_{tgt} (MeV)	Neutron Yield (cts/Coulomb)	δY (cts/Coulomb)
5.267	0.005	0.109	0.0080
5.288	0.005	0.121	0.0130
5.309	0.005	0.230	0.0210
5.330	0.005	0.081	0.0079
5.351	0.005	0.074	0.0064
5.899	0.005	0.008	0.0006
5.905	0.005	0.006	0.0004
5.909	0.005	0.006	0.0006
5.912	0.005	0.007	0.0004
5.915	0.005	0.006	0.0005
5.918	0.005	0.006	0.0004
5.921	0.005	0.007	0.0005
6.057	0.005	0.035	0.0024
6.061	0.005	0.027	0.0019
6.066	0.005	0.026	0.0020
6.068	0.005	0.032	0.0022
6.074	0.005	0.033	0.0023
6.078	0.005	0.031	0.0025
6.082	0.005	0.036	0.0025
6.089	0.005	0.040	0.0028
6.500	0.005	0.016	0.0011
6.508	0.005	0.011	0.0008
6.516	0.005	0.014	0.0020
6.525	0.005	0.013	0.0009
6.533	0.005	0.022	0.0015
6.542	0.005	0.013	0.0011
6.554	0.005	0.013	0.0018
6.567	0.005	0.014	0.0017

Table 7: Yield of ^{22}Na-gated neutrons per Coulomb, scaled relative to Na yields, from the fluorine-beam experiment (§3.b.6). E_{eff} is the effective laboratory energy of an alpha particle in the center of target corresponding to the same center of mass energy as the laboratory energy of the fluorine beam; δY is the uncertainty in the neutron yield per Coulomb. A separate scaling factor is used for each of the four fluorine beam energy ranges.

E_{eff} (MeV)	Scaling factor	Neutron Yield (cts/Coulomb)	δY (cts/Coulomb)
5.267	10.5	1.14	0.080
5.288	10.5	1.27	0.140
5.309	10.5	2.46	0.220
5.33	10.5	0.85	0.080
5.351	10.5	0.77	0.070
5.899	40.5	0.33	0.023
5.905	40.5	0.25	0.018
5.909	40.5	0.24	0.024
5.912	40.5	0.26	0.018
5.915	40.5	0.23	0.020
5.918	40.5	0.24	0.017
5.921	40.5	0.27	0.020
6.057	34.1	1.21	0.080
6.061	34.1	0.92	0.060
6.066	34.1	0.88	0.070
6.068	34.1	1.08	0.080
6.074	34.1	1.12	0.080
6.078	34.1	1.07	0.090
6.082	34.1	1.22	0.080
6.089	34.1	1.37	0.090
6.500	29.9	0.47	0.030
6.508	29.9	0.33	0.023
6.516	29.9	0.43	0.060
6.525	29.9	0.38	0.030
6.533	29.9	0.65	0.040
6.542	29.9	0.38	0.030
6.554	29.9	0.38	0.060
6.567	29.9	0.43	0.050

Table 8: Relative yield per Coulomb based on a weighted average of ^{22}Na yields and scaled ^{22}Na-gated neutron yields from the fluorine-beam experiment (§3.b.6). E_{eff} is the effective laboratory energy of an alpha particle in the center of target corresponding to the same center of mass energy as the laboratory energy of the fluorine beam; ΔE_{tgt} is the full energy loss of the beam in the target; δY− and δY+ are the asymmetric uncertainties in the average yield per Coulomb.

E_{eff} (MeV)	ΔE_{tgt} (MeV)	Average Yield (cts/Coulomb)	δY- (cts/Coulomb)	δY+ (cts/Coulomb)
5.267	0.005	1.07	0.096	0.083
5.288	0.005	1.18	0.110	0.133
5.309	0.005	2.79	0.310	0.270
5.330	0.005	0.91	0.086	0.071
5.351	0.005	1.09	0.123	0.115
5.899	0.005	0.32	0.021	0.021
5.905	0.005	0.25	0.018	0.018
5.909	0.005	0.27	0.020	0.021
5.912	0.005	0.29	0.020	0.019
5.915	0.005	0.28	0.020	0.020
5.918	0.005	0.28	0.020	0.020
5.921	0.005	0.30	0.020	0.020
6.057	0.005	1.14	0.080	0.079
6.061	0.005	1.04	0.070	0.071
6.066	0.005	1.02	0.070	0.070
6.068	0.005	1.08	0.070	0.070
6.074	0.005	1.23	0.090	0.083
6.078	0.005	1.10	0.080	0.073
6.082	0.005	1.27	0.090	0.091
6.089	0.005	1.45	0.096	0.096
6.500	0.005	0.43	0.029	0.029
6.508	0.005	0.31	0.021	0.021
6.516	0.005	0.48	0.036	0.036
6.525	0.005	0.34	0.024	0.024
6.533	0.005	0.60	0.045	0.045
6.542	0.005	0.39	0.029	0.028
6.554	0.005	0.45	0.037	0.046
6.567	0.005	0.43	0.031	0.035

Table 9: Cross sections based on scaling the relative yield per Coulomb from the fluorine-beam experiment to cross section results from the alpha-beam experiment (§3.c). E_{eff} is the effective laboratory energy of an alpha particle in the center of target corresponding to the same center of mass energy as the laboratory energy of the fluorine beam; ΔE_{tgt} is the full energy loss of the beam in the target; δσ– and δσ+ are the asymmetric uncertainties in the cross section.

E_{eff} (MeV)	ΔE_{tgt} (MeV)	Cross section (mb)	δσ– (mb)	δσ+ (mb)
5.267	0.005	224	20	17
5.288	0.005	248	23	28
5.309	0.005	586	66	56
5.330	0.005	190	18	15
5.351	0.005	230	26	24
5.899	0.005	260	17	17
5.905	0.005	206	14	14
5.909	0.005	220	17	17
5.912	0.005	234	16	16
5.915	0.005	231	17	16
5.918	0.005	230	16	16
5.921	0.005	245	16	16
6.057	0.005	267	18	19
6.061	0.005	244	17	17
6.066	0.005	240	16	16
6.068	0.005	253	16	16
6.074	0.005	288	20	20
6.078	0.005	259	18	17
6.082	0.005	299	22	21
6.089	0.005	341	22	22
6.500	0.005	270	18	18
6.508	0.005	194	13	13
6.516	0.005	303	23	23
6.525	0.005	214	15	15
6.533	0.005	380	28	28
6.542	0.005	247	18	18
6.554	0.005	285	23	29
6.567	0.005	270	20	22

Table 10: Combined cross section results from both the alpha-beam experiment and the fluorine-beam experiment (§3.c). For alpha-beam runs, E_{eff} is the laboratory energy of the alpha beam at the center of the target; for fluorine-beam runs, E_{eff} is the effective laboratory energy of an alpha particle in the center of target corresponding to the same center of mass energy as the laboratory energy of the fluorine beam; δE_{eff} is the uncertainty in E_{eff} ; ΔE_{tgt} is the full energy loss of the beam in the target; σ is the cross section; $\delta\sigma-$ and $\delta\sigma+$ are the asymmetric uncertainties in the cross section. The data is plotted in Fig. 3-43.

E_{eff} (MeV)	δE_{eff} (MeV)	ΔE_{tgt} (MeV)	σ (mb)	$\delta\sigma-$ (mb)	$\delta\sigma+$ (mb)
3.92	0.0170	0.0135	30.9	2.7	2.7
3.95	0.0170	0.0130	45.4	3.1	3.1
3.96	0.0170	0.0130	53.8	3.7	3.7
3.99	0.0170	0.0130	67.0	4.2	4.2
4.01	0.0170	0.0130	47.5	3.1	3.1
4.04	0.0170	0.0130	53.6	3.5	3.5
4.07	0.0170	0.0130	63.0	4.5	4.5
4.09	0.0170	0.0130	78.6	5.4	5.4
4.11	0.0170	0.0130	49.5	4.6	4.6
4.14	0.0170	0.0130	42.7	4.7	4.7
4.143	0.0050	0.0130	33.2	5.4	5.4
4.17	0.0170	0.0130	50.7	3.6	3.6
4.19	0.0170	0.0130	39.4	3.4	3.4
4.22	0.0170	0.0125	86.0	5.8	5.8
4.24	0.0170	0.0125	93.1	5.7	5.7
4.27	0.0170	0.0125	106	7.3	7.3
4.29	0.0170	0.0125	82.5	5.8	5.8
4.316	0.0050	0.0125	104	6.6	6.6
4.32	0.0170	0.0125	96.9	6.0	6.0
4.34	0.0170	0.0125	64.9	5.3	5.3
4.37	0.0170	0.0125	57.1	5.8	5.8
4.39	0.0170	0.0125	55.1	4.7	4.7
4.42	0.0170	0.0125	56.6	4.1	4.1
4.44	0.0170	0.0125	72.6	5.1	5.1
4.47	0.0170	0.0125	137	13	13
4.49	0.0170	0.0125	138	8.8	8.8
4.51	0.0170	0.0120	104	12	12
4.57	0.0170	0.0120	170	13	13
4.604	0.0050	0.0120	144	14	14
4.626	0.0050	0.0120	176	16	16
4.634	0.0050	0.0120	182	14	14
4.644	0.0050	0.0120	167	14	14
4.654	0.0050	0.0120	153	15	15
4.66	0.0170	0.0120	188	12	12
4.663	0.0050	0.0120	150	9.4	9.4
4.67	0.0170	0.0120	181	13	13
4.681	0.0050	0.0120	175	18	18
4.686	0.0050	0.0120	192	12	12
4.706	0.0050	0.0120	173	16	16

4.71	0.0170	0.0120	172	11	11
4.731	0.0050	0.0120	119	12	12
4.756	0.0050	0.0120	164	15	15
4.76	0.0170	0.0120	66	5.1	5.1
4.769	0.0050	0.0120	71.3	9.1	9.1
4.78	0.0170	0.0120	75	5	5
4.791	0.0050	0.0120	62.5	5.9	5.9
4.81	0.0170	0.0120	94.1	8.5	8.5
4.87	0.0170	0.0115	87.1	5.6	5.6
4.88	0.0170	0.0115	88.4	5.6	5.6
4.92	0.0170	0.0115	107	15	15
4.99	0.0170	0.0115	125	12	12
4.994	0.0050	0.0115	133	11	11
5.02	0.0170	0.0115	137	12	12
5.019	0.0050	0.0115	127	11	11
5.14	0.0170	0.0115	136	10	10
5.169	0.0050	0.0115	126	10	10
5.23	0.0170	0.0110	124	11	11
5.267	0.0030	0.0050	224	20	17
5.288	0.0030	0.0050	248	23	28
5.294	0.0050	0.0110	251	18	18
5.309	0.0030	0.0050	586	66	56
5.319	0.0050	0.0110	296	20	20
5.330	0.0030	0.0050	190	18	15
5.344	0.0050	0.0110	201	14	14
5.351	0.0030	0.0050	230	26	24
5.361	0.0050	0.0110	209	15	15
5.392	0.0050	0.0110	241	16	16
5.419	0.0050	0.0110	227	15	15
5.445	0.0050	0.0110	197	16	16
5.470	0.0050	0.0110	198	13	13
5.495	0.0050	0.0110	187	12	12
5.519	0.0050	0.0110	178	13	13
5.544	0.0050	0.0110	201	13	13
5.570	0.0050	0.0110	233	14	14
5.594	0.0050	0.0110	261	16	16
5.644	0.0050	0.0110	143	11	11
5.669	0.0050	0.0110	93.7	11	11
5.694	0.0050	0.0110	169	11	11
5.720	0.0050	0.0105	213	13	13
5.745	0.0050	0.0105	182	11	11
5.797	0.0050	0.0105	235	16	16
5.820	0.0050	0.0105	280	18	18
5.845	0.0050	0.0105	329	21	21
5.870	0.0050	0.0105	308	20	20
5.895	0.0050	0.0105	258	18	18
5.899	0.0030	0.0050	260	17	17

5.905	0.0030	0.0050	206	14	14
5.909	0.0030	0.0050	220	17	17
5.912	0.0030	0.0050	234	16	16
5.915	0.0030	0.0050	231	17	16
5.918	0.0030	0.0050	230	16	16
5.920	0.0050	0.0105	236	17	17
5.921	0.0030	0.0050	245	16	16
5.945	0.0050	0.0105	269	18	18
5.970	0.0050	0.0105	344	23	23
5.995	0.0050	0.0105	330	21	21
6.020	0.0050	0.0105	303	20	20
6.045	0.0050	0.0105	252	17	17
6.057	0.0030	0.0050	267	18	19
6.061	0.0030	0.0050	244	17	17
6.066	0.0030	0.0050	240	16	16
6.068	0.0030	0.0050	253	16	16
6.070	0.0050	0.0105	276	18	18
6.074	0.0030	0.0050	288	20	20
6.078	0.0030	0.0050	259	18	17
6.082	0.0030	0.0050	299	22	21
6.089	0.0030	0.0050	341	22	22
6.095	0.0050	0.0105	326	22	22
6.119	0.0050	0.0105	341	23	23
6.145	0.0050	0.0105	408	27	27
6.170	0.0050	0.0105	439	28	28
6.195	0.0050	0.0105	362	25	25
6.222	0.0050	0.0100	294	21	21
6.245	0.0050	0.0100	283	19	19
6.270	0.0050	0.0100	300	20	20
6.295	0.0050	0.0100	318	21	21
6.320	0.0050	0.0100	333	22	22
6.345	0.0050	0.0100	373	24	24
6.370	0.0050	0.0100	308	19	19
6.395	0.0050	0.0100	304	20	20
6.420	0.0050	0.0100	384	27	27
6.445	0.0050	0.0100	373	24	24
6.470	0.0050	0.0100	336	21	21
6.495	0.0050	0.0100	265	17	17
6.500	0.0030	0.0050	270	18	18
6.508	0.0030	0.0050	194	13	13
6.516	0.0030	0.0050	303	23	23
6.520	0.0050	0.0100	269	17	17
6.525	0.0030	0.0050	214	15	15
6.533	0.0030	0.0050	380	28	28
6.542	0.0030	0.0050	247	18	18
6.554	0.0030	0.0050	285	23	29
6.567	0.0030	0.0050	270	20	22

6.645	0.0050	0.0100	268	18	18
6.670	0.0050	0.0100	338	22	22

Table 11: Details on the cross section and uncertainty for each data point from the alpha-beam and fluorine-beam experiments (§3.c). For the alpha-beam runs, E_{eff} is the laboratory energy of the alpha beam at the center of the target; for the fluorine-beam runs, E_{eff} is the effective laboratory energy of an alpha particle in the center of target corresponding to the same center of mass energy as the laboratory energy of the fluorine beam; ΔE_{tgt} is the full energy loss of the beam in the target; σ is the cross section; $\delta\sigma-$ and $\delta\sigma+$ are the asymmetric uncertainties in the cross section; $\delta_{fit}-$ and $\delta_{fit}+$ are the asymmetric uncertainties arising from fitting the alpha-beam experiment *measured yield vs. angle* distribution with the *predicted yield vs. angle* distribution from the simulation (§3.a.7), or the uncertainties from the particle identification windows in the gas ionization counter used to determine the yield of ^{22}Na and neutrons in the fluorine-beam experiment; $\sigma_{\checkmark}$ is the cross section portion added in to the total for certain runs to account for populated ^{22}Na levels with neutrons below the detection threshold (§3.a.10); $\delta\sigma_a$ is the uncertainty in the added cross section; $\delta\sigma_{He}$ is the systematic uncertainty for the alpha-beam experiment including detection efficiency (4%), MCNP simulations (4%), and target thickness (2%) (§3.a.9); $\delta\sigma_b$ is the uncertainty in the beam current integration that occurred in certain runs when the beam current integrator module failed (§3.a.3); and $\delta\sigma_F$ is the systematic uncertainty in the fluorine-beam experiment including beam current and target thickness normalization (0.2%) and yield reproducibility (6%) (§3.b.6). The "origin code" describes where this data point was measured: 1 – alpha-beam experiment; 2 – fluorine-beam experiment, ^{22}Na and neutrons; 3 – fluorine-beam experiment, neutrons only. The "σ code" gives details of the cross section determination; for data points that do not contain these codes, the contribution from the corresponding effect to the cross section was negligible or none; **a** – forward peak (§3.a.10); **b** – added cross section (§3.a.10); **c** – merged data points (§3.a.8); **d** – fluorine-beam result from weighted average of both ^{22}Na and neutrons (§3.b.6); **e** – fluorine-beam result from neutrons only (§3.b.5); **f** – interpolation of alpha scattering (§3.b.3); **g** – dipole angular distribution of neutrons (§3.1.10). The "$\delta\sigma$ code" gives a list of terms contributing to the cross section uncertainty; for data points that do not contain these codes, the contribution from the corresponding effect to the cross section was negligible or none; **1** – forward peak (§3.a.10); **2** – added cross section (§3.a.10); **3** – low statistics (§3.a.2); **4** – estimated beam current integration (§3.a.3); **5** – recalculated beam energy (§3.a.9).

E_{eff} (MeV)	ΔE_{tgt} (MeV)	σ (mb)	$\delta\sigma-$ (mb)	$\delta\sigma+$ (mb)	$\delta_{fit}-$ (mb)	$\delta_{fit}+$ (mb)	σ_a (mb)	$\delta\sigma_a$ (mb)	$\delta\sigma_{He}$ (%)	$\delta\sigma_b$ (mb)	$\delta\sigma_F$ (%)	origin code	σ code	$\delta\sigma$ code
3.92	0.0135	30.9	2.7	2.7	2.0	2.0			6			1		3,5
3.95	0.0130	45.4	3.1	3.1	1.6	1.6			6			1		5
3.96	0.0130	53.8	3.7	3.7	1.8	1.8			6			1		5
3.99	0.0130	67.0	4.2	4.2	1.2	1.2			6			1		5
4.01	0.0130	47.5	3.1	3.1	1.1	1.1			6			1		5
4.04	0.0130	53.6	3.5	3.5	1.4	1.4			6			1		5
4.07	0.0130	63.0	4.5	4.5	2.5	2.5			6			1		5
4.09	0.0130	78.6	5.4	5.4	2.7	2.7			6			1		5
4.11	0.0130	49.5	4.6	4.6	3.5	3.5			6			1	c	5
4.14	0.0130	42.7	4.7	4.7	3.9	3.9			6			1	a	1,3,5
4.143	0.0130	33.2	5.4	5.4	5.0	5.0			6			1	a	1,3
4.17	0.0130	50.7	3.6	3.6	1.9	1.9			6			1	a	1,5
4.19	0.0130	39.4	3.4	3.4	2.5	2.5			6			1	g	3,5
4.22	0.0125	86.0	5.8	5.8	2.6	2.6			6			1		5
4.24	0.0125	93.1	5.7	5.7	1.2	1.2			6			1		5
4.27	0.0125	105.7	7.3	7.3	3.5	3.5			6			1	g	5

4.29	0.0125	82.5	5.8	5.8	3.1	3.1			6			1	c,g	5
4.316	0.0125	104.1	6.6	6.6	2.0	2.0			6			1		
4.32	0.0125	96.9	6.0	6.0	1.5	1.5			6			1	g	5
4.34	0.0125	64.9	5.3	5.3	3.7	3.7			6			1	c	5
4.37	0.0125	57.1	5.8	5.8	4.7	4.7			6			1	a,c	1,5
4.39	0.0125	55.1	4.7	4.7	3.3	3.3			6			1	a	1,5
4.42	0.0125	56.6	4.1	4.1	2.4	2.4			6			1	g	5
4.44	0.0125	72.6	5.1	5.1	2.7	2.7			6			1	g	5
4.47	0.0125	137.3	13.2	13.2	10.3	10.3			6			1		3,5
4.49	0.0125	137.7	8.8	8.8	3.0	3.0			6			1		5
4.51	0.0120	104.5	11.6	11.6	3.7	3.7	25	6	6			1		5
4.57	0.0120	170.1	12.9	12.9	1.9	1.9	51	6	6			1	b,g	2,5
4.604	0.0120	143.8	14.1	14.1	5.2	5.2	51	6	6			1	b,c	2,3
4.626	0.0120	176.5	15.9	15.9	4.4	4.4	51	6	6	5.7		1	b,g	2,4
4.634	0.0120	182.0	14.0	14.0	2.7	2.7	51	6	6			1	b,g	2
4.644	0.0120	167.0	14.4	14.4	4.3	4.3	51	6	6			1	b	2
4.654	0.0120	153.5	14.9	14.9	5.7	5.7	51	6	6			1	c	3
4.66	0.0120	187.9	12.4	12.4	5.1	5.1			6			1		5
4.663	0.0120	149.9	9.4	9.4	2.6	2.6			6			1		
4.67	0.0120	181.3	12.5	12.5	6.2	6.2			6			1		5
4.681	0.0120	174.9	17.8	17.8	7.1	7.1			6	12.5		1		4
4.686	0.0120	192.4	12.3	12.3	3.7	3.7			6			1		
4.706	0.0120	173.2	15.9	15.9	6.4	6.4			6	10.2		1		4
4.71	0.0120	171.8	11.1	11.1	3.8	3.8			6			1		5
4.731	0.0120	119.4	12.4	12.4	7.6	7.6			6	6.6		1	c	4
4.756	0.0120	164.1	15.2	15.2	3.7	3.7			6	10.9		1		4
4.76	0.0120	66.0	5.1	5.1	3.2	3.2			6			1		5
4.769	0.0120	71.3	9.1	9.1	3.8	3.8			6	7.1		1		4
4.78	0.0120	75.0	5.0	5.0	2.2	2.2			6			1		5
4.791	0.0120	62.5	5.9	5.9	3.4	3.4			6	3.1		1		4
4.81	0.0120	94.1	8.5	8.5	6.3	6.3			6			1		3,5
4.87	0.0115	87.1	5.6	5.6	2.1	2.1			6			1		5
4.88	0.0115	88.4	5.6	5.6	1.9	1.9			6			1		5
4.92	0.0115	106.5	15.1	15.1	13.7	13.7			6			1		3,5
4.99	0.0115	125.2	12.3	12.3	3.7	3.7	14	6	6			1	b,g	2,3,5
4.994	0.0115	132.6	11.5	11.5	2.2	2.2	14	6	6			1	b,g	2
5.02	0.0115	137.2	11.6	11.6	2.1	2.1	28	6	6			1	b,g	2,5
5.019	0.0115	127.3	11.2	11.2	2.2	2.2	28	6	6			1	b,g	2
5.14	0.0115	135.5	10.2	10.2	6.2	6.2			6			1	g	1,5
5.169	0.0115	126.1	10.5	10.5	2.9	2.9			6			1	g	
5.23	0.0110	124.1	11.2	11.2	8.4	8.4			6			1		3,5
5.267	0.0050	224.1	20.2	17.4	15.1	11.1					6.3	2	d	
5.288	0.0050	247.8	23.0	28.0	17.6	23.7					6.3	2	c,d	
5.294	0.0110	251.4	18.0	18.0	5.9	5.9	25	4	6			1	b,c	2
5.309	0.0050	585.9	66.0	55.8	55.9	43.3					6.3	2	c,d	
5.319	0.0110	296.1	20.0	20.0	5.1	5.1	25	4	6			1	b	2
5.330	0.0050	190.3	18.1	14.9	14.1	9.6					6.3	2	c,d	

5.344	0.0110	201.4	14.4	14.4	3.9	3.9	25	4	6			1	b	2
5.351	0.0050	229.9	25.9	24.2	21.9	19.9					6.3	2	c,d	
5.361	0.0110	208.5	15.1	15.1	4.4	4.4	25	4	6			1	b	2
5.392	0.0110	241.4	16.1	16.1	3.0	3.0	25	4	6			1	b	2
5.419	0.0110	226.6	15.3	15.3	2.9	2.9	25	4	6			1	b	2
5.445	0.0110	197.4	15.8	15.8	5.7	5.7	25	4	6			1	b	2
5.470	0.0110	198.4	12.6	12.6	4.1	4.1			6			1		
5.495	0.0110	187.3	11.6	11.6	2.8	2.8			6			1		
5.519	0.0110	178.0	13.3	13.3	7.9	7.9			6			1		
5.544	0.0110	201.2	12.9	12.9	4.6	4.6			6			1		
5.570	0.0110	232.7	14.2	14.2	2.6	2.6			6			1		
5.594	0.0110	261.0	15.9	15.9	2.8	2.8			6			1		
5.644	0.0110	143.2	11.5	11.5	7.6	7.6			6			1		
5.669	0.0110	93.7	10.7	10.7	9.1	9.1			6			1		3
5.694	0.0110	168.9	10.8	10.8	3.6	3.6			6			1		
5.720	0.0105	212.6	13.1	13.1	3.0	3.0			6			1		
5.745	0.0105	181.9	11.3	11.3	2.8	2.8			6			1		
5.797	0.0105	235.3	15.8	15.8	3.0	3.0	20	4	6			1	b,g	2
5.820	0.0105	279.5	18.4	18.4	3.5	3.5	41	4	6			1	b,g	2
5.845	0.0105	329.4	21.0	21.0	3.0	3.0	41	4	6			1	b	2
5.870	0.0105	308.4	19.7	19.7	2.8	2.8	41	4	6			1	b	2
5.895	0.0105	258.1	17.6	17.6	4.3	4.3	41	4	6			1	b	2
5.899	0.0050	260.3	16.8	16.8	6.3	6.3					6.3	2	d	
5.905	0.0050	205.7	14.3	14.3	7.3	7.3					6.3	3	e	
5.909	0.0050	219.5	17.1	17.4	11.0	11.3					6.3	2	d,f	
5.912	0.0050	234.2	15.8	15.6	7.2	6.7					6.3	2	d	
5.915	0.0050	230.7	16.5	16.3	9.0	8.6					6.3	2	d,f	
5.918	0.0050	230.0	16.4	16.2	8.8	8.5					6.3	2	d	
5.920	0.0105	236.2	16.5	16.5	4.5	4.5	41	4	6			1	b	2
5.921	0.0050	244.7	16.2	16.2	6.9	6.9					6.3	2	d,f	
5.945	0.0105	268.9	18.0	18.0	4.0	4.0	41	4	6			1	b,g	2
5.970	0.0105	343.7	22.5	22.5	9.0	9.0			6			1	g	
5.995	0.0105	329.7	21.1	21.1	7.3	7.3			6			1	g	
6.020	0.0105	303.0	19.6	19.6	7.2	7.2			6			1	g	
6.045	0.0105	252.0	16.7	16.7	7.0	7.0			6			1	g	
6.057	0.0050	267.0	18.3	18.6	8.8	9.4					6.3	2	d	
6.061	0.0050	243.6	17.3	16.7	9.2	8.2					6.3	2	d,f	
6.066	0.0050	239.6	16.5	16.5	8.0	8.0					6.3	2	d,f	
6.068	0.0050	253.3	16.4	16.4	6.3	6.3					6.3	2	d	
6.070	0.0105	276.1	18.5	18.5	8.2	8.2			6			1		
6.074	0.0050	288.1	20.2	19.6	10.4	9.2					6.3	2	d,f	
6.078	0.0050	258.6	17.8	17.2	8.8	7.5					6.3	2	d,f	
6.082	0.0050	299.1	21.9	21.5	12.6	11.8					6.3	2	d,f	
6.089	0.0050	341.0	22.5	22.5	9.3	9.3					6.3	2	d	
6.095	0.0105	325.9	21.9	21.9	9.9	9.9			6			1		
6.119	0.0105	341.4	22.7	22.7	9.8	9.8			6			1		
6.145	0.0105	408.4	26.9	26.9	11.1	11.1			6			1		

6.170	0.0105	439.5	27.7	27.7	8.6	8.6			6			1		
6.195	0.0105	362.3	25.2	25.2	8.6	8.6	16	4	6			1	b	2
6.222	0.0100	294.4	21.3	21.3	7.9	7.9	16	4	6			1	b	2
6.245	0.0100	283.3	19.2	19.2	5.0	5.0	16	4	6			1	b	2
6.270	0.0100	300.4	19.8	19.8	4.1	4.1	16	4	6			1	b	2
6.295	0.0100	318.2	20.6	20.6	3.8	3.8	16	4	6			1	b	2
6.320	0.0100	332.6	22.3	22.3	6.0	6.0	16	4	6			1	b	2
6.345	0.0100	372.5	24.4	24.4	9.8	9.8			6			1	c	
6.370	0.0100	307.6	18.7	18.7	3.0	3.0			6			1		
6.395	0.0100	303.6	20.0	20.0	6.7	6.7			6			1		
6.420	0.0100	384.4	26.8	26.8	13.7	13.7			6			1	c	
6.445	0.0100	372.7	24.2	24.2	9.3	9.3			6			1		
6.470	0.0100	336.2	21.4	21.4	7.2	7.2			6			1		
6.495	0.0100	264.9	16.7	16.7	5.1	5.1			6			1		
6.500	0.0050	269.6	18.3	18.3	8.5	8.5					6.3	2	d	
6.508	0.0050	194.2	13.0	13.0	5.7	5.7					6.3	2	d	
6.516	0.0050	303.2	22.6	22.6	13.5	13.5					6.3	2	d	
6.520	0.0100	269.1	16.9	16.9	4.9	4.9			6			1		
6.525	0.0050	213.7	14.9	14.9	7.7	7.7					6.3	2	d	
6.533	0.0050	380.0	28.3	28.4	16.8	16.9					6.3	2	d	
6.542	0.0050	246.6	18.1	17.9	10.4	10.1					6.3	2	d	
6.554	0.0050	284.9	23.5	28.7	16.1	23.1					6.3	2	d	
6.567	0.0050	270.1	19.8	21.7	11.3	14.5					6.3	2	d	
6.645	0.0100	267.5	18.0	18.0	8.2	8.2			6			1		
6.670	0.0100	338.2	22.2	22.2	8.9	8.9			6			1		

Table 12: Neutron yields from simulations of a solid UF_6 sphere with a variety of $^{19}F(\alpha,n)^{22}Na$ cross sections and two different enrichments (§5.b). The results are plotted in Fig. 5-2.

^{235}U (% U mass)	$^{19}F(\alpha,n)^{22}Na$ Cross Section	Neutron Yield (neutrons/alpha)	Neutron Yield (neutrons/g*s)
3.0	MCNP6 Models	0	0
3.0	TENDL -25%	1.62245E-06	1.14E-01
3.0	TENDL	2.14185E-06	1.51E-01
3.0	TENDL +25%	2.67301E-06	1.89E-01
3.0	Present Measurement -7%	1.79026E-06	1.26E-01
3.0	Present Measurement	1.92712E-06	1.36E-01
3.0	Present Measurement +7%	2.04099E-06	1.44E-01
57.38	MCNP6 Models	0	0
57.38	TEND -25%	1.64606E-06	1.10E+00
57.38	TENDL	2.24219E-06	1.50E+00
57.38	TENDL +25%	2.80755E-06	1.87E+00
57.38	Present Measurement -7%	1.85089E-06	1.23E+00
57.38	Present Measurement	1.97763E-06	1.32E+00
57.38	Present Measurement +7%	2.10956E-06	1.41E+00